UNIVERSITY
OF TRENTO

ISTITUTO NAZIONALE
DI GEOFISICA E VULCANOLOGIA

Doctorate of National Interest
on
Space Science and Technology

The Co-Volcanic Ionospheric Disturbances at Mt. Etna, Italy

Federico Ferrara

Supervisor
Dr. Alessandro Bonforte

Co-supervisors
Dr. Michela Ravanelli
Dr. Jaroslav Chum

October 2025

Contents

1 Introduction **1**

1.1 The ionospheric volcanology 2

1.2 The Co-Volcanic Ionospheric Disturbances 3

1.3 The ionospheric forcing from Mt. Etna 5

2 The Lithosphere - Atmosphere - Ionosphere environment **7**

2.1 The volcanic eruptions 7

2.1.1 Seismo-acoustic activity of Mt. Etna 9

2.1.2 The large-scale lava fountains at Mt. Etna 11

2.1.3 Volcanic plume dynamics 12

2.2 The atmosphere 15

2.2.1 The thermal layering of the atmosphere 18

2.2.1.1 Potential temperature and the parcel concept 20

2.2.2 Plasma of the atmosphere: the ionosphere 22

2.3 The atmospheric waves 25

2.3.1 The Lamb waves 26

2.3.2 The acoustic-gravity waves 27

2.3.2.1 Basic equations of acoustic-gravity waves . . 32

2.4 The traveling ionospheric disturbances 35

3 Data and methods **37**

3.1 The GNSS - TEC method 37

3.1.1 Variometric Approach for Real-time Ionosphere Observation 41

3.1.2 The GNSS - TEC satellite geometry 42

3.1.3 GNSS dataset arrangement 46

3.2 Geomagnetic indices and the electron density profile 48

3.3 Seismo-acoustic monitoring of Mt. Etna 50

3.4 Spectral analysis techniques 50

4 The December 4th 2015 eruption **53**
4.1 The seismo-acoustic activity 54
4.2 The ionospheric TEC analysis 56
4.2.1 Doppler shift correction and the intrinsic wave characteristics 64
4.2.2 Source characterization and infrasound ray tracing . 67
4.2.3 Data integration 68

5 The April 12th 2012 eruption **71**
5.1 The seismo-acoustic activity 72
5.2 The ionospheric TEC analysis 73

6 The July 4th 2024 eruption **80**
6.1 The seismo-acoustic activity 80
6.2 The ionospheric TEC analysis 82

7 Discussion **88**

8 Conclusion **93**

Abstract

Global Navigation Satellite Systems (GNSS), originally developed for positioning and navigation, are now widely used for ionospheric sounding. Due to the dispersive nature for radio waves, the ionosphere affects the GNSS signals as a function of its electron density. By this condition the total electron content (TEC) of the ionosphere can be estimated from GNSS data. TEC fluctuations can be related, from above, to space weather dynamics or, from below, to geodynamic events and then GNSS-TEC applications represent an innovative technique to improve the studies on natural hazards.
Volcanic eruptions perturb the atmosphere by changing temperature, pressure and density of the surrounding air. In particular, the thermodynamic forcing from explosive eruptions can generate acoustic-gravity waves that, due to the exponential decrease in air density and to the conservation of kinetic energy, propagate upward until to reach the electron density layers of the ionosphere. The match between the acoustic-gravity waves and the ionospheric layers induces electron density oscillations affecting the satellite-receiver line of sight of GNSS. This type of oscillations can be visualized in terms of TEC fluctuations that are called co-volcanic ionospheric disturbances (CVIDs) and they represent a key observational signature of the coupling processes between lithosphere, atmosphere and ionosphere.
Based on the GNSS-TEC application, the coupling processes between lithosphere and ionosphere have been studied into regional scale at Mt. Etna (Italy). Leveraging a dense and proximal GNSS network around the volcano, co-volcanic ionospheric disturbances are observed during three large-scale lava fountains that occurred on April 12th 2012, December 4th 2015 and July 4th 2024. The associated TEC perturbations occur in the near field, within 300 km of Mt. Etna, with an estimated apparent velocity around 200 m·s^{-1} and dominant frequency around 1 mHz. The spectral signature is consistent with the propagation of internal gravity waves, by suggesting that the paroxysmal activity of Mt. Etna is coupled with the ionospheric electron density layers through the lower-middle atmosphere. The results provide an unprecedented spatiotemporal characterization of CVIDs at Mt. Etna based on GNSS observations. Differences in signal travel times among the investigated events suggest that lower-middle atmospheric dynamics,

including background wind conditions, may significantly modulate the ionospheric response to the explosive activity of Mt. Etna. The observed CVIDs seem to be typical for Mt. Etna, in such a way that these findings provide a potential GNSS-TEC framework to implement the monitoring of Mt. Etna and the characterization of the lithosphere-atmosphere-ionosphere coupling processes at the regional scale.

Chapter 1

Introduction

From volcanology to the upper atmosphere physics, by the support of the remote sensing, the study of the effects into the atmosphere induced by volcanic eruptions represents an important test field for the current technologies. The exponential progress of the informatics and of the electronics of the last 50 years provides nowadays the chance to carry out scientific research by cloud-based databases from (and for) different areas of the Earth. The main aim is to implement the knowledge on the natural hazards by the integration of innovative approaches inspired by the *multidisciplinary research*.

The solid Earth (e.g. lithosphere, internal structure) and the fluid Earth (e.g. hydrosphere, atmosphere) are two open systems exchanging energy continuously at their interfaces. Worldwide seismic signal observations highlight the continuous excitation of normal modes, noted as "hum", and their sources are located at the ocean mainly and in the atmosphere partially. The atmospheric component is able to excite the spheroidal modes of the solid Earth ${}_0S_{29}$ and ${}_0S_{34}$, corresponding to periods of 237 ($\sim$ 4.4 mHz) and 270 ($\sim$ 3.7 mHz) seconds, respectively [73, 103]. These types of seismic signals are observed not only from earthquakes but from volcanic eruptions also, as the effect of the acoustic resonance between the wave frequencies released in atmosphere, by the volcano, and the normal modes of the atmosphere itself [28, 90]. The phenomenon is the generation of atmospheric oscillations being reflected from the ground to the sky and vice versa. Due to this ground-air interaction, noted as "coupling", the earthquakes, volcanic eruptions, tsunamis, typhoons and any other type of energetic dynamic can release energy sufficient to perturb the lower and the upper atmosphere by different coupling processes. The coupling is named with respect to the point of

the source. If the source is below the atmosphere, we are talking about the Lithosphere-Atmosphere-Ionosphere Coupling (LAIC); if the source is above we are talking about the Magnetosphere-Ionosphere-Lithosphere Coupling (MILC). The current efforts in the LAIC/MILC studies focus on the near real-time ionospheric detection of natural hazards, ionospheric precursors, source localization, source identification and coupling modeling [4, 18, 59, 79, 96]. In this context, the volcanic eruptions are among those sources that can generate atmospheric perturbations by thermodynamic and electromagnetic coupling processes [44, 78].

1.1 The ionospheric volcanology

The ionosphere is the ionized portion of upper atmosphere that is fundamental for telecommunication since it is a dispersive medium for radio waves. This means that different information of the ionosphere can be retrieved as a function of the radio frequency. The Low Earth Orbit (LEO) satellites perform in-situ measures of the ionosphere, while ground-based instruments as HF-Doppler sounder, ionosondes, Over-The-Horizon (OTH) radars make the most since the radio frequency dependence from the electron density variations in the ionosphere. Starting from '90s, the Medium Earth Orbit (MEO) satellites are used to study the ionosphere. Based on the dual-frequency structure of the broadcast signal, phase-code differential variations due to the ionospheric refraction of the radio-transmitted waves are observed [60]. Nowadays, the Global Navigation Satellite Systems (GNSS) are based on MEO satellites offering a coverage for the point positioning of any area of the Earth's surface, by providing time and geographical coordinates continuously 24/7. The geometry-free linear combination of the GNSS observables provide estimations of the total electron content (TEC) of the ionosphere, and TEC oscillations are observed after energetic natural events occurring at the ground-air and sea-air interfaces. The ionospheric monitoring represents an innovative technique to detect volcanic eruptions by remote, and different studies are carried out to find time-space correlations between the TEC fluctuations and the magnitude of the eruptions [62]. In this way, the ionospheric detection of volcanic eruptions implies the study of the coupling processes between the lower (neutral) and the upper atmosphere (ionized) by opening new perspectives for satellite applications.

1.2 The Co-Volcanic Ionospheric Disturbances

Contrarily to an earthquake or a tsunami releasing energy only into the air, the volcanic eruption generates a hot plume intrusion in the atmosphere releasing mass of tephra and kinetic energy due to the magma fragmentation. Mass-energy transfer processes occur during the convective rise of the eruption column by changing temperature, pressure and density of the crossed local atmosphere. The thermodynamic pulse can perturb the surrounding air in such a way to generate acoustic-gravity waves (AGWs). The acoustic component propagates at smaller wavelengths and its restoring force is related to the atmospheric pressure; when the air-mass displacement is big enough to increase the wavelength of the perturbation, air density changes and its buoyancy oscillations trigger a gravity wave restored by the gravity force. The gravity waves (also called "internal gravity waves" to distinguish them from the gravity waves related to the tidal component of the Earth rotation) propagate at frequencies below the Brunt-Väisälä frequency ($\sim$ 2.9 mHz in lower atmosphere), while the acoustic phases propagate above the cut-off frequency $\sim$ 3.3 mHz [4, 54, 73].

It is well known that explosive eruptions can generate AGWs able to reach the ionosphere and induce TEC fluctuations by the collisions between neutrals and ions. The TEC signatures induced by volcanic activity are called Co-Volcanic Ionospheric Disturbances (CVIDs). The main information provided by the ionospheric volcanology is the ionospheric detection of explosive volcanic activity as a wave-like structure of the CVIDs coupled with the AGWs propagation below. However, due to the inconstancy of the neutralion system of the atmosphere, the time-space correlation between CVID characteristics and eruptions is matter of research. In general, the more is the power of the eruption the more is the amplitude of the TEC peak with a coherent increase of the ionospheric perturbation velocity. Small volcanic eruptions, related to shallow volcanic sources, like strombolian-vulcanian eruptions, are able to generate high frequency waves that are typically associated to infrasound. Large eruptions, related to deep volcanic sources, like subplinian-plinian eruptions, are able to generate shock waves and acoustic-gravity waves. Furthermore, the bigger is the volcanic source the wider is the spectrum of the CVIDs in such a way that the most powerful eruptions tend to generate atmospheric perturbations in all the acoustic-gravity frequency range [3, 21, 44, 51, 65, 69, 89, 90, 105]. CVIDs related to AGWs propagation are thus associated to the thermodynamic coupling between

the geospheres, that is induced by the pulse of an explosive eruption. The most of CVIDs reported in literature comes from medium-high energetic eruptions that are classified by a Volcanic Explosivity Index (VEI) equal or higher than 4 [70]. Resonance frequencies, related to the spheroidal modes ${}_0S_{29}$ and ${}_0S_{34}$ of the Earth, are clearly observed starting from VEI 4 eruptions. These TEC-based CVID signals are characterized by wavetrains, starting around 10 - 20 minutes after the eruption onset, and variable apparent velocities spanning from few hundreds of $m{\cdot}s^{-1}$ to around 1 $km{\cdot}s^{-1}$ as a function of the wave frequency: the acoustic waves are faster than the internal gravity waves and they come first. Therefore, we expect CVIDs from VEI $\geq$ 4 eruptions, but CVIDs from VEI 2 - 3 eruptions can be detected too [28, 43]. These less energetic eruptions are associated with TEC-based CVIDs signatures showing transition features between gravity and acoustic periods. While the frequency spectrum of CVIDs is more or less coherent with the magnitude of the eruption, the velocity variability from similar VEI eruptions is probably related to the different factors playing a role into LAIC processes. The satellite geometry, the number of receivers around the volcano, the geomagnetic field vectors, the ionospheric variability, the atmospheric temperature, the winds, the volcanic conduit geometry are all potential elements that can influence the satellite-based CVID detection from TEC estimations. Nowadays, CVIDs are observed from VEI 2 to VEI 6 eruptions with a frequency spectrum broadening with the eruptive power. The frequency content seems to start from acoustic only for VEI 2-3 eruptions, to transit at gravity and low acoustic frequencies for VEI 3-4 eruptions and finish with a wide acoustic-gravity range and shock waves for the powerful events. The transition from VEI 2 to VEI 6 is related to the volcanic source size and thus it is reasonable to hypothesize that VEI 2 eruptions come from shallow/small sources that can generate short period waves without significant thermodynamic effects into the atmosphere and typical impulsive one-cycle (i.e. N-shape) TEC signatures. Starting from VEI 3 eruptions, the volcanic source becomes deep and large enough to perturb the atmosphere thermodynamically by inducing air density variations and internal gravity waves adding to infrasound [13, 91].

However, less energetic eruptions are able also to perturb the ionosphere without a big pulse, but through substantial emissions of volcanic ash into the air. It is known that radioactive gases near the ground, like Radon escaping from the ground fractures, can change the electrical conductivity of the atmosphere by inducing variations of the ionospheric potential and

modify the electric circuit between the ground and the sky. Similar effects are observed during sand storms in the Sahara desert or during the Eyjafjallajökull eruption on April 16th 2010 (Iceland). In this case, the CVIDs have not a wave-like structure and they are characterized by wide areas of anomalous values of TEC. This kind of ionospheric perturbations are related to the electromagnetic coupling between geospheres [78].

1.3 The ionospheric forcing from Mt. Etna

Ionospheric responses to Mt. Etna (Italy) volcanic activity has been observed as TEC turbulence frequency variations before the December 24th 2018 eruption and by a statistical study based on the Volcanic Radiative Power (VRP) between 2000 and 2019 [24, 93]. These results open to focus on the coupling between Mt. Etna (hereafter the term "Etna" will be used also) and the local ionosphere above it. The VEI 2 - 3 eruptions that occurred in the early December 2015 show a linear relation between the Ionospheric Volcanic Power Index (IVPI) and the plume height, but spatio-temporal characterization of CVIDs at the Mt. Etna lack in literature [62]. This research is focused to fill this gap and the intrinsic characteristics of CVIDs at Mt. Etna are here reported with unprecedented detail, as co-volcanic TEC signatures recovered from GNSS data. Since the low-medium eruptive energy, only the usage of dense GNSS network around the volcano allows CVIDs detection from TEC estimations [37]. These local CVIDs appear as TEC fluctuations within 200 - 300 km of the vent occurring after the seismo-acoustic onset of the eruption and different timing, leading to hypothesize different subjects acting into LAIC process at Mt. Etna. My thesis reports ionospheric TEC fluctuations detected during some large-scale lava fountains that occurred at Mt. Etna. The research focuses on the morning eruption of December 4th 2015, as primary case study for the data analysis implementation. The study is characterized by a multidisciplinary approach comparing seismo-acoustic and video data with the TEC time series detected during the eruptive activity. Atmospheric and geomagnetic data of the eruption day integrate the information of the results. Fast Fourier Transform, Empirical Mode Decomposition and Continuous Wavelet Transform are applied to obtain the spectral features of these local co-volcanic ionospheric disturbances, and their intrinsic wave characteristics have obtained by taking into account the relative satellite motion. Observa-

tions of co-volcanic TEC signatures during Etna's eruptions that occurred in April 12^{th} 2012 and July 4^{th} 2024 are also reported by following the same methodology. These findings represent new case studies from Mt. Etna and a new baseline of information based on the GNSS-TEC applications. Specifically for Mt. Etna, the spot-like near field CVIDs appearance may depict new novels to future integrations into the monitoring network.

Chapter 2

The Lithosphere - Atmosphere - Ionosphere environment

The coupling processes between geospheres imply to study the different environments involved. The composition of the atmosphere, the winds and the geomagnetic field determine various gradients with altitude. From above, space weather dynamics can heavily affect the plasma of upper atmosphere by causing ionospheric disturbances that can shatter the link from satellites. On the other hand, volcanic eruptions influence the surrounding atmosphere by changing its chemical-physical properties as a function of magnitude or lasting of their occurrence. Therefore, co-volcanic acoustic-gravity waves (AGWs) can be generated by different eruptive dynamics and the lower atmosphere can attenuate the wave amplitude, or amplify it. By propagating in a well variable atmospheric mean, AGWs can reach the electron density layers of upper atmosphere to induce ionospheric disturbances representing the mark of the eruption.

2.1 The volcanic eruptions

The volcanoes are lithospheric apertures by which the magmatic fluids, generated into the Earth, come out as volcanic eruptions. The volcanic eruptions are basically recognized in *effusive* and *explosive*. The main difference between effusive and explosive is due to the ratio between the gas and the liquid-crystal volumes into the magma. This means that the more gas in the magma the more explosive the eruption will be, and from this variation different volcanological features arise. The effusive eruptions are characterized by lava flows, eruptive fissures and lava fields expanding for

long distances on the ground but relatively low plumes into the atmosphere; the explosive eruptions are characterized by emission of pyroclasts, medium-high plumes, high-convective eruption columns, pyroclastic density currents and ash fallouts. Examples of effusive eruptions are those of Fagradalsfjall 2023 (Iceland), Cumbre Vieja 2021 (Canary, Spain); on the other hand the Hunga-Tonga Hunga-Haapai 2022 eruption and Etna paroxysms are examples of different explosive eruptions [15, 55, 65, 94].

The fragmentation index F of the magma and the ash dispersal area D on the ground are two important parameters to distinguish different styles of volcanic explosive activities [99]. The F parameter is given by the percentage finer than a given arbitrary grain-size (e.g. 1 mm) in the entire assemblage of fragments thrown out by the eruption and then describes the explosivity grade of the depressurizing magma approaching to the surface. As F increases, the occurrence frequency of the explosions increases too and transition from effusive Hawaiian styles to Strombolian ones occurs. Strombolian eruptions are characterized by an intermittance of low-mid intensity explosions that can develop towards more energetic and relative continuous gas flows, typical of the Subplinian - Plinian styles. On the other hand, the D parameter is the area enclosed by an isopach bearing a fixed ratio to the maximum thickness of the deposit and represents the potential altitude reached by the volcanic plume before the ash fallout: the more broad D the higher is the plume. Plinian eruptions are characterized by high-convective eruption columns corresponding to higher values of D. The June 15 th 1991 Mt. Pinatubo (Philippines) eruption is the representation of a Plinian style (Fig. 2.1a). No-volcanic factors can abruptically change both F and D, as the water and the wind, by causing significant variations of the eruptive style. Indeed, hydrothermal fluids can interacts with the rising magma at shallow depths and lead to a dramatic exponential increase of F, that is typical of Surtseyan eruptions and phreato-magmatic variants. When no magma is involved, hot hydrothermal fluids can however reach pressurization threshold values, eventually induced by the fall of inner conduit blocks, in such a way to bring episodic strong explosions as Vulcanian eruptions and phreatic variants. On the other hand, the winds influence the volcanic plume dynamics, in such a way to steer the ash fallout along defined directions by causing co-elongated D. Another important parameter is the mass eruption rate Q that is related to the top plume height H_t by the power law

$$H_t = 0.318 \cdot Q^{0.253} \tag{2.1}$$

where Q is calculated in $kg \cdot s^{-1}$ and H_t is in km [10, 63, 106].
The more is the explosivity the more is the scale of the eruption. The merging of past classifications with other parameters lead to set the Volcanic Explosivity Index (VEI) [70]. The VEI is the most common classification of the volcanic eruptions since it gives an immediate idea of the magnitude and the effects into the atmosphere (Fig. 2.1b).

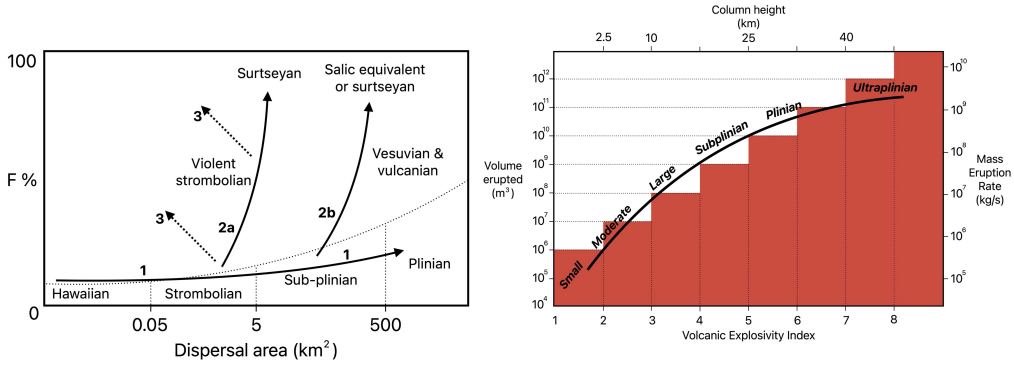

Figure 2.1: Classification of volcanic eruptions; a) classification based on fragmentation index F and ash dispersal area D with the relative main intermediate variations depicted as numerated black arrows; b) the Volcanic Explosivity Index based on different volcanological parameters. The solid black line indicates the relation between the eruption column height H and the mass eruption rate Q (a) from Walker 1973, modified).

The classifications here reported are not totally exhaustive since the chemical-physical features of the volcanic products ejected are not considered. Indeed petrology, geochemistry, field surveys of the volcanic deposits and the co-related studies have many other key parameters to recognize different eruptive styles and the related dynamics. The classification terms here used are the most general in the literature and appropriate to give a first-order idea of the differences among the volcanic eruptions.

2.1.1 Seismo-acoustic activity of Mt. Etna

When an eruptive activity happens, amplitude time series of seismic and infrasonic signals, recorded around the volcano, often show similar trends by implying a strict interaction between the inner eruptive mechanism (seismic data) and its effect into the atmosphere (infrasonic data). As such, infrasound and seismic sensors are routinely deployed colocated at active volcanoes [35, 50].

The Mt. Etna (37.75 °N - 14.99 °E) is located in Italy, at the eastern coast of Sicily island, less than 30 km north of Catania metropolitan city, and it is the most active and widest volcano in Europe (around 1500 km^2 wide and 3400 m high). The Istituto Nazionale di Geofisica e Vulcanologia - Osservatorio Etneo (INGV-OE), Italy, performs research, monitoring and surveillance 24/7 of Mt. Etna by the multi-parametric network for ground-based and satellite-based data. Eruptive activity at Etna generates a large variety of seismic signals such as volcano-tectonic earthquakes (VT), volcanic tremor, Long Period (LP) and Very Long Period (VLP) events [45, 102]. Ruling out the VT earthquakes, volcanic tremor and LP-VLP events are usually detected by broadband seismometers (able to detect periods longer than 1 s) within 10 km to the Etna summit craters. The volcanic tremor is a continuous ground vibration typically detected at open-conduit volcanoes. Its signal is not impulsive and quite stationary at periods around 0.2 - 2 s. The volcanic tremor could be related to fluid dynamics inside the plumbing system since it directly changes by variations in amplitude, spectral content, wavefield features and source location as the eruptive activity intensifies (INGV-OE - Real time volcanic tremor) [16]. At Mt. Etna, LP and VLP events can be detected before, during and after the eruption but also during any observable volcanic activity. The signals of LP events are characterized by very emergent onset without S-waves arrivals and periods into the tremor range. VLP events are characterized by periods around 2 - 100 s. Some of class with clear signal characteristics, representing the transition towards seismo-acoustic processes, are the *explosion quakes* accompanying Strombolian or other (larger) explosive eruptions. Most of the explosion quakes signals can be identified by the occurrence of an air-wave, which is caused by the sonic boost of the explosion, when the expanding gas is accelerated at the vent exit. Broadband seismometers detecting periods as long as 120 s may shed new information on the seismo-acoustic correlations in volcanic areas.

The infrasonic signals detected at Etna volcano are mainly transients, named *infrasonic events*, that are characterized by a variable duration from less than 1 s to more than 30 s, impulsive compressional onset and periods around 0.2 - 3 s. The infrasonic events characterize Strombolian eruptions and some degassing processes. Another type of infrasonic signal is the *infrasonic tremor*, that can be detected during energetic degassing or paroxysmal activities as a tremor-like continuous signal lasting from minutes to days. The infrasound monitoring provides the advantage to increase the preci-

sion of source localization but it can be affected by weathering, as wind or lightning [16, 88].

2.1.2 The large-scale lava fountains at Mt. Etna

Despite Etna long-standing reputation as an effusive volcano, since 1986 there has been an evident increase in mid-intensity explosive eruptions from its summit craters, known as paroxysms. The Etna paroxysms range from series of single explosions (e.g. Strombolian activity) to lava fountaining activity lasting from tens of minutes to a few days, producing some km-high volcanic plumes and ash fallouts up to hundreds of km^2 on the ground [2, 36]. More than 290 paroxysms have occurred since 1986 and the more energetic episodes occurring at the summit craters are known as *large-scale lava fountains* (LSLF). The transition from lava fountain to LSLF is mainly related to the ash dispersal area that goes from tens to hundreds of km^2. The large-scale lava fountains are characterized by tall lava fountains (up to a few thousand meters from the crater) and high eruption columns that can reach the lower stratosphere [2]. Usually, the fountaining activities occur into a sequence but the number of paroxysms for year can be various. For example, the lava fountains that occurred in 2000, from January to August, are 66 while those that occurred in 2021, from February to December, are 61. Between these 2 main series, the number of paroxysms is much less, for example the lava fountains that occurred in 2013 and 2015 are 18 and 4 respectively. In the last years the paroxysms that occurred in 2022, 2023 and 2024 are 2, 4 and 8 respectively [2, 12, 14]. The volcanic craters are the terminals of the main conduits for the magma rising towards the surface. The current Etna craters are five: Cratere di Nord-Est (CNE), Voragine (VOR), Bocca Nuova 1 (BN1), Bocca Nuova 2 (BN2) and Cratere di Sud-Est (CSE). Nevertheless, Etna's continuous activity can cause very quick changes of the morphology and altitude of the summit craters. Indeed, between November 2004 and November 2009, a series of collapse pits formed in various locations on the eastern flank of the CSE. Afterwards, during the eruptive cycle of January 2011 - April 2012, the site was definitely occupied by a large pyroclastic cone informally named Nuovo Cratere di Sud-Est (NSEC) [7]. NSEC was characterized to be the site of explosive activities, as the 2021 lava fountain series. During the 2021 eruptive cycle, NSEC progressively joined CSE to form one main crater again named CSE (INGV-OE - Multidisciplinary bulletins).

Etna LSLFs imply several risks to the population and the urban facilities mainly due to the extensive ash dispersal area. Indeed, the ash dispersion in the troposphere can cause the temporary closure of the Catania international airport, danger for driving due to the ash fallout on the roads, agriculture issues, heaviness of the roofs, obstacle to water drainage and health difficulties related to the breathing of the finest ashes.

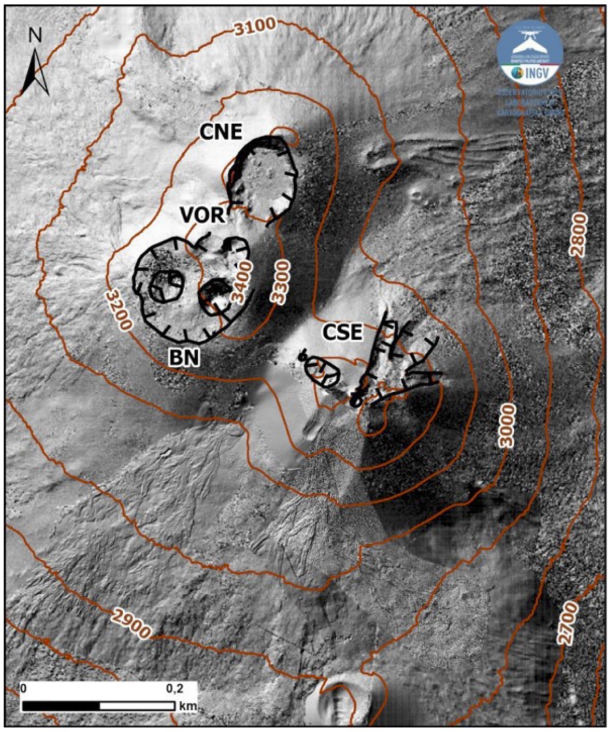

Figure 2.2: Shadowed relief of the summit area of Etna volcano. The geoidal contour lines are drawn every 100 meters. CSE = cratere di Sud-Est; BN = Bocca Nuova; VOR = Voragine; CNE = cratere di Nord-Est (INGV - multidisciplinary bulletin of December 2nd 2025).

2.1.3 Volcanic plume dynamics

Volcanic plumes are mixtures of volcanic particles, gases and air that are produced mainly by explosive eruptions. They are generated when magma (mixture of super-critical fluids and minerals) is fragmented into small pieces and discharged from the vent at high velocity in the air. Rapid acceleration of this material into the atmosphere is largely driven by the expansion of gases due to the decrease in pressure, as material is erupted at the surface. Volcanic plumes are injected into the atmosphere and they can disperse ash and gases on a global scale. Buoyancy plays a fundamental role in the

motion of plumes and determines how they interact with the atmosphere. Energetic plumes can rise to altitudes as great as 50 km above the Earth's surface and others are maintained for relatively long periods of time by the continuous discharge of material from the vent [19]. In no wind conditions, the volcanic plumes are characterized by a lower *gas-thrust region*, an intermediate *convective region* and the upper (typical) *umbrella region* (Fig. 2.3).

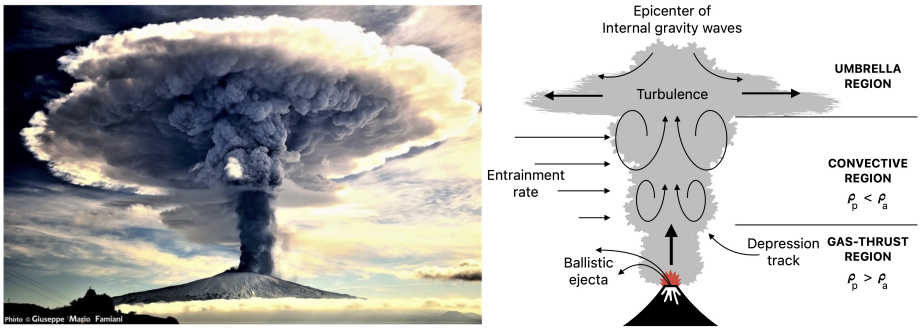

Figure 2.3: Eruption column occurred at Mt. Etna in December 4th 2015 taken from Cesarò town, northwest of the volcano. The gas-thrust, convective and umbrella regions are recognizable (credit: Giuseppe Mario Famiani).

The gas-thrust region is characterized by a distinct turbulent stream with density greater than the surrounding air. Here the temperature and the vertical velocity are the higher of the entire ascent process. This region is where the lava fountains take place and grain-size separation of tephra occurs through ballistic trajectories followed by particles greater than tens of centimeters [85]. The exit velocity w_{ex} of the lava fountain can be estimated as *ejecta exit velocity*

$$w_{\text{ex}} = \sqrt{2gh_f} \tag{2.2}$$

where g is the gravity acceleration at the vent altitude, h_f is the lava fountain height. This equation is based on the conservation law of energy and it is a good approximation for both a steady lava fountain and a single Strombolian explosion. It neglects the entrainment of air into the fountain. However, the gas velocity is twice the average ejecta velocity, suggesting that eq.(2.2) is very accurate to estimate an average velocity but it can underestimate the gas velocity at most by a factor of 2 [97].

Above the gas-thrust region, the unburdened plume mixes by turbulence with the surrounding air through the so-called *entrainment process*. The entraining air is colder and slighter than the plume, in such a way that the entrainment process activates the thermodynamic convection of the erup-

tion column and the stream accelerates again. Hence the plume becomes a convective system characterized by leading eddies separating from the gas-thrust region rapidly. The convective region develops upward, until the plume reaches a density equal than the atmosphere at the so-called buoyancy altitude H_b. Once the convective plume reaches the level of neutral buoyancy, it overshoots to the top height H_t due to its momentum at H_b

$$H_t = \frac{H_b}{0.7} \tag{2.3}$$

At height H_b the plume starts to spread horizontally by internal gravity waves and the spreading current forms the umbrella region between H_b and H_t with a thickness $z_u = 0.3H_t$ (Fig. 2.3). The point where the plume changes its direction, from subvertical to subhorizontal, is called plume corner $x_0 = 0.24H_t$ [11, 85].

Studies of thermal plumes show that the time-averaged vertical velocity w is a symmetrical gaussian function of distance from the plume axis

$$w = w_c \cdot e^{\frac{-x^2}{b^2}} \tag{2.4}$$

where w_c is the centerline velocity at height h, x is the radial distance from w_c, b is the distance at which w decreases to 1/e times w_c. The vectorial sum of $w(h)$ defines the plume axis.

Volcanic plume dynamics are strongly dependent on the wind field and then they are classified in *strong* and *weak plumes*, when w is much greater or much smaller than the cross-wind speed, respectively.

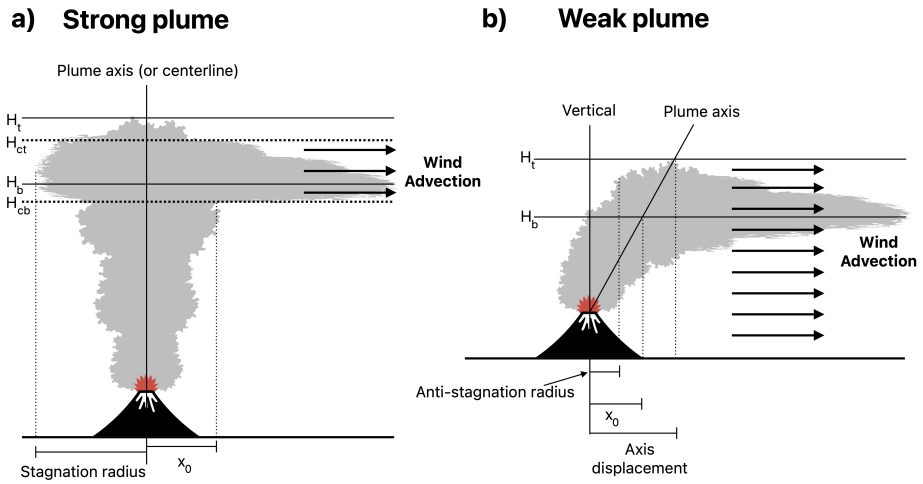

Figure 2.4: Wind-affected plumes; a) strong plume for which the ash fallout occurs selected downwind and coarse upwind; b) weak plume for which the ash fallout occur totally downwind. H_{ct} in a) is the top of the spreading current (modified from Bonadonna & Costa, 2003).

Strong plumes are characterized by a subvertical convective region and the umbrella is carried by the downwind spreading current. Weak plumes are bent-over starting to spread downwind at H_b (Fig.2.4). In a strong plume case, the umbrella region expanses radially and it reaches a stagnation point at the upwind edge, where its velocity is equal to the wind velocity. The absolute ratio W between the stagnation radius and the plume's axis displacement defines the wind effect on the volcanic plume. Ratios $W > 1$ are related to mushroomed-shaped strong plumes (Fig.2.4a), ratios $W = 1$ are related to plume upwind edge above the vent, whereas $W < 1$ describe weak plumes [11, 20].

A cross-wind on the plume produces several different effects which could influence the characteristics of the resultant fall deposits and energy injections into the atmosphere. Since most volcanic eruption plumes transect a large part of the troposphere, and many penetrate into the stratosphere, they can encounter large variations in horizontal wind speed. The convective dynamics of the volcanic plumes are complex due to the turbulence. As fluid mechanical phenomena, buoyant plumes are described by the Navier-Stokes equations. For high Reynolds number turbulent flows, the complicated and transient structures mean that it is difficult to solve these equations. Therefore, analytic methods take off the turbulence in order to focus on the centerline trajectory of the ascent plume as an axisymmetric time-averaged function of height, horizontal radius and density (PlumeRise model) [86]. Often the terms "volcanic plume" and "eruption column" are interchanged since they describe the same phenomenon. In this thesis, the term "volcanic plume" is referred to the generic ash cloud generated from an eruption and its dispersed portion into the atmosphere; instead the term "eruption column" is referred specifically to the high-convective ash cloud just above the volcano and only if its convective dynamic is recognizable. It is reasonable to assume that different volcanic plume dynamics release their energies into the atmosphere differently.

2.2 The atmosphere

The atmosphere is the propagation mean of the acoustic-gravity waves and the variation of its physical properties influence greatly the oscillation modes. An important parameter in the atmospheric studies is the *scale height* H since it indicates the altitude above which the pressure of the gas

falls by the e-factor

$$H = \frac{R_m T_0}{g_0} \tag{2.5}$$

where $R_m = \frac{R}{M_m} = 287$ J· kg^{-1}K^{-1} is the gas constant for unit mass of dry air with molar mass M_m, T_0 and g_0 are the absolute temperature and the gravity acceleration respectively at the altitude of measure, that is at the bottom of H.

The eq.(2.5) describes how the scale height is directly proportional to the temperature and it is greater for slight gases. In other words, the thickness of the atmospheric layer with a specific composition, between two pressure surfaces, is proportional to the mean temperature. Since the real atmosphere is a gas mixture characterized by temperature and compositional variations, then H is a function of the superimposition of different scale heights weighted by the fractional concentrations of the single components. The equilibrium of the atmosphere is defined as an hydrostatic balance between the gravity force and the atmospheric pressure. This means that the hydrostatic equilibrium of a volume of air between the altitudes z_0 and z_1 is defined by the *hydrostatic equation*

$$\frac{dP}{dz} = -g\rho \tag{2.6}$$

where $dP = dP_0$ - dP_1 is the difference of pressure between z_0 and z_1, $dz = z_0$ - z_1 is the height of the volume of air, g is the gravity acceleration at the center of mass, ρ is the volume density and the minus sign notes that the pressure decreases upwards.

Since $P = R_m T\rho$ then the combination of eq.(2.5) with eq.(2.6) leads to the conclusion that the atmosphere is characterized by an exponential decrease of pressure P and density ρ with altitude

$$P = P_0 exp\left(\frac{-z}{H}\right) \tag{2.7}$$

where P_0 is the pressure at some reference level, which is usually taken at the sea level $z = 0$, z is the altitude of P, H is the scale height.

Since the atmosphere is well mixed below 100 km, the pressure and density of the individual gases decrease with altitude at the same rate and eq.(2.7) is thus the same to compute the density profile. The upward exponential decrease of air density causes a progressive increase of the mean free-path Λ between particles, to be around 1 m at 120 km of altitude

$$\Lambda = \frac{1}{\pi n d^2} \tag{2.8}$$

where $\pi = 3.142$, n is the number density of the air, d is the diameter of the air particle.

Since Λ lengthens with the altitude, the interparticle collisions with a wavelength equal or greater than Λ are the ones carrying kinetic energy upward as wave propagation, and then shorter waves dissipate upward. This is a reason why the atmosphere is a dispersive medium for the acoustic-gravity waves (Fig. 2.5).

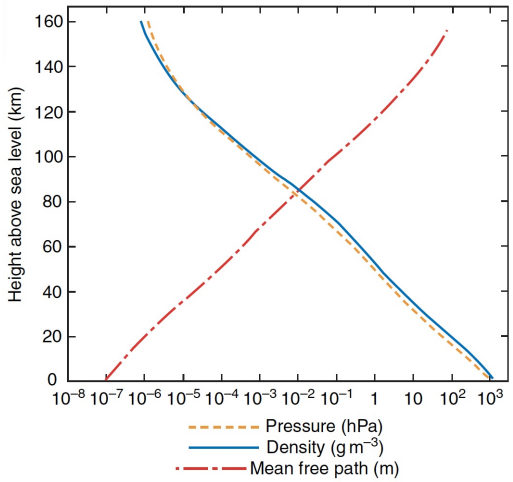

Figure 2.5: Mean free-path, pressure and density profiles of the atmosphere. It can be noted the fitting among pressure and density (from Wallace & Hibbs, 2006).

The pressure and density vertical variations are much larger than the corresponding horizontal and time variations. The atmosphere is composed of a mixture of gases maintaining similar proportions up to around 100 km of altitude. Above that altitude the gases progressively become composed by monoatomic constituents and their distribution is strongly controlled by the gravity force. The atmosphere below 100 km is called *homosphere* (or turbosphere) since the gases are well mixed by turbulence, whereas above 100 km it is called *heterosphere*, due to the stratification of the components. The homosphere is the most common concept of the atmosphere and it can be related to the concept of air. The different features of the atmosphere let us describe it from various viewpoints. Important characterizations for LAIC applications are those related to the temperature and plasma [1, 87, 101].

2.2.1 The thermal layering of the atmosphere

The atmosphere is characterized by a temperature varying with altitude and with different gradients. The atmospheric thermal gradient Γ is defined as the derivative of temperature with altitude, accompanied by the convention of the minus sign to indicate positive gradient when the temperature falls with height and negative for thermal inversion

$$\Gamma = -\frac{dT}{dz} \tag{2.9}$$

As a function of Γ, the atmosphere all the time shows thermal inversions along the altitude. These inversions set up the thermal stratification of the atmosphere in four main layers called, from the ground to the sky: *troposphere, stratosphere, mesosphere* and *thermosphere*. Between two adjacent layers, the temperature is constant for a few kilometers defining the upper limit of the atmospheric layer; this thermal-steady little stratum is the so-called "pause" of the bottom layer (Fig. 2.6). Small scales inhomogeneities of the temperature can be present into every layer.

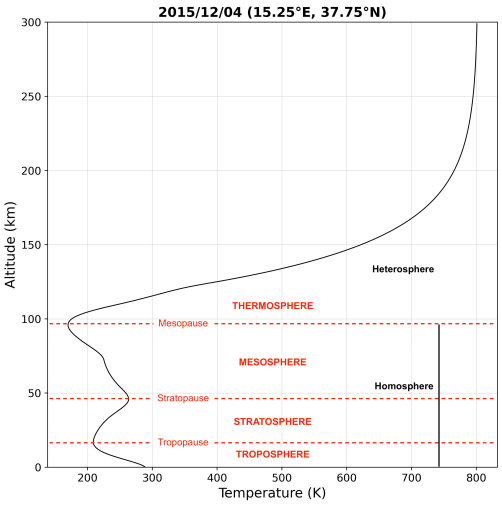

Figure 2.6: Temperature profile above Mt. Etna in December 4th 2015, at the time of the morning large-scale lava fountain.

- The troposphere is characterized by a falling temperature with height, at an average $\Gamma = 6.5$ °C/km. The positive lapse rate of the troposphere is due to two factors: 1) the thermal radiation by the ground irradiating the lower air that is then warmest than the upper air; 2) the cooling of an adiabatic rising air parcel expanding upward due to the lower pressure. The troposphere contains about 80% of the

atmospheric mass and almost all the water vapor; for this reason the troposphere is the layer in which the weather phenomena occur. The cloud droplets and ice particles of weathering continually clean the troposphere by aerosols having thus resident times around the week. The thickness of the troposphere depends on the latitude in such a way that it reduces towards the Poles. At the Equator the troposphere can be 16 - 18 km high, since the tropical thermal convection pushes the tropopause upward, whereas at the Poles the tropopause is at about 7 - 8 km. The troposphere is upper limited by the stratospheric thermal inversion.

- The stratosphere contains the 90% of the ozone O_3 reaching maximum concentrations around 15 - 35 km of altitude. The ozone absorbs the ultraviolet radiation from the Sun by producing the heating of the stratosphere and the stabilization of the typical negative gradient. The stratospheric thermal inversion strongly inhibits the vertical motions of air and the water vapor concentration drops abruptically of one order of magnitude by causing the extreme dry conditions of the stratosphere. The semi-total absence of cloud formation processes and mixing lead the aerosols into the stratosphere to have long resident times. The characteristic anvil shape, created by the spreading of tropospheric cloud tops, generated by intense thunderstorms or volcanic plumes when they reach the tropopause, is due to this strong thermal stratification. The absorption of ultraviolet radiation by the stratospheric ozone is critical for the habitability of the Earth. The stratosphere reaches its maximum temperature around 0 °C at 50 km of altitude, over which the stratopause begins. As the warmer layer, the stratosphere heats the lower mesosphere that is characterized by another thermal inversion.

- The mesosphere is characterized by a positive thermal gradient reaching the minimum temperature around -100 °C at 100 km of altitude. The strato-induced bottom high temperature facilitates, as into the troposphere, the convective air mixing.

Finally, above the mesopause, absorption of the solar radiation (UV - X bands) by molecular nitrogen N_2 and oxygen O_2 occurs, and related photodissociation and photoionization processes of the constituents lead to

the production of charged particles and the formation of a weakly ionized plasma. Therefore, above 100 km of altitude, the strong thermospheric negative gradient represents not another "simple" thermal inversion, but a new type of atmospheric environment, in such a way it is common to recognize the lower-middle neutral atmosphere from the ionized upper atmosphere [1, 101]. The atmospheric temperature profile is important for the ray-tracing modeling of acoustic-gravity waves.

2.2.1.1 Potential temperature and the parcel concept

It is common to study the atmospheric thermodynamic as adiabatic process of air parcels, in which the heat is neither gained nor lost in reversible transformations. If an air volume V, at temperature T and pressure P, is compressed adiabatically until pressure P_0, we find the potential temperature $\mathrm{T}_{\mathrm{pot}}$

$$\mathrm{T}_{\mathrm{pot}} = T\left(\frac{\mathrm{P}_0}{\mathrm{P}}\right)^k \tag{2.10}$$

where $k = \frac{\mathrm{R_m}}{c_p} \approx 0.286$ for diatomic gases (c_p is the isobaric specific heat). The potential temperature of an air parcel is constant when the mass is subject to an adiabatic change.
In adiabatic conditions and at constant pressure, as it can be approximated at a specific altitude, the pressure within parcel is equal to that of the surrounding environment, but its temperature, density and composition may differ from those of the environment. For an adiabatically rising parcel, the potential temperature and the entropy are constants, then the adiabatic lapse rate is

$$\Gamma_a = \frac{g}{c_p} = \left(\frac{\gamma - 1}{\gamma}\right)\frac{\mathrm{T}}{\mathrm{H}} \tag{2.11}$$

where g is the gravity acceleration, $\gamma = 1.4$ is the adiabatic index for diatomic gases and $\gamma = 1.6$ for monoatomic gases, T is the temperature at the ascent starting point, H is the scale height [1, 54, 100].
If a force is applied to the parcel, it arises adiabatically through a small height dz without affecting the surroundings. At the displaced position z_1 $= \mathrm{z} + dz$ the parcel temperature has increased to T_{p1} according to Γ_a

$$\mathrm{T}_{\mathrm{p1}} = \mathrm{T} + \Gamma_a dz \tag{2.12}$$

On the other hand, the environment temperature at height z_1 is T_{e1}

$$T_{e1} = T + \Gamma dz \tag{2.13}$$

The volume of air parcel going upward will displace the same volume of surrounding air. Since the adiabatic conditions, the pressure is the same inside and outside the parcel, then the volume is directly proportional to the temperature [87]. This means that the adiabatic volume change of the parcel produces a density variation from the surroundings

$$\rho_{p1} = \frac{P_1}{R_m T_{p1}} \qquad \rho_{e1} = \frac{P_1}{R_m T_{e1}} \tag{2.14}$$

The difference of density between the air parcel and the surroundings determines parcel oscillations due to the buoyancy force (i.e. Principle of Archimede). The buoyancy force and its acceleration are the fundamentals for the hydrostatic equilibrium of the atmosphere, in such a way that

$$\frac{d^2(dz)}{dt^2} = g\left(\frac{\rho_{e1}}{\rho_{p1}} - 1\right) = -\frac{g}{T}(\Gamma_a - \Gamma)dz = -N^2(dz) \tag{2.15}$$

leading to the equation of the form

$$\frac{d^2(dz)}{dt^2} + N^2(dz) = 0 \tag{2.16}$$

where

$$N^2 = \frac{g}{T}(\Gamma_a - \Gamma) = \frac{g}{T}\left(\frac{dT}{dz} + \frac{g}{c_p}\right) = \frac{g}{T_{pot}}\frac{dT_{pot}}{dz} \tag{2.17}$$

The factor N is the *angular buoyancy frequency* (or Brunt-Väisälä frequency), that is the natural oscillation frequency of the atmosphere, below which the gravity acts as restoring force for the atmospheric wave propagation. Since at constant pressure, $V \propto T$, then:

- If $T_{p1} < T_{e1} \Rightarrow \rho_{p1} > \rho_{e1} \Rightarrow N^2 > 0$ the parcel going upward is "heavier" than the surroundings, and will falls until the hydrostatic equilibrium by buoyancy oscillations at an angular frequency N. This condition occurs when $\Gamma < \Gamma_a$ and the atmosphere is called *statically stable*.

- If $T_{p1} > T_{e1} \Rightarrow \rho_{p1} < \rho_{e1} \Rightarrow N^2 < 0$ the parcel is "lighter" than the surroundings and will rise indefinitely with increasing speed. N is imaginary and leads to exponential solutions of eq.(2.16), one of which corresponds to the displacement of the parcel. This condition

occurs when $\Gamma > \Gamma_a$ and the atmosphere is called *statically unstable*. This condition occurs above erupting volcanoes.

- If $\Gamma = \Gamma_a$ the *neutral stability* occurs [1].

2.2.2 Plasma of the atmosphere: the ionosphere

Starting from about 60-90 km of altitude, the X-UV solar radiation starts to trigger photodissociation and photoionization processes of the atmospheric gases, leading to the production of ions and free electrons composing a plasma, called *ionosphere*. The electron component is in thermal equilibrium with the neutral gas only in the lower ionosphere. A decoupling of the two components already begins around 150 km with a distinctly stronger increase of the electron temperature T_e.

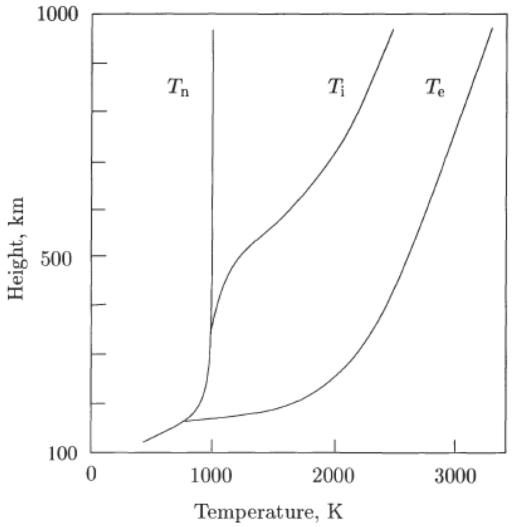

Figure 2.7: Temperature profiles of the three gas species at the ionospheric altitudes (from Prölss, 2004).

Owing to the much larger interaction cross section, the ion component stays in thermal equilibrium with the neutral gas up to an altitude of about 350 km. The ion temperature T_i above this altitude shows an increase in the direction of T_e without ever reaching it. The different temperatures of the three gas components result in a continual heat flux from the electrons to the ions and from the ions to the neutral gas. This implies that a heat source must exist above the ionosphere to maintain a downward directed heat current. This is true as long as the Sun shines, since at the nightside of the Earth the temperatures decline steeply and assimilate so that to a good approximation $T_e \simeq T_i \simeq T_n$ (T_n is the neutral temperature starting

from the troposphere) [77]. Electrons and ions represent trace gases and the upper atmosphere is only weakly ionized. Typical values for the ratio of electron number density n_e to neutral gas number density n are 10^{-8} at about 100 km, 10^{-3} at the electron density peak and 10^{-2} at about 1000 km.

The ionosphere everywhere is a quasi-neutral mixture of charge carriers, for which, at the mesoscale, the sum of the positive ions is always equal to the sum of the electrons and negative ions. However, above 90 km of altitude, the contribution of negative ions is such small that the total density of positive ions is about equal to the electron density [1, 77]. The charge neutrality is maintained by the dynamic equilibrium between the electron production and the electron reduction rates

$$\frac{dn_e}{dt} = q - \mathrm{L} - \nabla(n_e\vec{\nu}) \tag{2.18}$$

where n_e is the number density of the electrons (hereafter called electron density), q is the photoionization rate (or Chapman production function), L is the recombination rate, $\nabla(n_e\vec{\nu})$ is the loss of electrons by movement, $\vec{\nu}$ is the vector of the average drift velocity [41].

The electron density profile of the ionosphere is strongly dependent on the solar zenithal angle and the current solar activity, in such a way that around noon the peak is reached.

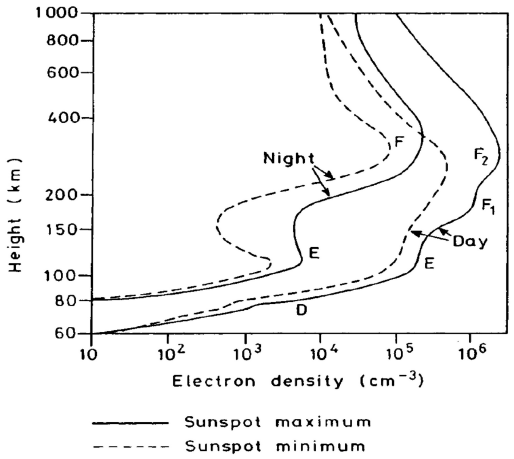

Figure 2.8: Electron density profile recovered in daytime and nighttime at the solar maximum and minimum. The electron density distribution is more articulated at the daytime of solar maximum (from Hargreaves, 1992).

The dependence of atmospheric ionization by solar activity on the Earth

leads the ionosphere at the dayside to be different from that at the nightside (Fig. 2.8). The exposure to the Sun increases q, leading to the formation of four electron density layers reducing commonly to two in the night. The permanent ionospheric layers are the E region and the F region whereas, in daytime, the photo-induced processes produce added solar-dependent layers: one at the bottom of the ionosphere, called D region, and the splitting of the F region into F1 and F2 layers [41, 56]. The molecular ions O_2^+ and NO^+ are the main components of lower ionosphere while O^+ is the primary component of the F region and of the upper ionosphere, until the direct transition to the lighters He and H^+.

- The D region is the lower and denser ionospheric layer, between 50 - 90 km without electron density peak. It is composed by O_2^+ and NO^+ but the low altitude and the presence of ions derived from the water vapor (as H_2O^+, $H_5O_2^+$, $H^+(H_2O)_n$ groups) leads the D region to have high recombination rates. Since the high recombination rates, the D region disappears at the sunset.

- The E region is between 90 - 150 km with an electron density peak $n_{e-max} \approx 10^{3\text{-}5}$ $e^-\cdot cm^{-3}$ from night to day at about 110 km. It is a Chapman layer characterized by the cuspidal distribution of the electron density, with occasional overdense ionization noted as *E-sporadic layer*. Although its electron density is highly reduced, the E region can be detected at night due to the abundance of NO^+.

- The molecular ion O_2^+ is predominant than the NO^+ but, around 150 km, the inversion of these two components occurs since the presence of N_2^+ and O^+. Furthermore, above 150 km, the lighter atomic ions start to prevail on the heaviest molecular ones, and O^+ become the predominant component of F region with a density peak at about 300 km. At daytime, the solar radiation at $\lambda < 80$ nm triggers the production of N_2^+ contributing to the maximum production rate of NO^+, and the F1 layer is produced with a peak $n_{e-max} \approx 10^{5\text{-}6}$ $e^-\cdot cm^{-3}$ at about 190 km. Going upward, the low atmospheric density leads the recombination rates to be slower than the production ones and the electron density increases along the altitude until the production of the F2 layer, with the absolute electron density peak that can excess 10^6 $e^-\cdot cm^{-3}$, during the maximum sunspot number, at about 200 - 300 km.

A layer characterized by an electron density augmentation with height, due to the drop of the recombination rate, is called Bradbury layer. However, the Bradbury layer is characterized by an undefined increase of the electron density that doesn't explain the electron reduction above the F2 layer (Fig. 2.8b). To rest the electron density increase, it is necessary to consider the *plasma transport processes* due to the magnetosphere trapping charged particles by its field lines. This means that the F2 layer originates from the dynamical equilibrium between the electron production processes and the diffusion of the charge carriers. At nighttime, the diffusion processes prevail on the total recombination ones and the electron density drops until the permanent statement of F region. The upper limit of the ionosphere is conventionally placed at 1000 km, that is the bottom of the protonosphere composed by He^+ and H^+ [41, 56, 57, 77].

2.3 The atmospheric waves

Earthquakes and tsunamis are characterized to release kinetic energy only into the atmosphere. Since the tsunamis are generated by earthquakes occurring at the ocean floors, both phenomena release the energy at the epicenter (where the energy peak occurs) and by their own characteristic wave fields (where the energy dispersion occurs). Earthquakes and tsunamis are thus dynamic sources. Volcanic eruptions and severe weathering are characterized to release mass and energy into the atmosphere. Especially the eruptions release their momentum by the volcanic plume mainly as their own epicenter, but seismic wave fields can also occur during the volcanic activity. Volcanic eruptions and tornadoes are thus thermodynamic sources that are more complex since they can occur by different combinations among their dynamic and thermal parts. When dynamic or thermodynamic sources release their power into the atmosphere, the excess energy perturbs the hydrostatic equilibrium of the air and atmospheric waves propagation occurs as the process of the atmosphere to restore the balance. Several studies about atmospheric temperature profile and air waves were developed during the '50s and '60s of the twentieth century [42, 46]. An important question is the *sound channel* determined by warm layers above colder ones in which short-period acoustic waves become trapped as they travel around the globe. The explosion (e.g. impulsive source) generates an initial spherical wave that is modified into a cylindrical wave by the layered structure of the atmosphere.

The wave can be composed of a broad spectrum ranging from audible sound to about 1000 s. The long waves of the initial pulse becomes dispersed into a train of waves as a function of the temperature and wind stratification [31, 107]. The wave dispersion into the atmosphere can be *normal* or *reverse*. The normal dispersion is due to a group velocity increasing with period, whereas the reverse dispersion is due to the group velocity decreasing with period. Reversal dispersion is related to the greater velocity into the upper layer: the greater the velocity the more pronounced is the reversal. Commonly, the train of waves exhibits normal dispersion into 1 - 5 min range that is followed by a long train of short-period waves. Reversal dispersion occurred sometimes at periods greater than 6 min. [75]. The atmospheric waves noted to be triggered from impulsive sources are the *acoustic-gravity waves* and the *Lamb waves*, and they represent the main dynamical coupling process of the lithosphere with the atmosphere.

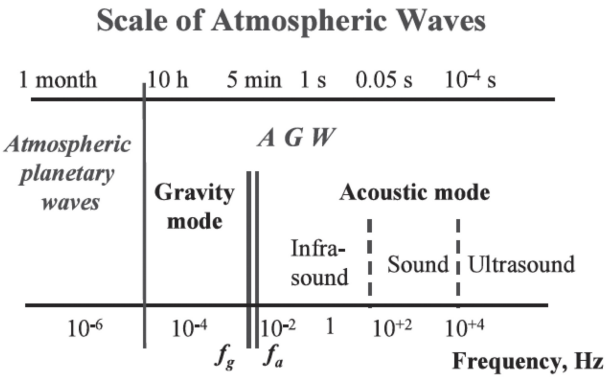

Figure 2.9: Acoustic-gravity spectrum; f_g and f_a are the Brunt-Väisälä and the cut-off acoustic frequencies respectively (from Lizunov & Hayakawa, 2004).

2.3.1 The Lamb waves

The Lamb wave, in an isothermal fluid, is the fundamental mode between the action of acoustic waves (i.e. longitudinal waves at short periods) and that of internal gravity waves (i.e. transverse waves at long periods) [81]. The wave propagation is horizontal above a rigid lower boundary with periods $>$ 100 s and velocity $v_L = \sqrt{\gamma g \mathrm{H}}$ (where γ is the adiabatic index, g is the gravity acceleration, H is the scale height at the source) [53, 65]. Lamb waves have no upward phase propagation since their energy decreases exponentially with altitude, due to the atmospheric density decrease. As a consequence, the Lamb waves are concentrated at altitudes below 30 km

while they are hydrostatically balanced in the vertical direction [72]. These waves can be generated by powerful sources and they typically arrive before the acoustic-gravity waves since the direct propagation at the greatest sound speed layer of the lower atmosphere [21]. The duration of the Lamb waves is affected by the topography and by the vertical profile of the air density [58]. Computations of the Lamb waves generation are made for a point source energy release, by assuming a viscous fluid, and the results show that as the source height falls, as the distance from the source increases or as the period extends, the Lamb wave wavelength is greatly increased (Fig. 2.10). In other words, either the source height increases or as the source energy decreases, by defining spectra of short periods (corresponding to a diminished blast wave radius and less energy into the atmosphere), Lamb wave dominance of the acoustic-gravity wave signals at close ranges is extremely unlikely [81]. Therefore, the Lamb wave is a surface atmospheric wave really constrained at the Earth's surface where no buoyancy acts. It occurs into the tropospheric scale height H due to the simultaneous horizontal large air displacement.

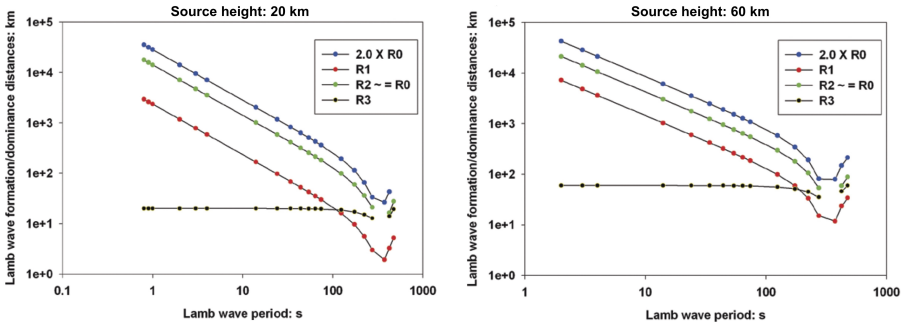

Figure 2.10: Lamb waves modeling from two different heights of the source. R0 is the Lamb wave formation distance, R1 is the Lamb wave dominance distance attributable to its amplitude, R2 and R3 are additional scaled distances to constrain the results. It can be noted the strong dependence on the source height by R0 and R1 (from ReVelle, 2010).

The Lamb wave observed in Europe from the January 15th 2022 Hunga Tonga - Hunga Ha'pai eruption (Tonga), at about 17000 km far away, has a period around 60 min, peak-to-peak amplitude of 2 hPa and $v_L \sim 295$ m·s^{-1}, that is a wavelength around 1000 km [21, 58].

2.3.2 The acoustic-gravity waves

The acoustic-gravity waves (AGWs) are the two main dispersion branches of the atmospheric waves caused by geodynamical sources. These waves

propagate into the atmosphere at periods shorter than the acoustic cut-off (τ_{a}) and longer than the air buoyancy (τ_{g}) (or Brunt-Väisälä period) [54]. The acoustic component of AGWs is then infrasound propagating as an elastic longitudinal wave in which the particle motion is in the same direction of the wave propagation, by alternating compressions and rarefactions of air. Infrasound travels at the speed of sound increasing with temperature and downwind because of advection, and depends on the type of gas.

$$c_{eff} = \sqrt{\gamma \mathrm{R_m T}} + \hat{n} \cdot \vec{u} \tag{2.19}$$

where $\gamma = 1.4$ is the adiabatic index, $\mathrm{R_m}$ is the gas constant for air mass unit, T is the absolute temperature, $\hat{n} \cdot \vec{u}$ projects the wind $\vec{u}$ in the direction from source to observer $\hat{n}$, through this inner product.
Sound propagates at about 340 m·s^{-1} at 293 °K but the wind can change this value with important implications on the sound propagation and eq.(2.19) is called *effective sound velocity* [33] (Fig. 2.11). The lower limit of infrasound is bounded by the thickness of the atmospheric layer through which it travels (Fig. 2.9). The infrasound refracts within layers where $c_{eff}(h)$ increases to values larger than the value at the ground $c_{eff}(0)$, due to the increase in downwind velocity, temperature or a combined effect [101].

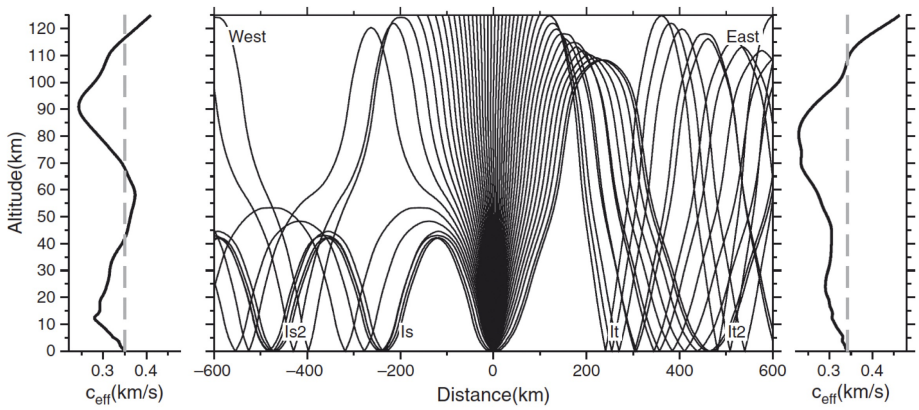

Figure 2.11: Effective velocity profiles from eq.(2.19). It can be noted the marked difference in the velocity profile due to the easterly wind. Westward of the source, downwind sound reflection occurs around 40 km of altitudes where $c_{eff}(h) > c_{eff}(0)$; eastward of the source, the sound reflection is due to the thermospheric temperature only. The terms *Is* and *It* indicates the "infrasound stratosphere" and "infrasound termosphere", respectively (from Evers & Haak, 2010).

Since the wave refraction is a function of the ray-path orientation, when the incident angle θ_i (e.g. the angle between the vertical and the ray-path) is critical, the infrasound reflects downwards by following the Snell law. This

means that the infrasound rays propagating with low θ_i penetrate the atmosphere, and as θ_i broads, the progressive refraction of the wave, until the total reflection, occurs (Fig. 2.11). On the other hand, the upwind facilitates the upward acoustic-gravity wave propagation [30]. Figure 2.11 shows the effects of the wind on the sound propagation both in case of downwind (westward) and upwind (eastward). In detail, the strict constraint due to the velocity difference between $c_{eff}(0)$ and $c_{eff}(h)$, due to the wind by eq.(2.19), is clearly represented.

The absorption of sound in atmosphere diminishes with increasing period, in such a way that the atmosphere acts as a low-pass filter of the sound with altitude. The air is very viscous at higher altitudes (130 km) due to the very large neutral gas mean free-path (Fig. 2.5) [101]. Starting from 100 km, the short periods are strongly attenuated and dissipated by the air viscosity and only periods greater than 30 - 60 s propagate into the upper atmosphere (Fig. 2.12).

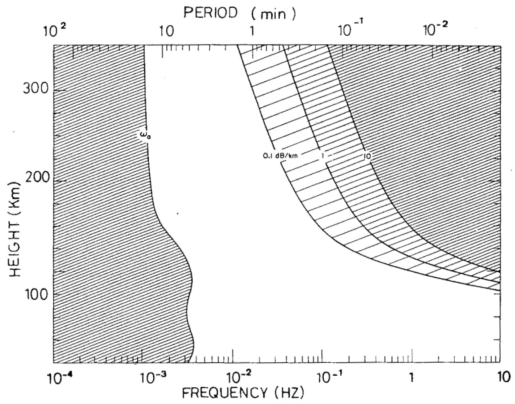

Figure 2.12: Attenuation of infrasound in the upper atmosphere. Only periods less than the cut-off ω_0 exist but the upward propagation of short periods is strongly attenuated (from Blanc, 1985).

Because of the fast attenuation drop with the period, infrasound can travel over long distances [68]. From Figure 2.12 we can infer further information of the dispersion features as follows. Since the group velocity of the wave is related to the transport of energy, then the reverse dispersion indicates important lacks of short periods (strongly attenuated along the propagation path): this means that the dispersion is a function of distance also, in such a way that the normal dispersion would characterize near-field propagation, while reverse dispersion would characterize far-field propagation.

Pfeffer & Zarichny [75] analyze the wave dispersion by starting from a no-

wind atmospheric half-space of 300 km with a rigid bottom boundary (Fig. 2.13). The step-like character of the phase velocity curves can be interpreted as being the result of interference between two families of normal modes: *quasi-horizontal* modes representing energy propagation below the ozonosphere (warm layer) and *quasi-vertical* modes representing energy propagation above the ozonosphere. This means that the quasi-horizontal modes propagate into positive thermal gradient layers, while the quasi-vertical ones penetrate the atmosphere. In a no-wind model, the temperature augmentations in stratosphere (or ozonosphere) and in thermosphere must prevent the wave energy from escaping to even greater altitudes. The wave energy penetrates high velocity layers as a function of wavelength, in such a way that the longer waves penetrate farther than the shorter ones. There are infinite modes which can satisfy the governing equations but only a small finite number are sufficient to account for the observations, that is the family of "acoustic" and "gravity" modes that are controlled by the acoustic properties of the atmosphere and by gravity respectively [75].

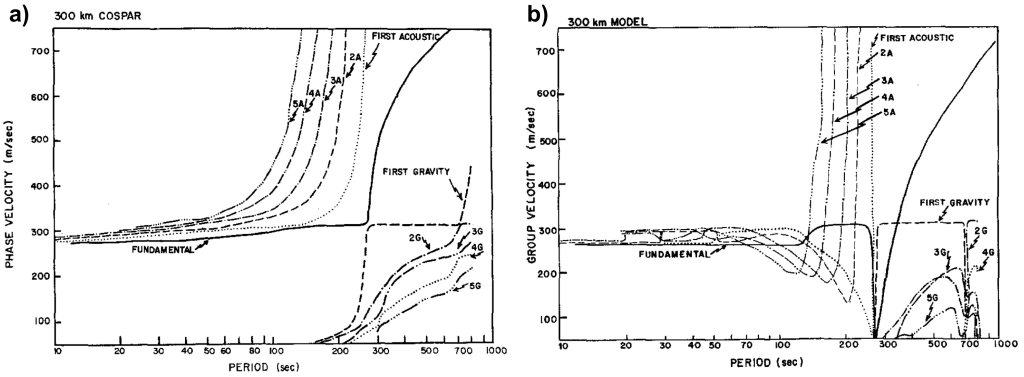

Figure 2.13: Dispersion curves of AGWs induced by impulsive source. The curves are calculated in COSPAR atmospheric model up to 300 km. Panel a) shows phase dispersion curves related to the atmospheric structure; panel b) shows group dispersion curves related to the energy propagation (modified from Pfeffer & Zarichny, 1963).

Figure 2.13 shows fundamental and higher modes of the acoustic-gravity waves that are splitted in short ($<$ 150 s), intermediate (150 - 300 s) and long ($>$ 300 s) periods. The relation between group velocity U and phase velocity V is given by

$$U = \frac{V^2}{V + \left(\frac{dV}{dt}\right)\tau} \tag{2.20}$$

where τ is the wave period in no-wind conditions.
It follows that the short-period waves are most sensitive to the small-scale

inhomogeneities of the atmospheric structure and travel in the lowest velocity layer. The intermediate-period waves are too large to be confined within either channel, their velocity is not influenced significantly by the temperature distribution above the stratosphere, and their kinetic energy decreases exponentially along the altitude. The long-period waves are sensitive only to major differences in temperature between lower and upper atmosphere and they can be confined by the thermosphere [75]. In LAIC processes and for sufficiently small structure sizes, certain "asymptotic" relations apply to the parameters describing acoustic-gravity waves such that

$$\frac{U_x}{U_z} \approx \frac{\lambda_x}{\lambda_z} \approx \frac{\tau}{\tau_g} \tag{2.21}$$

where U_x, U_z are the horizontal and vertical components of the group velocity respectively, λ_x, λ_z are the horizontal and vertical wavelengths of the wave respectively, τ is the period of the wave, τ_g is the buoyancy period [46, 58].

AGWs tend to increase their amplitude A of oscillation with increasing height h, in proportion to the amplification factor α

$$\alpha = exp\left(\frac{\gamma g h}{c^2}\right) = exp\left(\frac{h}{2H}\right) \tag{2.22}$$

where h is the coordinate measured vertically upwards.

The factor α is interpreted in terms of energy flux, since it just compensates for the upward exponential decrease of atmospheric density in maintaining the flux in those modes whose rate of energy dissipation, over a full oscillation period, would be just sufficient to exhaust the excess energy available.

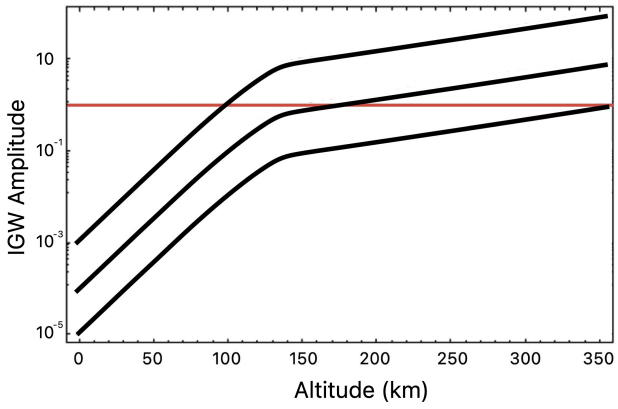

Figure 2.14: Linear approximation of amplitude - altitude relation for internal gravity waves. It can be noted the change of the amplification rate around 100 - 150 km of altitude (modified from Lizunov & Hayakawa, 2004).

The upward exponential decrease of the air density causes the viscous dissipation of the short waves and the minimal wavelength grows along the altitude. This effect, associated with the conservation of kinetic energy, leads the particle velocity to grow exponentially upward. Therefore, the atmospheric amplification implies that less dissipative modes are permitted while more dissipative ones are excluded [46, 73]. Dependence of $A^{\alpha}(z)$ is plotted in Figure 2.14. The slowing down of amplification at altitudes $z =$ 100 - 200 km is connected with the increase of the scale height H and in less grade with the increase of the vertical group velocity. Since the density variation cannot exceed physically 100%, the amplitude A = 1 is the nonlinear limit of amplification. Therefore, surface pressure oscillations < 0.1 mbar are able to originate linear AGWs at the upper limit of the E-region, with amplifications up to 10^5 in absence of wind. AGWs at higher altitudes or in E-region with higher initial amplitudes are found to be nonlinear [54].

2.3.2.1 Basic equations of acoustic-gravity waves

The step-by-step modeling of the atmosphere, from simple unrealistic conditions to realistic ones, provides us the atmospheric details controlling the acoustic-gravity waves propagation. Real local atmosphere can be defined as a compressible and vertically stratified fluid into a gravitational field where sound speed c varies along the altitude z. The compressibility of the fluid is set for parameters such that $c \neq \infty$, the density stratification is set for scale heights H $\neq \infty$ and the gravitational field is set for parameters with g $\neq 0$. The basic equations of AGWs propagation are the equations of momentum (eq.2.6), continuity (eq.2.23) and energy conservation (eq.2.24)

$$\frac{d\rho}{dt} + \rho \nabla \cdot \vec{V} = 0 \tag{2.23}$$

$$\frac{d\eta}{dt} = 0 \tag{2.24}$$

where η is the entropy of the air parcel that is conserved in adiabatic motion [38, 92].

The acoustic waves propagate in absence of a gravitational field, due to limited displacements for which gravity is inactive. Thus, the acoustic wave propagation can be treated in a density stratified and compressible fluid without gravity, where the vertical wave number k_z is equal to

$$k_z^2 = \frac{\omega^2}{c^2} - k_x^2 - \sigma^2 \qquad\qquad c \neq \infty, \sigma \neq 0, g = 0 \tag{2.25}$$

where ω is the perturbation angular frequency, c is the absolute sound speed (without wind), k_x is the horizontal wave number of the perturbation, $\sigma = \frac{1}{2\mathrm{H}}$ is the buoyancy wave number characteristic of the atmospheric stratification [92].
Since the symmetry between k_x and k_z, the propagation is isotropic, but for $\omega^2 < \sigma^2 c^2$ attenuation occurs. This angular frequency is the acoustic cut-off ω_a (ω_0 in Fig. 2.12)

$$\omega_a = \sigma c = \frac{\gamma g}{2c} \tag{2.26}$$

The acoustic cut-off ω_a is the low-frequency limit for the acoustic waves and it is a resonant frequency for propagating waves in a distributed mass-spring system; usually ω_a is related to periods around 250 - 350 seconds, as observed in Figure 2.13. The acoustic phase and group velocities are

$$V_a = \frac{\omega}{k} = c\left(1 - \frac{\omega_a^2}{\omega^2}\right)^{-\frac{1}{2}} \tag{2.27}$$

$$U_a = \frac{d\omega}{dk} = c\left(1 - \frac{\omega_a^2}{\omega^2}\right)^{\frac{1}{2}} \tag{2.28}$$

where k is the wave number. As $\omega \to \omega_a$, $V_a \to \infty$ but $U_a \to 0$. Since V_a changes for different ω, the propagation is dispersive. The group velocity represents the velocity with which the energy is propagated [92].
The internal gravity waves can be treated as adiabatic process of air parcels oscillating in an incompressible fluid, due to the absence of acoustic modes, where the vertical wave number is

$$k_z^2 = k_x^2\left(\frac{\mathrm{N}^2}{\omega^2} - 1\right) - \sigma^2 \qquad\qquad c = \infty, \sigma \neq 0, g \neq 0 \tag{2.29}$$

where $k_z < 0$ for upward displacements. It is necessary for the upward propagation that $\omega^2 < \mathrm{N}^2$, then the buoyancy limit N is related to the high-frequency cut-off for the propagating waves. To compare N with ω_a, the square root of eq. (2.17) is calculated as a function of γ

$$\mathrm{N} = \omega_g = (\gamma - 1)^{\frac{1}{2}}\frac{g}{c} \tag{2.30}$$

The wave numbers k_x and k_z are no longer symmetric and the propagation is anisotropic as well as dispersive [38, 54, 92]. Therefore, the group velocity

has horizontal U_g^x and vertical U_g^z components

$$U_g^x = \frac{d\omega}{dk_x} = \frac{k_x(\mathrm{N}^2 - \omega^2)}{\omega(k_x^2 + k_z^2 + \sigma^2)} \tag{2.31}$$

$$U_g^z = \frac{d\omega}{dk_z} = -\frac{k_z\omega^2}{\omega(k_x^2 + k_z^2 + \sigma^2)} \tag{2.32}$$

where the vertical group velocity U_g^z has an inverted sign compared to the vertical phase velocity $V_g^z = \frac{\omega}{k_z}$. This is the typical propagation condition of internal gravity waves as the atmosphere falls down by the effect of the gravity; consequently, $V_g^z < 0$ and $U_g^z > 0$ for upward energy propagation [74].

The dispersion relation of the acoustic-gravity waves reveals that any pair of real wave numbers (k_x, k_z) can be associated with either of two distinct values of the perturbation ω^2, and so with either of two values of ω if attention is confined to positive roots. One value of ω is necessarily greater than the acoustic cut-off ω_a and the other value is necessarily less than the buoyancy cut-off ω_g. This indicates that two distinct sequences of internal waves can occur: the acoustic ones at high frequencies ($\omega > \omega_a$) and the gravity ones at low frequencies ($\omega < \omega_g$) [46].

$$\frac{(\omega^2 - \omega_a^2)\omega^2}{c^2} - \omega^2(k_x^2 + k_z^2) + \omega_g^2 k_x^2 = 0 \tag{2.33}$$

Since γ value, the assumption $\omega_a > \omega_g$ is true at any condition. A gap in the frequency spectrum exists in the range $\omega_g \leq \omega \leq \omega_a$, that is for values of no-vertical phase propagation related to the Lamb waves. The effects of the gravity on the acoustic waves, or the compressibility on the internal gravity waves, is to move the solutions slightly towards each other as $k_z^2 > 0$ (Fig. 2.15).

The study of air waves within jet flows leads to recognize two downwind jet mixing noise sources: *large-scale turbulence* (LST) and *fine-scale turbulence* (FST). The LST is propelled near the jet axis while FST travels toward the ground, and both increase with the temperature. Although the FST is the main noise portion commonly detected by the ground-based networks, the LST is the component showing coherent structures as atmospheric instability waves. Different experiments on jet noise show that the acoustic intensity (e.g. mean-square pressure) from volcanic eruptions vary as a function of angle θ to the jet axis (i.e. incident angle). The dependence on θ is very strong and represent the highly directional nature of jet noise.

High temperature ratios between the jet and the surrounding atmosphere, coupled with $\theta < 50°$, could determine exponential increases of LST velocity around 3 - 4 order of magnitude than the FST one [64].

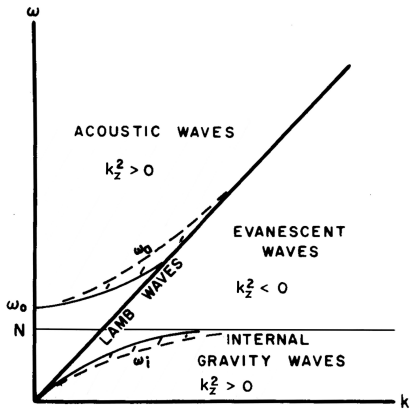

Figure 2.15: Typical $k - \omega$ diagram of the acoustic-gravity waves. The acoustic branch propagates into the atmosphere for angular frequency greater than ω_a, while the gravity one for values lesser than ω_g. The empty space between these two branches is composed of evanescent waves with no-vertical phase propagation (modified from Tolstoy, 1963).

2.4 The traveling ionospheric disturbances

Since the strong relation with the solar activity, the ionosphere is characterized by different structures as a function of the geographic latitude. In the upper atmosphere, gravity waves are observed either directly as fluctuations of the neutral gas, or indirectly as fluctuations of the ionospheric plasma which is in principle a passive tracer of the neutral gas motions. The ionospheric signature of acoustic-gravity waves (AGWs) propagating in the upper atmosphere are called Traveling Ionospheric Disturbances (TIDs) [47]. Among the ionospheric phenomena, TIDs are electron density fluctuations propagating as waves and they are classified according to their velocity and period as: Large-scale TIDs (LSTIDs), Medium-scale TIDs (MSTIDs) and Small-scale TIDs (SSTIDs) [8]. LSTIDs have horizontal propagation velocities ranging around 300 - 1000 $m \cdot s^{-1}$, horizontal wavelengths around 1000 - 3000 km and periods from 30 minutes to 3 hours; MSTIDs have horizontal propagation velocities around 100 - 300 $m \cdot s^{-1}$, horizontal wavelengths of several hundreds of km and periods around 15-60 minutes; SSTIDs having

wavelengths less than 300 km have also been observed .

LSTIDs are mainly associated with auroral and geomagnetic activity that occur at high-latitudes. During geomagnetic storms, the polar/subpolar ionosphere is prone to heating, and convection processes tend to produce strong spatially and temporally variable plasma density gradients. Such gradients form the source of LSTIDs which then propagate equatorward [8]. LSTIDs are believed to be an important mechanism by which high-latitude forcing modifies the low-latitude thermospheric density [108]. MSTIDs are mostly associated to the coupling between lower and upper atmosphere [8]. In LAIC processes, the main driver for MSTIDs is represented by AGWs propagation. In this case, the TID is the signature in the ionosphere of the passage of the AGW, that is the ions being forced along the field lines by the neutral air winds driven by the pressure waves. This means that TIDs induced by lithospheric source do not technically propagate: it is the AGW that propagates and the related TID is merely the signature of its passage. For this reason, the TIDs velocity estimable from travel time diagrams is called "apparent velocity" [5]. While the potential sources of AGWs are known, the predictability of these sources and their impacts on the thermosphere and ionosphere is matter of research [108]. TIDs induced by volcanic activity are called Co-Volcanic Ionospheric Disturbances (CVIDs) and they show different features as a function of VEI, atmospheric conditions and distance of detection ([13, 37, 59] and reference within).

Table 2.1: Characteristics of CVIDs detected by different volcanic eruptions. The velocity values are related to the "apparent velocity". Data from [28, 43, 44, 69, 79, 89, 90].

Volcano	Date	VEI	TECU	Frequency (mHz)	Velocity ($m \cdot s^{-1}$)
Asama	01/10/2004	2	0.16	~ 8	~ 1000
Soufriere-Hills	13/07/2003	3	0.5	1.4 - 4.4	460 - 760
Sarychev Peak	11-16/06/2009	4	0.03 - 0.15	3.7 - 6	700 - 1800
Kelud	13/02/2014	4	0.2 - 0.4	3.7 - 4.8 - 6.8	630 - 1200
Calbuco	22-23/04/2015	4	0.16 - 0.5	3.8 - 5.2	900 - 1300
Hunga	15/01/2022	5	4.0	3.7 - 7.4	290 - 850

Chapter 3

Data and methods

The multiparametric monitoring network around Mt. Etna represents a huge database from different sensors detecting various signals from the volcano. The analysis of different data may provide new information on our understanding of the LAIC processes related to volcanic activity. In this study, Etna's volcanic activity is analyzed by ground-based and satellite-based data. The occurrence of eruptive activity is analyzed by videocameras in visible and thermal channels, seismic and infrasonic signals as Root Mean Square (RMS) time series. The geomagnetic activity in ionosphere is evaluated by Kp and Disturbance Storm Time (Dst) indices; the electron density profile is evaluated by International Reference Ionosphere (IRI) model or ionosonde. Finally, the ionospheric forcing from Etna volcano is analyzed by total electron content (TEC) fluctuations retrieved from Global Navigation Satellite System (GNSS) data, in particular GPS data. The spectral analysis of TEC time series is carried out by Fast Fourier Transform (FFT), Continuous Wavelet transform (CWT) and Empirical Mode Decomposition (EMD).

3.1 The GNSS - TEC method

The Global Navigation Satellite Systems (GNSS) are interoperable satellite constellations that are composed of the navigation satellite systems of different Countries. The term "global" refers to the interoperability and compatibility of each individual satellite-based positioning system, ensuring geolocalization worldwide at any time. The individual satellite positioning system joining the GNSS are: NAVSTAR - GPS (United States of America), GLONASS (Russia), Galileo (Europe) and BeiDou (China).

These systems provide global coverage that can be improved as GNSS by the integration of regional systems, as QZSS (Japan) and IRNSS (India), as well as the satellite-based augmentation systems (SBAS) [48]. When the phase velocity of a wave in a medium is a function of the wave frequency, the medium is said to be "dispersive". This means that two waves, differing slightly in frequency, will travel with slightly different velocities. As a consequence, the interference pattern produced by two such waves determine where, and with what velocity, the energy in the composite wave will travel. The composite wave is the modulation envelope of all its phases and its velocity is the group velocity [29]. The ionosphere is dispersive for GNSS radio signals, and other sources of error affect the positioning. The GNSS operates in dual-frequency mode, since a linear combination of observables, on the two carrier frequencies, is needed to remove and/or minimize the positioning errors. The *ionosphere-free linear combination* removes the first order ionospheric effect and the *geometry-free linear combination* removes the geometric part of the measure, leaving all the frequency-dependent effects, multipath and noise. In ionospheric volcanology it is the ionospheric effect into the GNSS signal to be analyzed, and the dispersive property of the ionosphere provides an opportunity to estimate the total electron content (TEC) by the geometry-free linear combination of two GNSS carrier frequencies.

To obtain the TEC value, we start from the ionospheric refractive index n, that is related to the ionospheric plasma frequency $\omega_p = \left(\frac{n_e e^2}{\varepsilon_0 m}\right)^{\frac{1}{2}}$, the electron gyrofrequency $\omega_H = \frac{Be}{m}$ and the collision frequency ν

$$n^2 = 1 - \frac{X}{1 - iZ - \frac{Y_T^2}{2(1-X-iZ)} \pm \left[\frac{Y_T^4}{4(1-X-iZ)^2}\right]^{\frac{1}{2}} + Y_L^2} \tag{3.1}$$

where $X = \frac{\omega_p^2}{\omega^2}, Y = \frac{\omega_H}{\omega}, Z = \frac{\nu}{\omega}$, n_e is the electron density, $e = 1.602 \cdot 10^{-19}$ C is the charge of one electron, $m = 9.11 \cdot 10^{-31}$ kg is the mass of one electron, $\varepsilon_0 = 8.85 \cdot 10^{-12}$ $C^2 \cdot N^{-1} \cdot m^{-2}$ is the dielectric constant in vacuum, B is the magnetic field intensity, ω is the radial frequency of the radio wave, Y_L and Y_T are the ordinary (longitudinal) and extraordinary (transversal) wave polarization rays, respectively. The equation 3.1 is noted as "Appleton - Hartree formula" [29].

The carrier frequencies of GNSS signal are in L-band to make n as close as possible to unity. Indeed, $Y \ll 1$ and the absorption is negligible for L-band waves, therefore in GNSS-TEC applications it is assumed that Y, Z

$= 0$ and n reduces to the dispersive term only

$$n^2 = 1 - X \tag{3.2}$$

For realistic values of $n_e = 10^6$ e·cm^{-3} and carrier frequency $f = 1.5$ GHz, $n \approx 1$ - $(2{\cdot}10^{-5})$. That is X $\ll 1$ and eq.(3.2) can be approximated at the first order to obtain

$$n \approx 1 - \frac{X}{2} = 1 - \frac{\omega_p^2}{2\omega^2} = 1 - \frac{N_e e^2}{8\pi^2 \varepsilon_0 m f^2} = 1 - \frac{a}{f^2} n_e \tag{3.3}$$

where ω is the angular frequency of the radio wave, $a \approx 40.3$ m$^3 \cdot$ s^{-2} is the constant for positioning to convert the electron density in length units [22]. It can be noted that n is near 1 at high frequency, that is the higher the GNSS carrier frequency the lower the ionospheric dispersion. The refractive index is real and must be smaller than 1, thus when $\omega > \omega_p$ the wave phase travels faster than the light. This is not a violation of the relativity since it means that the wavelength of the phase is greater in the medium than in vacuum [29]. This statement for the phase can be verified by the travel time of a GNSS signal along the real optical path, from the satellite transmitter to the ground receiver

$$t_{travel} = \int_{rec}^{sat} \frac{n}{c} dr = \frac{1}{c} \int_{rec}^{sat} 1 - \frac{a}{f^2} n_e(r) dr \tag{3.4}$$

where $c \approx 292792$ km·s^{-1} is the speed of light.
The travel time difference relative to wave propagation in vacuum is

$$\Delta t_\Phi = t_{travel}^{medium} - t_{travel}^{vacuum} = -\frac{a}{f^2 c} \int_{rec}^{sat} n_e(r) dr \tag{3.5}$$

The minus sign means that the phase is advanced. This is not true for the group velocity, since the modulation envelope of all phases means the same for all the frequencies. Then it is convenient to define a group refractive index n' that has to be greater than 1

$$n' = \frac{c}{U} = c\frac{d\kappa}{d\omega} = \frac{1}{n} = 1 + \frac{a}{f^2} n_e \tag{3.6}$$

This means that the travel time difference relative to energy propagation in vacuum is

$$\Delta t_G = \frac{a}{f^2 c} \int_{rec}^{sat} n_e(r) dr \tag{3.7}$$

The plus sign means that the wave group is delayed. In conclusion, the ionosphere affects the GNSS signal in such a way to cause a *phase advance* equal to a *group delay*, that is Δt_Φ = - Δt_G. In other words, the phase of the GNSS carrier wave is advanced by the same amount of time that the information in a wave group is delayed. Each phase measurements is affected by an unknown ambiguity $N\lambda$ related to the initial lock onto the GNSS signal. The amount of phase advance cannot be measured on a single frequency and two coherent frequencies are required to this measure [27, 52]. The equations (3.5) and (3.7) show that the ionospheric effect induced on the GNSS signal is directly proportional to the number of free electrons between the satellite and the receiver. Then the electron density integrated along the geometric range of 1 m^2 cross-section is called *total electron content* (TEC). The TEC is expressed in TECU (TEC Unit) where 1 TECU = $1{\cdot}10^{16}$ $e{\cdot}m^{-2}$. In terms of distances, the ionospheric range delays are

$$\mathrm{I}_\Phi = c\Delta t_\Phi = -\frac{a}{f^2} sTEC \tag{3.8}$$

$$\mathrm{I}_G = c\Delta t_G = \frac{a}{f^2} sTEC \tag{3.9}$$

where $sTEC$ indicates the *slant TEC* since the integral is defined along the line-of-sight (oblique most of time).
As suggested by equations (3.3) and (3.6), the phase advance I_Φ and the group delay I_G are small for the higher carrier frequency. The real optical ray of the GNSS signal deviates from the theoretical geometrical one (straight) not only for the ionospheric effect but also for other sources of error, in such a way that the satellite-based measures of distance are called *pseudoranges* [48]. Pseudoranges are GNSS observables that can be computed by group or phase measurements as *code observables* P, based on the GNSS signal structure (e.g. coded signal), and the *phase observables* L, based on the carrier frequency, respectively. The observable P provides an absolute measure of range, robust but lesser precise than the L that is relative, phase-ambiguity affected but very precise [60].

$$P_i = \rho + c\delta t + T + I_i + b + \varepsilon_P \tag{3.10}$$

$$L_i = \rho + c\delta t + T - I_i + N\lambda_i + B + \varepsilon_L \tag{3.11}$$

where $\rho = ct$ is the satellite-receiver geometric range covered by the radio

wave if the receiver employs a clock set precisely to the satellite one, δt is the *real* clock offset between receiver reception and satellite transmission, T is the tropospheric effect, $N\lambda_i$ is the phase ambiguity for the i-frequency, ε are noise and multipath errors on L and P measurements, b and B are the differential code and interfrequency biases, respectively, due to the receiver and the transmitter hardwares.

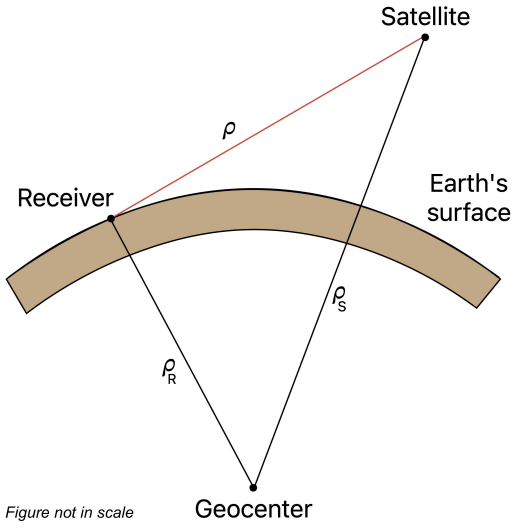

Figure 3.1: Satellite-receiver geometry configuration into a geocentric reference system; ρ is the pseudorange used for positioning, ρ_R is the constant receiver-geocenter distance, ρ_S is the satellite-geocenter distance corrected by navigational data.

Subtraction of simultaneous observations at different frequencies leads to an observable L in which all frequency-independent effects (geometrical range, clock errors, tropospheric delay ecc...) are cancelled and the ionospheric effect, together with other frequency-dependent effects, remains [22].

3.1.1 Variometric Approach for Real-time Ionosphere Observation

The Variometric Approach for Real-time Ionospheric Observation (VARION) is an algorithm based on single time differences of GNSS carrier-phase measurements in geometry-free linear combination, by using a standalone GNSS receiver and standard GNSS broadcast products. If no cycle slips occurs, $N\lambda$ can be considered constant between two consecutive epochs. The inter-frequency biases are also assumed as constant for a given period. For these reasons, differentiating eq.(3.11) between two consecutive epochs t_0 and $t_1 = t_0 + \Delta$t, and applying the geometry-free linear combination,

we obtain the observation overcoming the problem of estimating $N\lambda$ and B [84].

$$[L(t_1) - L(t_0]_{gf} = \frac{f_1^2 - f_2^2}{f_2^2} [I(t_1) - I(t_0)] \tag{3.12}$$

where the subscript gf refers to the geometry-free linear combination, f_1 and f_2 are the GNSS carrier-frequencies with $f_1 > f_2$.
Taking into account the ionospheric refraction along the geometric range, we compute the TEC variations between two consecutive epochs

$$\delta sTEC(t_1, t_0) = \frac{f_1^2 f_2^2}{A(f_1^2 - f_2^2)} [L(t_1) - L(t_0)]_{gf} \tag{3.13}$$

The equation (3.13) represents the core output of the VARION algorithm, that is the relative sTEC variation (or differential sTEC$\cdot d\mathrm{t}^{-1}$) as a single time difference of phase observables L, in geometry-free linear combination, between two next epochs at the sample period. Finally, the sTEC variations are integrated over the time axis of observation, from t_{start} to t_{end}, to retrieve the integrated differential TEC time series

$$\Delta sTEC(t_{end}, t_{start}) = \int_{t_{start}}^{t_{end}} \delta sTEC(t) \tag{3.14}$$

Since ΔTEC is an integral it is an estimation of the electron density variation and not a measure. The time series δsTEC and ΔsTEC show similar signals in the time domain but with different amplitudes to orders of magnitude. The advantage of the differential δsTEC is its high quality, since it is the direct output from GNSS record processing but it is unfiltered and trending-affected. On the other hand, the integrated ΔsTEC can be filtered and then detrended. Usually TEC amplitudes are referred to the integrated values. The single-time difference computation, from standalone GNSS receivers, makes VARION suitable for real-time applications. Nowadays, VARION is effectively used to study various types of ionospheric disturbances [3, 59, 80, 84].

3.1.2 The GNSS - TEC satellite geometry

The equation (3.14) requires a point into the satellite-receiver line-of-sight to refer the value of TEC estimation. Most of TEC value is attributable to the electron density peak and then it is assumed that most contribute, into the TEC variation, is due to electron density peak fluctuations. This

assumption is based to the fact that, at the electron density peak altitude, the ionosphere is more sensitive to the energy propagation and the ionospheric effect should then more pronounced. For this reason, usually TEC estimations are referred at the electron density peak altitude h_mF2 in daytime (Fig. 2.8) by assuming the whole ionosphere as a thin layer called *ionospheric shell*.

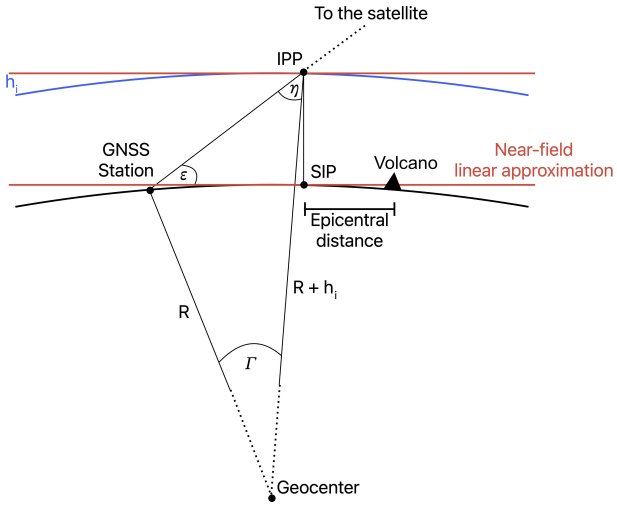

Figure 3.2: TEC-2D geometry configuration in linear approximation; h_i is the ionospheric shell altitude.

The intersection between the ionospheric shell and the line-of-sight is the Ionospheric Pierce Point (IPP), that is the point to refer the ΔTEC estimation. Therefore, TEC estimations are usually plotted around 300 km of altitude. Finally, the orthogonal projection on the ground of IPP is called Sub-Ionospheric pierce Point (SIP). The SIPs are used to mapping TEC time series of eq.(3.14), as a function of longitude and latitude, along the observation arc. The satellite geometry influences the estimation of TEC values by the IPP velocity v_{ipp} and by the sounding configuration of the three elements (receiver, IPP and source) in the XZ plane (X = horizontal axis; Z = vertical axis) (Fig.3.2). The IPP velocity is due to the satellite moving along the observation arc and then it depends on the elevation angle ε by an inverse relation, in such a way that the higher ε the lower v_{ipp}. Another implication of v_{ipp} can be the Doppler shift of the TEC signature's spectral frequency and corrections are made to retrieve the intrinsic values of the signature. Therefore the signal-to-noise ratio (S/N), into TEC time series, is higher for high ε and low v_{ipp}; conversely ε and v_{ipp} for lower S/N.

$$v_{ipp} = \frac{d_{ipp}}{dt} = \frac{\sqrt{[r_{t0}\cos(\varepsilon_{t0}) - r_{t1}\cos(\varepsilon_{t1})]^2 + [r_{t0}\sin(\varepsilon_{t0}) - r_{t1}\sin(\varepsilon_{t1})]^2}}{dt} \tag{3.15}$$

$$r = (\mathrm{R} + h_i)\cos(\eta) - \mathrm{R}\sin(\varepsilon) \tag{3.16}$$

$$\eta = \arcsin\left[\frac{\mathrm{R}}{\mathrm{R} + h_i}\cos(\varepsilon)\right] \tag{3.17}$$

where d_{ipp} is the IPP distance covered between t_0 and t_1, $dt = t_1 - t_0$ is the GNSS sample period in seconds, ε_{t_0} is the elevation angle at time t_0, η_{t_0} is the angle "station - IPP - geocentre" at t_0, R is the Earth radius, h_i is the ionospheric shell height (Fig. 3.2, 3.4) [83].
The direction δ_{ipp} of d_{ipp} is related to the IPP azimuth from the source. In a period $\Delta t = t_1 - t_0$, the IPP treads an unknown distance a from the volcano's zenith point Z, that is possible to calculate as linear distance by the cosine theorem

$$a^2 = b^2 + c^2 - 2bc \cdot \cos(\alpha) \tag{3.18}$$

where a, b, c are the sides of a generic triangle, α is the opposite angle of a (Fig. 3.3). Since VARION data processing provides as outputs the distances $b = \overline{IPP(t_0) - Z}$ and $c = \overline{IPP(t_1) - Z}$, and their azimuth angles α_0 and α_1 at the times t_0 and t_1, respectively, then $\alpha = |\alpha_0 - \alpha_1|$ and $a = \overline{IPP(t_0) - IPP(t_1)} = d_{ipp}$ from eq.(3.18) are obtained.

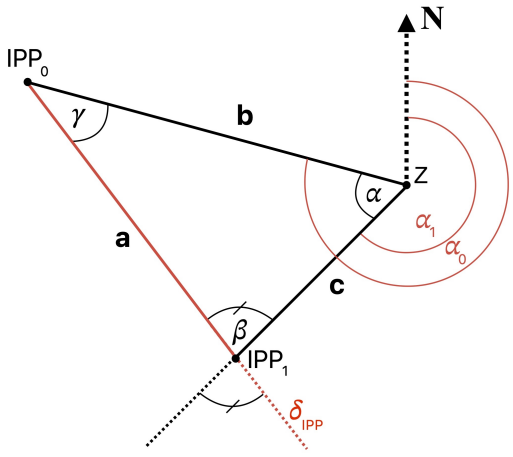

Figure 3.3: Elements of the cosine theorem.

Once obtained a, by manipulation of eq.(3.18) it is possible to obtain the angle β related to δ_{ipp}. Finally, by the pair angles theorem, it follows that $\delta_{ipp} = \alpha_1 - \beta$.

On the other hand, the ideal sounding configuration for the ionospheric TEC is to have the IPP between the station and the source in the XZ plane, in order to record the same phase of TEC fluctuation [28, 61]. In reality, the TEC sounding by satellite depends on the actual orbit during the satellite revisit time and on the relative positions of the receiver and the source from the IPP track. This means that when the signal triggering doesn't occur at the ideal configuration, it can be possible to analyze TEC time series affected by low S/N ratios. Another detail of the GNSS - TEC method is its IPP geometric convention implying two critical questions: 1) the fixed, necessary, ionospheric shell altitude implies a spatial distortion of the length of the SIP track plots, since the satellite in the same time covers different horizontal distances as a function of the IPP altitude; 2) electron density fluctuations, that may be related to different altitudes, are anyway referred to the ionospheric shell (Fig. 3.4). Therefore, the GNSS-TEC method provides reliable detection in time but the spatial information must be supplied with complementary approaches to get complete time-spatial information of the TEC signatures.

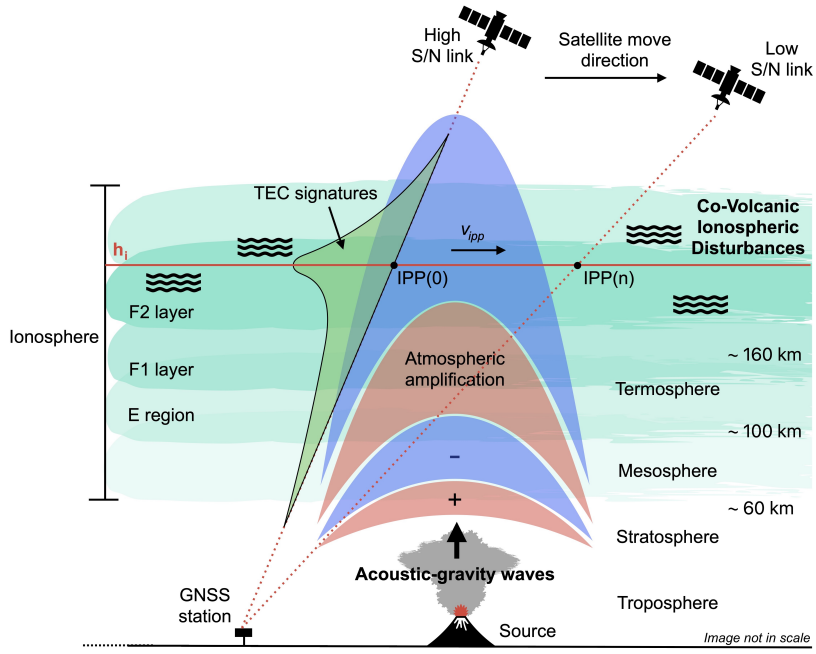

Figure 3.4: Elements of the GNSS - TEC satellite geometry. The figure is not in scale.

3.1.3 GNSS dataset arrangement

The compatibility and interoperability of each individual positioning system, forming GNSS, are based on the usage of a single data format that can be exchanged and read in the same routine by different systems. The data format in which the GNSS receivers store the observations is the Receiver Independent Exchange data format (RINEX) that can be handled with different softwares as "teqc" or "gfzrnx" [32, 71]. In this study, the RINEX data are in daily 2.11 version and they are retrieved from four different GNSS networks:

- RING network (Rete Integrata Nazionale GNSS) run by INGV [82]
- Local GNSS monitoring network run by INGV-OE (ct.ingv.it)
- ®Topcon Positioning Systems network (topconpositioning.com)
- Geodetic Data Archive Facility (GeoDAF) of EUREF Permanent GNSS Network Italian branch run by Italian Space Agency (ASI) [39]

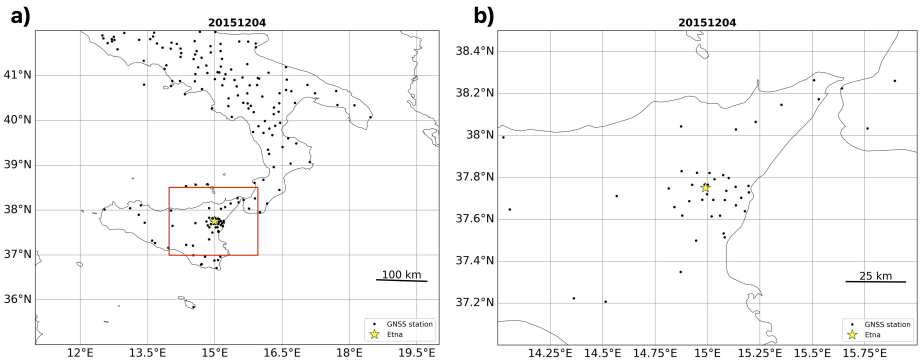

Figure 3.5: GNSS network available on December 4th 2015; a) GNSS stations as black dots within 600 km of Mt. Etna; b) local GNSS network around Mt. Etna as the magnification of the red line square in a).

Most of the data comes from RING and ®Topcon networks. The networks are continually monitored and updated and this means that the total number of the adopted GNSS receivers can be different between two eruptions occurring in different periods (Fig. 3.5). In general, the study is carried out on more than 100 receivers from RING network, around 60 receivers from ®Topcon, around 30 from Local network and around 10 from GeoDAF. In some events, GeoDAF data are not present. The GNSS receivers from these networks are selected within 600 km of Mt. Etna.
Before any analysis of TEC time series, information of GNSS receiver coordinates, and phase measurements, must be retrieved by dedicated routines.

This type of routine is the application of GNSS-TEC method, in which model parameters (e.g. ionospheric shell height h_i, carrier frequencies, geodetic specifications) are set in VARION that runs on all the satellite-station pairs of the dataset to obtain: time, SIP longitude, SIP latitude, SIP azimuth, Line-Of-Sight (LOS) elevation angle, δsTEC. SIPs longitude, latitude and azimuth are model-dependent since they change as h_i changes.

```
# SECOND        TIMING      vTEC        EPICENTRAL DISTANCE     AZIMUTH     LOS_ANGLE
58500.0, 16.25, 0.27525853283323315, 286.62344311763883, 308.3655870167202, 44.27544918414356
58530.0, 16.258333333333333, 0.2614123439390593, 284.9664911160959, 308.5852192131712, 44.44975758913466
58560.0, 16.266666666666666, 0.254728699990254, 283.31273023241243, 308.80529292049226, 44.62420755515679
58590.0, 16.275, 0.2468553159126693, 281.7670241352, 309.0258297788571, 44.79881640404351
58620.0, 16.283333333333335, 0.2359336303636646427, 280.1182747512898, 309.2469605381054, 44.97372592671914
58650.0, 16.291666666666668, 0.2358431733699397, 278.47320192975184, 309.4684881359168, 45.14870079670062
58680.0, 16.3, 0.2370517567102782, 276.93483644347623, 309.690538883794, 45.32387737248824
58710.0, 16.308333333333334, 0.22098145554849555, 275.2945159920403, 309.9132230639303, 45.49937041912182
58740.0, 16.316666666666666, 0.19129777380486013, 273.70902992770465, 310.1363890845337, 45.67499884891012
58770.0, 16.325, 0.15415814571054745, 272.1268842133057, 310.3599821655524, 45.85069343499924
58800.0, 16.333333333333332, 0.11031182291405306, 270.5466291379323, 310.58423720182265, 46.02670624224684
58830.0, 16.341666666666665, 0.06965649702364779, 268.96932678110556, 310.80900034525285, 46.20285639924256
58860.0, 16.35, 0.03558253154017951, 267.44564520116364, 311.03429606378705, 46.37916170420102
58890.0, 16.358333333333334, -0.002286289290440113 3, 265.82251125942804, 311.26026250166336, 46.55576233309166
58920.0, 16.366666666666667, -0.042416374122487 28, 264.3039312443757, 311.48669464458 62, 46.73242556985357
58950.0, 16.375, -0.07232885329346611, 262.7876322746478, 311.7137241118455, 46.90928414530228
58980.0, 16.383333333333333, -0.095178887730546, 261.2229649779052, 311.9414719244307, 47.08645583971806
59010.0, 16.391666666666666, -0.12270224513372374, 259.66137259296306, 312.16977601178917, 47.26375665294898
59040.0, 16.4, -0.14822331080976958, 258.15285414070956, 312.39858059249707, 47.44111850074395
```

Figure 3.6: Output in ".txt file" of 20 samples by the VARION first run on RINEX data for a single satellite-station pair. The seconds are in second-of-day format and the time is in 24 hr decimal format. The SIP epicentral distances from the source are obtained by the SIP latitude and SIP longitude.

Some of these space-time information are then combined for mapping; the SIP coordinates are used to compute the *epicentral distance* between SIP and source, whereas δsTEC is converted to vertical component δvTEC by eq.(4.1). These time-space information, obtained by the first run of VARION, are stored in a ".txt file" (Fig. 3.6). The first run returns time-space information of differential TEC estimations from all satellites in line-of-sight with the GNSS network on 24 hours. Some of these information are related to a different time than the eruption occurrence, then it is now possible to reduce the time axis to find the satellites S_x (x = 1, 2, ..., n) being in transmission with the receivers R_x during the eruption. In order to recognize the satellites S_x, a reference station R_0 is chosen close to the source. This means that all the satellites, in line-of-sight with R_0 during the eruption, make a list of satellites S_x that have recorded any potential co-volcanic ionospheric disturbances. The satellites S_x are selected by plotting a skyplot centered at R_0 on the time axis of interest (Fig. 3.7b). Once recognized the satellites S_x transiting close to the source during the eruption, a list of receivers R_x within a certain distance from the source is made. At this point, the specific GNSS dataset (i.e. composed by specific S-R pairs) for TEC analysis on the eruption is complete.

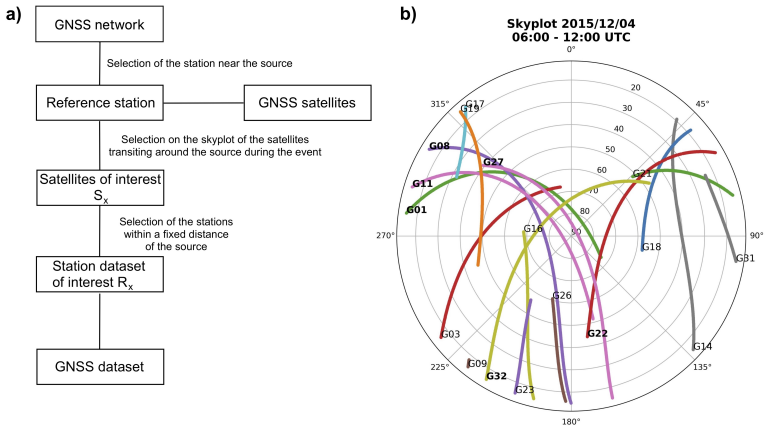

Figure 3.7: a) work-flow for the GNSS dataset arrangement; b) skyplot of the transiting satellites around Etna between 6 - 12 AM. The letter G of the satellites in b) indicates GPS satellite that are associated with their identity number. The bold satellites G08, G11, G22, G27 and G32 are selected since they are transiting around the volcano during the morning eruption of December 4^{th} 2015.

3.2 Geomagnetic indices and the electron density profile

In order to know the ionospheric conditions at the time of analysis, the global geomagnetic activity is evaluated by the Disturbance Storm Time (Dst) and the Kp indices. The Dst index is related to the H-component of the magnetic field derived from a network of near-equatorial geomagnetic observatories, and it represents the parallel disturbance field with respect to the dipole axis. As a function of time, Dst index provides the occurrences of geomagnetic storms. Even in absence of distinct geomagnetic activity, Dst index will continuously report disturbances that can be correlated with other solar and geophysical parameters. It is for these purposes that the Dst index is published on a continuous basis [104]. The Kp index varies between 0 - 9 and it represents all irregular disturbances of the geomagnetic field caused by solar particle radiation within 3 hours interval concerned. As an indication of the geomagnetic activity instantaneously driven by the solar wind, the X-Y components are measured as K index by a network of sub-auroral geomagnetic observatories. The average of K indices is the Kp index as a planetary scale measurement of the geomagnetic activity from high latitudes [6, 66]. The monitoring of geomagnetic activity on the Earth is focused on the risk mitigation related to space weather dynamics that can affect radio-based applications and their electronic infrastructures, like those related to satellites, telecommunication, internet and power plants. For

example, the Mother's Day geomagnetic storm that occurred on May 10^{th} 2024 is among the most spectacular and severe storms of the last 500 years. Dst and Kp indices have reached values around -400 nT and 9, respectively, that caused blackout and degradation of satellite communication at different orbits for a few hours [23]. Table 3.1 reports the scales of Dst and Kp geomagnetic indices.

Table 3.1: Geomagnetic activity evaluated by Dst and Kp indices.

Description	Dst (nT)	Kp
Quiet	$>$ - 30	0 - 3
Weak storm	- 50 $<$ Dst $<$ - 30	3 - 4
Moderate storm	- 100 $<$ Dst $<$ - 50	4 - 6
Strong storm	- 200 $<$ Dst $<$ -100	6 - 7
Super storm	$<$ - 200	$\geq$ 7

The electron density profile of the ionosphere is fundamental to estimate TEC values from GNSS data. The High Frequency (HF) vertical sounding of the ionosphere is performed by ionosondes at the ground to obtain direct measures of the electron density distribution along the altitude. The HF sounding is based on the travel time that is requested for a transmitted radio wave from the ionosonde to return on the ground, after being reflected at the altitude where the ionospheric plasma frequency f_p is equal to the wave frequency f. Another method to obtain information on the electron density profile is to examine the International Reference Ionosphere (IRI) model. IRI is an empirical model being based on ground and space observations of the ionosphere. Being a data-based model, the reliability of IRI depends on the spatial and temporal coverage provided by the underlying datasets. A large availability of data at mid latitudes assures a corresponding good accuracy, whereas the performance is not so good in regions at high and low latitudes since the data availability is not comparable to that at mid latitudes. The IRI model represents monthly averages of the electron density, electron temperature, ion temperature, ion composition along the altitude range of 60 - 2000 km. Additional IRI outputs include the vertical TEC (vTEC) from the lower boundary to a user-specified upper boundary, vertical ion drift near the magnetic equator and the probability of occurrence for electron density layer spreading that is related to geomagnetic phenomena [9]. In this study, IRI model provides the electron density profile only, since vTEC is obtained as differential dvTEC from GNSS data.

3.3 Seismo-acoustic monitoring of Mt. Etna

Nowadays, Mt. Etna is monitored by a network of 28 seismometers (broadband 3-component Nanometrics® Trillium 40 with sample frequency at 100 Hz) that are used to define a level of concern color code, and transmit eruption warnings to the Italian Civil Aviation Authority (VONA advices) and the Department of Civil Protection. The acoustic activity is monitored by a network of 9 microphones (G.R.A.S.® 40AN with flat response in 0.3 - 20 Hz range and sample frequency at 50 or 100 Hz). The seismometers are located very close (a few meters) to the infrasound sensors and then it is common calling "seismo-acoustic stations" this type of instrumental configuration [88, 109]. The INGV seismo-acoustic network installed at the Etna volcano is the main portion of the Permanent Seismic Network (RSP) dedicated to the monitoring of Calabria peninsula, Eastern Sicily, Eolian and Pantelleria islands (Italy) (INGV-OE - Seismic monitoring).

3.4 Spectral analysis techniques

Nowadays, the digitalization of signals lead us to analyze time series by various techniques. Most signals of practical interest can be decomposed into a sum of sinusoidal signal components that is called *spectrum*. These decompositions are extremely important in the analysis of Linear-Time Invariant (LTI) systems because the response of an LTI system, to a sinusoidal input signal, is a sinusoid of the same frequency but of different amplitude or phase. The linearity property of the LTI systems implies that a linear sum of sinusoidal components, at the input, produces a similar linear sum of sinusoidal components at the output, which differs only in amplitude and phase from the input sinusoids. Only the class of sinusoidal signals possess the property in passing through an LTI system, and for this reason the sinusoidal decomposition of signals is very important to analyze natural phenomena [76]. Techniques like Fast Fourier Transform (FFT), Continuous Wavelet Transform (CWT), Empirical Mode Decomposition (EMD) decompose the time series of the input signal by different approaches.
The basic mathematical representation of periodic signals is the *Fourier series*, which is a linear weighted sum of harmonically related sinusoids

$$x(t) = \sum_{k=-\infty}^{\infty} c_k e^{j2\pi k F_0 t} \tag{3.19}$$

where $x(t)$ is the signal amplitude in the time domain, c_k is the coefficient specifying the shape of the waveform, j is the imaginary unit, $k = (0, \pm 1, \pm 2, ...)$ is the harmonic index, F_0 is the fundamental frequency of $x(t)$, t is the time.
The periodic signal $x(t)$ with period T_0 can be represented by the series 3.19, where F_0 is the reciprocal of T_0. If the period of $x(t)$ increases without limit, the line spacing of its spectrum tends towards zero, that is the signal becomes aperiodic and its spectrum becomes continuous. The spectrum of aperiodic signals is the envelope of the line spectrum in the corresponding periodic signal obtained by repeating the aperiodic signal with some period T_p. This statement leads us to define a function $X(F)$, called the *Fourier transform* of $x(t)$

$$X(F) = \int_{-\infty}^{\infty} x(t) e^{-j2\pi F_t dt} \tag{3.20}$$

The Fourier transform is a function of the continuous variable F that doesn't depend on T_p or F_0. The essential difference, between the Fourier series and the Fourier transform, is that the spectrum in the latter case is continuous and hence the synthesis of an aperiodic signal from its spectrum is accomplished by means of integration instead of summation. If a signal $x(t)$ is absolutely integrable, it will also have finite energy. Nearly all finite energy signals have a Fourier transform. The eq.(3.20) is called Discrete Fourier Transform (DFT) since it is the mathematical formalism to convert discrete signals from the time domain to the frequency one. The Fast Fourier Transform (FFT) indicates the high performing algorithm optimizing the computation of eq.(3.20) [25].
In contrast to the Fourier transform, the *Wavelet* transform keeps the locality present in the signal and allows the local reconstruction of a signal. To be called a "wavelet", the analyzing function should be an integrable function with average equal to zero. This function, also noted as "mother wavelet", is characterized by a specific central frequency. From the mother wavelet, the scale decomposition of a signal is performed by the generation of the family of continuously translated, dilated and rotated wavelets.

$$\psi_{lx'\theta}(x) = l^{-\frac{n}{2}} \psi \left[\Omega^{-1}(\theta) \frac{x - x'}{l} \right] \tag{3.21}$$

where ψ is the mother wavelet, $l \in \Re^+$ is the scale dilation parameter corresponding to the width of the wavelet (e.g. the period in time axis), $x' \in \Re^n$ is the translation parameter corresponding to the position of the wavelet, Ω is the rotation matrix depending on the $n(n-1)/2$ Euler angles θ. The parameter l and x' are dimensionless variables, the factor $l^{-\frac{n}{2}}$ is a normalization causing all the wavelets to have the same energy and the wavelet coefficients will correspond to energy densities. The family of analyzing wavelets $\psi_{lx'\theta}$ may be compared to a mathematical microscope and polarizer, for which ψ characterizes the optics, l^{-1} is the resolution, x' the position and θ the polarization angle. Different mother wavelets are available and some of them can be performed as Discrete Wavelet Transform (DWT) and Continuous Wavelet Transform (CWT). The output of the Wavelet transform is a two-dimensional result providing information in the frequency as well as in time domains [34].
Unlike the Fourier transform operating under the assumptions that the spectral components remain constant over time, and the assumption that Wavelet transform coefficients are computed from the stretching and shrinkage of the same mother wavelet, the Empirical Mode Decomposition (EMD) is an adaptive method decomposing a signal into intrinsic mode functions (IMFs) that are based on the local characteristics of the signal, without making assumptions regarding stationary or linearity. The time series of the input signal $x(t)$ is decomposed into a finite number n of intrinsic mode functions and a residual r_n by an adaptive basis that is derived from the maximum and minor envelopes of each IMF.

$$x(t) = \sum_{j=0}^{n-1} IMF(t)_j + r_n \tag{3.22}$$

For a given time series, each IMF has its own timescale and represents an oscillation with both amplitude and frequency modulations. This type of empirical decomposition is local and orthogonal, in such a way to yield the instantaneous phase and the instantaneous frequency $\mathrm{IF_j(t)}$. By the so-called *sifting* of eq.(3.22), the EMD returns already filtered and detrended IMFs [17, 49].

Chapter 4

The December 4^{th} 2015 eruption

The large-scale lava fountains (LSLF) of Etna volcano are hazardous paroxysmal activities for the surroundings and the air traffic on the eastern side of Sicily island, Italy. Usually, this type of eruption occurs at the Voragine (VOR) crater and the fire fountains of December 2015 are among the strongest explosive activities in the twenty-first century. The December LSLFs occurred four times between the night of December 3^{rd} and the afternoon of December 5^{th}, in a 38 hr time range. This LSLF sequence is characterized by an intensity decrease from the first to the last episode [26]. Despite the mass eruption rate Q is not the highest one among the four fire fountains, Co-Volcanic Ionospheric Disturbances (CVIDs) are observed as TEC signatures during the morning eruption of December 4^{th} 2015 [37]. Figure 4.1 shows three screenshots of the large-scale lava fountain in visible (up) and thermal (down) channels from the videocamera ENT, sited in Nicolosi (37.61 °N - 15.02 °E), at around 15 km southward VOR. The visible channel provides information on the volcanic plume while the thermal channel provides information about the fire fountain. The panels on the left show the start of the eruption at 08:40 UTC that is characterized by the tephra emission onset in the air; at this moment, the plume is not present in atmosphere and the fire fountain is approaching to exit from the vent. A thermal anomaly is already present at the top of the ground. The panels in the middle show the lower part of the eruption column that is sustained by the large-scale lava fountain reaching its maximum height; the eruptive activity shows features of maximum intensity, thus it is reasonable to hypothesize that the atmospheric perturbation is maximized around this

Figure 4.1: Screenshots of the morning December 4th 2015 eruption from videocamera. The upper panels show images in the visible channel while the low ones show images in the thermal channel. The white line indicates the height unit of the videocamera. From the left to the right the screenshots show the onset of the eruption, the fire fountain at the highest altitude, the fire fountain when it starts to decrease.

moment. The panels on the right show the eruption column starting to bend since the fire fountain starts to decrease and the plume is not more sustained from below. In detail, the maximum energy release in the atmosphere is supposed to occur when the lava fountain reaches the highest altitude by producing a sustained eruption column (Fig. 4.1, panels in the middle). The eruption occurred between 08:40 and 11:00 UTC, with a plume height $h = 13.1$ km of altitude. This lava fountain has a maximum mass eruption rate $Q_{max} = 1.62 \cdot 10^6$ kg·s^{-1} that is the second highest value among the four December lava fountains. The nighttime occurrence and the low Q may be the reasons why similar CVIDs, during the other three episodes, aren't observed [67, 98].

4.1 The seismo-acoustic activity

The root-mean-square (RMS) amplitudes of the seismic and acoustic signals help to better define the time range of the eruption in comparison with that observed by video. In particular, the seismo-acoustic signals provide information about ground and air motions due to the eruption, in such a way to compare the timing of eruptive energy release with the timing estimated by the visual observation of the eruptive activity. Furthermore,

the seismo-acoustic signals can report any time sub-intervals of different phases of the same eruptive activity that cannot be watched from video. The seismo-acoustic time series, recorded by ESLN station (37.69 °N - 14.97 °E) at 7 km southward VOR, has a typical *waxing-waning behavior* starting to increase at 08:40 UTC, peaks at 10:00 UTC and ending at 11:00 UTC (Fig. 4.2). The seismo-acoustic onset of the eruption is characterized by an explosion quake coinciding with the ash emission onset (Fig. 4.1; panels on the left).

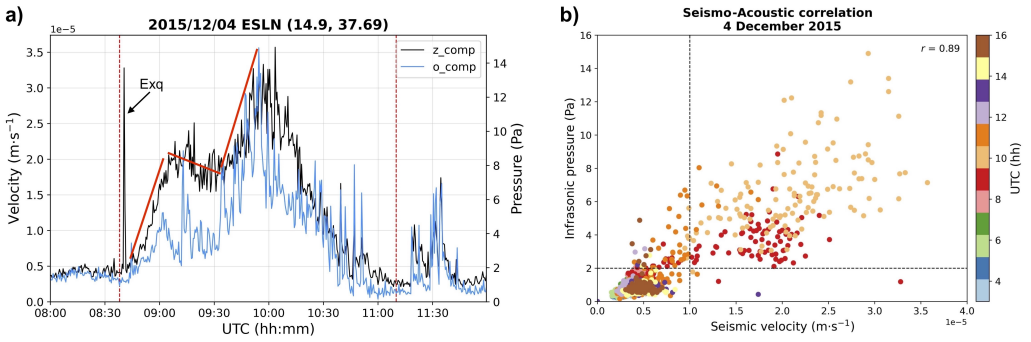

Figure 4.2: a) seismo-acoustic RMS amplitude time series; z-comp is the seismic velocity vertical component; o-comp is the infrasound signal; the high seismic peak early after the onset is the explosion quake Exq; b) linear correlation of the seismo-acoustic time series in a). The red dashed lines in a) indicate the start and the end of the seismo-acoustic activity. The three red solid lines in a) indicate the two rising ramps and the central flat-step. The perpendicular black dashed lines in b) define the seismo-acoustic field of the eruption.

The importance of seismo-acoustic time series is represented on what happens into the waxing phase, that is between the onset at 08:40 UTC and the peak at 10:00 UTC. The waxing phase is characterized by two ramps with similar seismic velocity rates $a_{tr} \approx 1.7 \cdot 10^{-8}$ m·s^{-2} that are spaced by a flat step Δt $\sim$ 09:05 - 09:45 UTC with rate $a_{tr} \approx 0$. Since the fire fountain reaches the highest height around 09:08 UTC (Fig. 4.1; panels in the middle) it is reasonable to state that the seismic flat step Δt represents the time range of the more intensive energy release in the atmosphere. An explanation to this statement is that when the fire fountain goes out from the crater, the ground shaking stops and the amplitude of the seismic signal (black line in Fig. 4.2a) decreases. The flat step is again reported by the infrasonic time series (blue line in Fig. 4.2a) with an important peak around 09:10 UTC that it is to associate to the exploit of the tall fire fountain. Although the infrasonic time series shows a less marked flat step than the seismic one, both signals are characterized by the same trend that is attributable to the same source (e.g. the eruption). Finally, despite the seismo-acoustic

peak indicates the maximum seismo-acoustic energy, starting from 10:00 UTC the waning phase occurs. This means that the seismo-acoustic peak coincides with the incipient bending of the eruption column due to the fire fountain starting to decrease (Fig. 4.1; panels on the right). Therefore, the amplitudes of seismo-acoustic time series reach the pre-eruption values around 11:00 UTC defining the seismo-acoustic end of the eruption.
To investigate the ground-air coupling in the surrounding of the crater, a linear correlation between the seismic velocity vertical component and the infrasonic signal is computed between 03:00 and 16:00 UTC (Fig. 4.2b). This time range is evaluated from video analysis and from the seismo-acoustic time series itself, in such a way to include noise of pre- and post activity to validate the correlation. The seismo-acoustic correlation yields a Pearson coefficient $r = 0.89$ indicating a volcanic conduit releasing quite directly the underground seismic energy into the atmosphere as infrasound. In particular, the seismo-acoustic correlation plot is characterized by one main cluster at lower seismo-acoustic amplitudes and one minor cluster (red and gold dots), around 09:00 - 10:00 UTC, at seismic velocity values exceeding $1{\cdot}10^{-5}$ m·s^{-1} and at infrasonic pressure values exceeding 2 Pa. Therefore, the seismo-acoustic amplitudes of the minor cluster at that time represent the seismo-acoustic field of the large-scale lava fountain (Fig. 4.2b).

4.2 The ionospheric TEC analysis

The High Frequency (HF) vertical sounding of the ionosphere, with time resolution of 15 minutes, returns an electron density peak altitude $h_mF2 =$ 220 km at 09:00 UTC for the December 4$^{\text{th}}$ 2015. The ionosonde, property of INGV, is located in Gibilmanna (37.99 °N - 14.02 °E), Italy, at about 90 km northwest of Etna volcano [95]. In this case, the electron density layering of the ionosphere from Gibilmanna is considered representative of the ionospheric layering above the eruption. The geomagnetic indices in the eruption day maintain low values over 24 hours with -13 $\leq$ Dst $\leq$ -4 and Kp $\approx$ 2. On the base of geomagnetic indices, the upper atmosphere is quite calm during the eruption in such a way that we may expect the detection of ionospheric forcing from the lithosphere (Fig. 4.8) [40].
Once defined the GNSS dataset, raw TEC estimations are firstly recovered as slant component. For TEC mapping it is appropriate to analyze the vertical component of TEC

$$vTEC = sTEC\cos(\eta) \tag{4.1}$$

where η is the mapping factor of eq.(3.17).

Five GPS satellites are found to transit near Etna during the December 4^{th} 2015 morning eruption (Fig. 3.7). To minimize artifacts and temporal misalignments, the TEC analysis starts from the integral of the raw differential TEC by eq.(3.14). Only the records of two satellites, G08 and G32, show dvTEC oscillations after the seismo-acoustic onset of the eruption (Fig. 4.3a-b). Then, a 4^{th} order Butterworth band-pass filter in 0.5 - 10 mHz is applied to analyze the acoustic-gravity components in 2 - 30 minutes range and TEC oscillations are recognized with period $\tau_{G08} \sim 20$ - 25 min and $\tau_{G32} \sim 12$ - 15 min, amplitude A ≈ 0.6 TECU (hereafter, terms like signature, anomaly, fluctuation and oscillation are used as synonyms to describe the local co-volcanic variation of differential TEC).

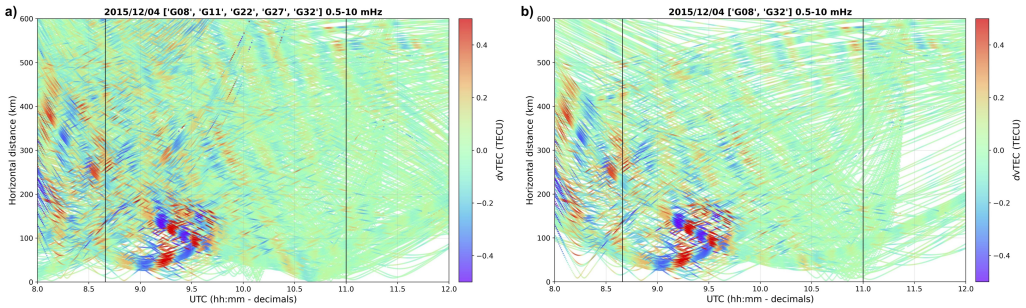

Figure 4.3: Travel-time diagrams of the S-R pairs observations during the eruption. Panel a) shows the observations for all satellites with a defined TEC anomaly around 09:00 - 09:30 UTC; b) same outputs of a) relative to satellites G08 and G32 only, as the two satellites detecting the TEC perturbation. The black solid lines indicate the seismo-acoustic onset and finish of the eruption.

To better analyze the two-dimensional characteristics of the ionospheric TEC signatures, a selection of around 20 GNSS stations, along transverse directions to the satellite's IPP trajectory on the TEC map, is done; this method allows better time-space tracking of the TEC signatures since it simplifies the identification of the waveform. Once defined the baselines of receivers for satellites G08 (NNE - SSW direction) and G32 (E - W direction), the TEC signatures are tracked on their own TEC maps. Figures 4.4a,b show the TEC maps for both satellites G08 and G32, on which the TEC anomaly is observed. The satellite G08 is in descending orbit from the northwest to the south, whereas satellite G32 is in ascending orbit from the southwest to the northeast. By this configuration, the satellite G08 goes

away from the source during the detection of these co-volcanic TEC signatures, while the satellite G32 approaches the source when its line-of-sights detect the perturbation. The TEC anomaly is located from both satellites around 100 - 200 km south-southwestward of Etna and it totally disappears beyond 200 km. Then, these co-volcanic ionospheric disturbances occur in the near-field of Etna volcano with a south-southwestward directivity.

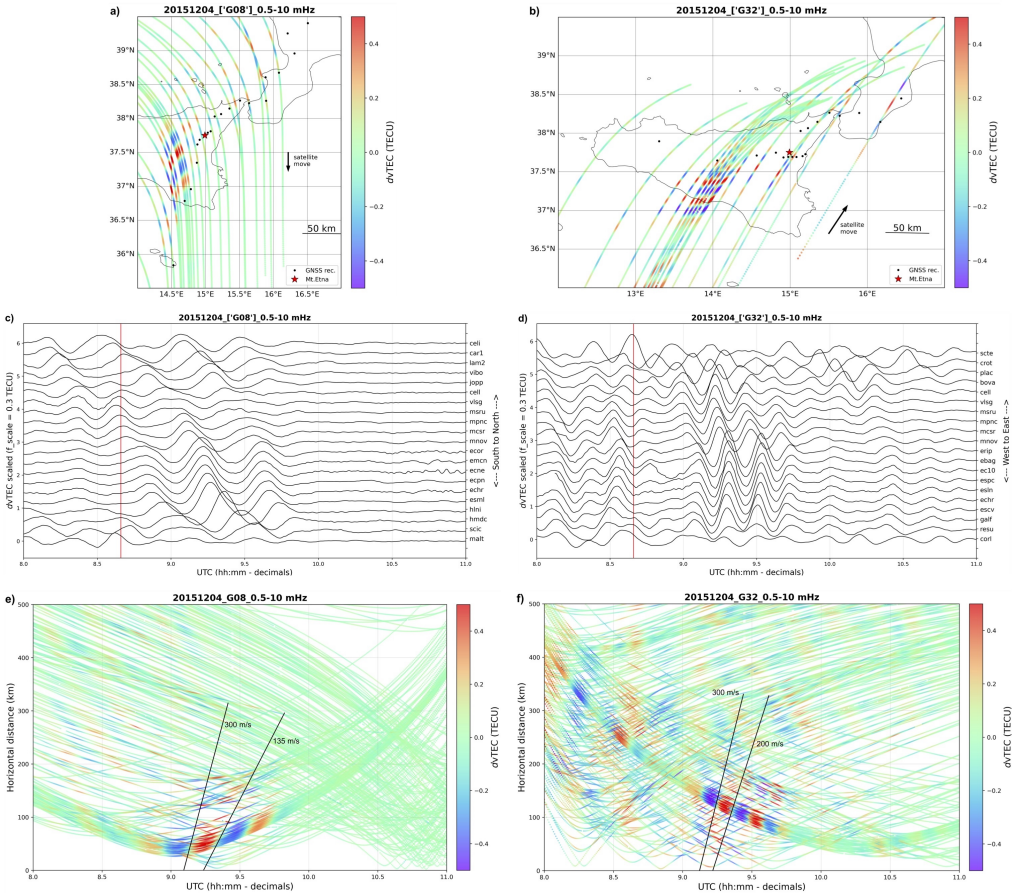

Figure 4.4: a) TEC map of satellite G08 along NNE - SSW line; c) TEC time series of the previous TEC map with the names of the receivers on the right axis (bottom to up = south to north-east); e) hodochrones of satellite G08 and the apparent velocities U_{HA}. Second column: b) TEC map of satellite G32 along E - W line; d) TEC time series of the previous TEC map (bottom to up = west to east); f) hodochrones of satellite G32 and the apparent velocities U_{HA}. The red line in the TEC time series indicate the seism-acoustic start of the eruption.

Figures 4.4c,d show the TEC time series from both satellites G08 and G32, respectively. The TEC signatures progressively emerge starting from 09:00 - 09:05 UTC, reach the peak amplitude around 09:15 - 09:20 UTC and then attenuate after 09:45 UTC. Therefore, these local TEC perturbations last for about 30 min with 2 - 3 quasi-periodic oscillations. The initial noise for G32-detection, between 08:00 - 08:40 UTC, is basically due to

the low elevation angle $\varepsilon_{G32} \sim 20°$ - $40°$ related to the satellite access in the line-of-sights of the ground GNSS network. Indeed, for satellite G08 the elevation angle $\varepsilon_{G08} \sim 55°$ - $70°$ in the same time, and the time series aren't affect by noise. Figures 4.4e,f show the hodochrones of both satellites, that is travel-time diagrams showing the TEC time series as a function of amplitude (color scale), time and sub-ionospheric pierce point's distance from the source (e.g. epicentral distance). The interpolation along the hodochrones of the in-phase points of the TEC signatures is an estimation of the horizontal apparent velocity $v_{HA} \sim 135$ - 300 m·s^{-1}.

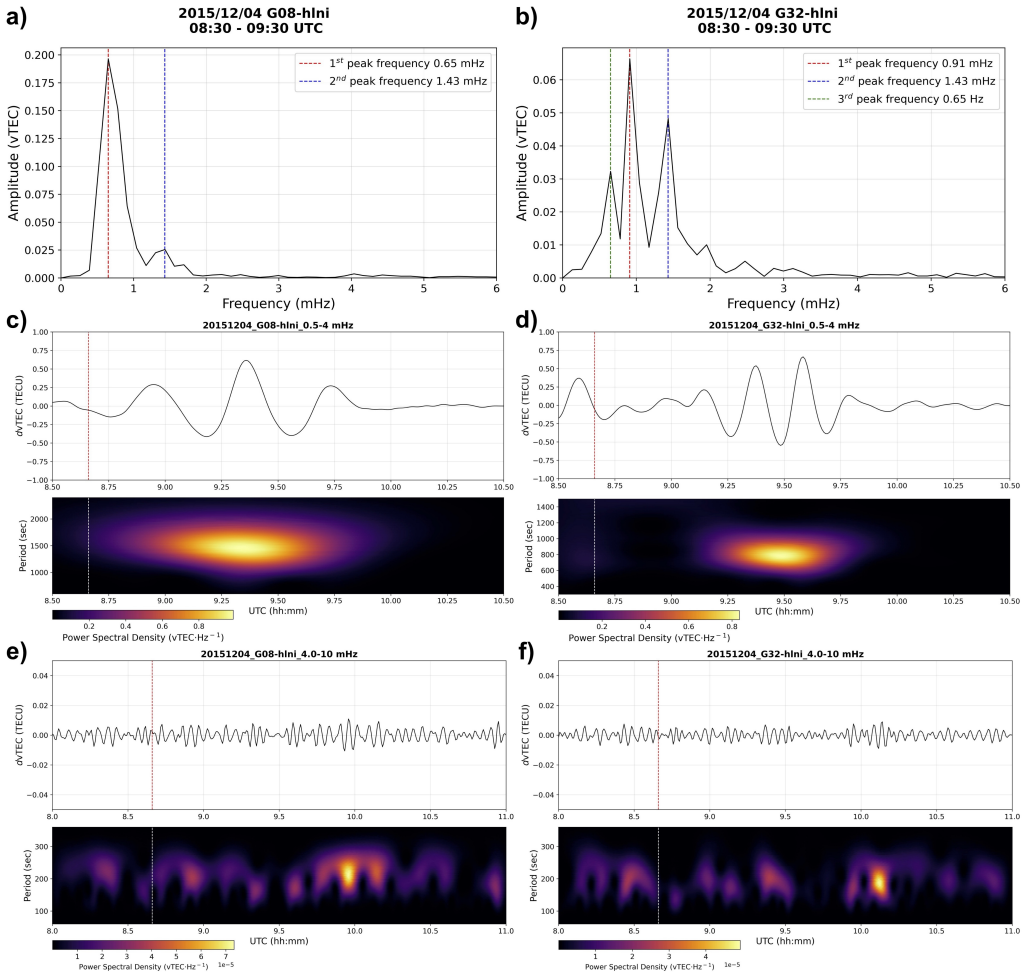

Figure 4.5: a), b) Fast Fourier Transform amplitude spectra with the peak frequencies reversed; c), d) Continuous Wavelet Transform power spectral density into the gravity frequency range (0.5 - 4 mHz); e), f) CWT power spectral density in the acoustic frequency range (4 - 10 mHz). The colored dashed lines in a), b) indicate the peak frequencies; the red and white dashed lines in c), d), e), f) indicate the seismo-acoustic onset of the eruption.

To analyze the spectral features of these co-volcanic ionospheric disturbances, the GNSS station HLNI (37.35 °N - 14.87 °E) is chosen, since it

records the maximum TEC amplitude around 0.6 TECU for both satellites G08 and G32. HLNI station is sited 45 km southward of Etna, that is quite far from hypothetical distortions of line-of-sights crossing the volcanic plume. The 1D - Fast Fourier Transform (FFT) for the pair G08 - HLNI returns a peak frequency $f_{G08} \approx 0.65$ mHz and one minor peak at 1.43 mHz that is one order of magnitude less (Fig. 4.5a). Knowing f_{G08} it is possible to set the Continuous Wavelet Transform (CWT) parameters for the 2D spectral analysis of the TEC signature. The CWT returns a power spectral density peak around 09:20 UTC, when the sub-ionospheric pierce point distance from the Etna is $r_h \sim 90$ km. The 4^{th} order Butterworth band-pass filter is applied to analyze the acoustic frequency range (4 - 10 mHz) but, despite a power spectral density peak around 10:00 UTC, the TEC amplitudes are at the background level and no distinct waveforms are observed (Fig. 4.5c-e). Slightly different spectral outputs are from the pair G32 - HLNI. In this case, the TEC signature's waveform oscillates with one more cycle than the one detected by satellite G08. The 1D - FFT analysis reveals a wider amplitude spectrum that is characterized by a peak frequency at 0.91 mHz and by two minor peaks at 1.43 mHz and 0.65 mHz. Finally, one order of magnitude less is the spectral amplitude in the range 2 - 3 mHz (Fig. 4.5b). Even for the pair G32 - HLNI it occurs a power spectral density peak in the acoustic frequency range, early after 10:00 UTC, but no distinct TEC signatures are recognized in the time axis upon the background level (Fig. 4.5d-f). Notably, an inversion of the primary and secondary peak frequencies is observed between satellites G08 and G32. Specifically, the amplitude spectrum of the pair G08 - HLNI exhibits a primary peak at 0.65 mHz and a secondary peak at 1.43 mHz, whereas that of the pair G32 - HLNI shows dominant peaks at 0.91 - 1.43 mHz and a secondary peak at 0.65 mHz.

To validate the spectral analysis of these TEC signatures, the Empirical Mode Decomposition (EMD) is applied on the time series from the same satellite - station pairs. Based on the empirical method, EMD provides information that is physically reliable. Since the so-called *sifting technique*, the EMD can be applied on the unfiltered input signal of eq.(3.13), to avoid filtering artifacts or time shifts, and without preventative detrend. In this way, the EMD is directly applied on the single-time difference of the TEC variation, by preserving the core data of the ionospheric detection. The EMD outputs, for the same satellite - station pairs, are similar to the FFT ones of Figure 4.5. In particular, the physical nature of these co-volcanic

ionospheric disturbances is validate to the fact that the EMD identifies the TEC signature as a single intrinsic mode for both satellites G08 and G32. Figure 4.6 shows the first three IMFs for both satellites. Lower frequency IMFs and the final residual are not displayed since they shift to planetary scale.

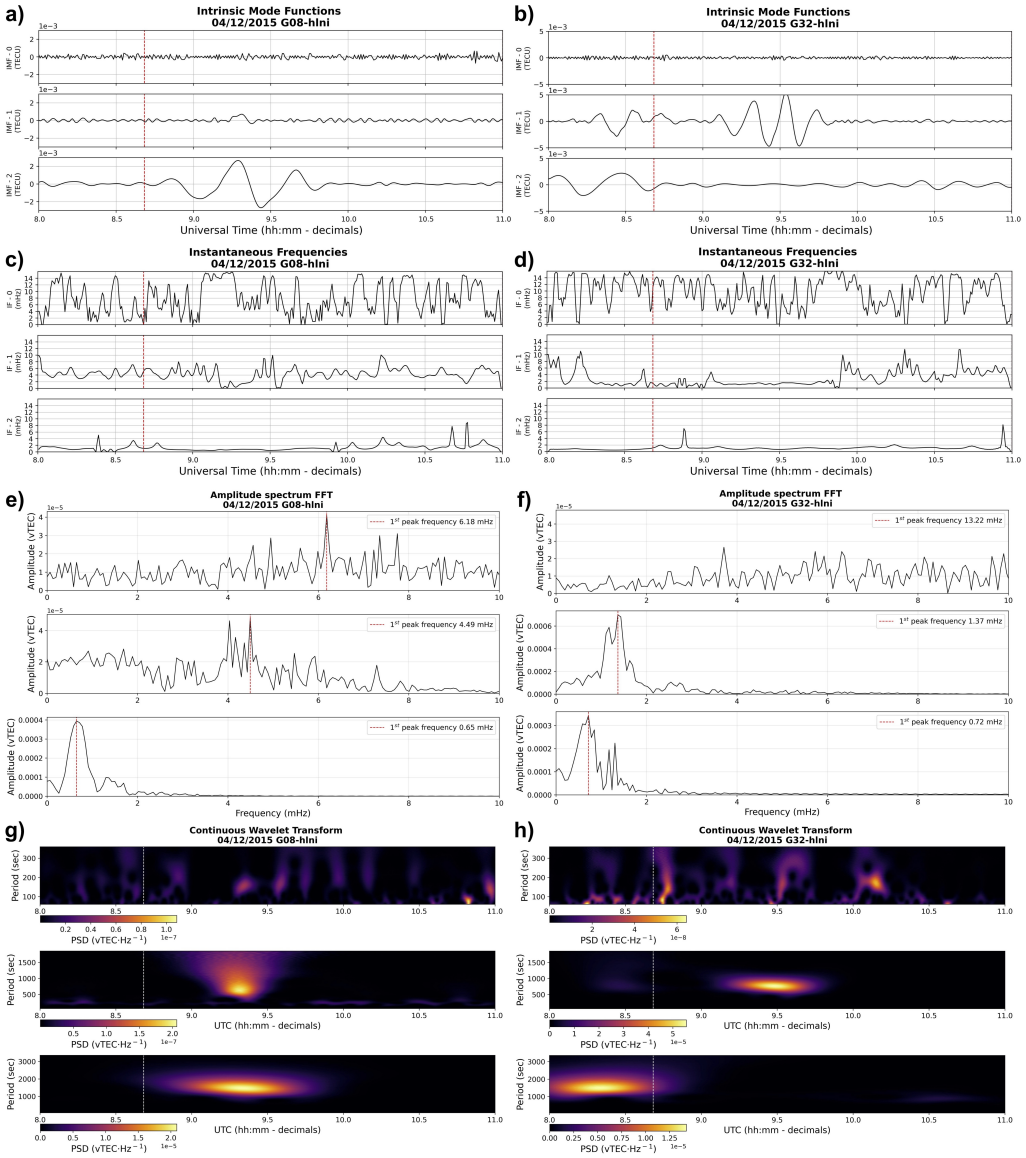

Figure 4.6: EMD integrated by FFT and CWT. Panels a, b) show the first three intrinsic mode functions for both satellite - station pairs; c, d) show the instantaneous frequencies of the previous IMFs; e, f) show the FFT amplitude spectra of the IMFs; g, h) show the CWT power spectral density of the IMFs. The red and white dashed lines in a, b, c, d, g, h) indicate the seismo-acoustic onset of the eruption; the red dashed lines in e, f) indicate the peak frequencies.

Regarding the pair G08 - HLNI, only the third mode IMF_2 is characterized by amplitudes comparable to the TEC observation. One IMF means a distinct waveform with finite spectral characteristics that are verified by

the instantaneous frequency IF_2 settling to values around 0.5 - 1 mHz and by the simultaneous appearance of the waveform in the time axis (Fig. 4.6a,c). This EMD output fits well with the FFT one, as verified by the re-processing of the FFT on the IMF_2 returning a peak frequency equal to f_{G08} (Fig. 4.6e, third row). New details are retrieved from the second mode IMF_1. Although its waveform is not defined, its amplitude is of the same order of magnitude than that of IMF_2. The re-processing of the CWT on the IMF_1 returns a power spectral density peak at periods around 500 - 700 s attenuating towards the same periods of IMF_2, like indicate a short-lived pulse coinciding to the peak TEC amplitude around 09:15 - 09:20 UTC (Fig. 4.6g). The period range 500 - 700 s of IMF_1 retrieved from CWT fits with the instantaneous frequency IF_1. Regarding the pair G32 - HLNI, the EMD identifies the second mode IMF_1 as representative of the TEC signature. In this case, the amplitude of IMF_1 has a very similar value to that of the input signal and the re-processing of FFT and CWT returns spectral peaks to periods around 700 - 800 s, fitting well with the instantaneous frequency IF_1 (Fig. 4.6b,d,f,h). The integration of FFT, CWT and EMD highlights the potential of integrate different spectral analysis techniques. In particular, two notes are explained as follows. First) it can be noted that the FFT amplitude spectra report the dominant peak frequency of the entire time series. This means that the 1D-FFT peak frequency may not necessarily correlate with the single waveform of interest within the time series itself. For example, the FFT amplitude spectrum in Figure 4.6e for IMF_1 (middle row) reports a peak frequency of 4.49 mHz, which is not the frequency of the IMF. In fact, the instantaneous frequency IF_1 is approximately 1 - 2 mHz, which is instead identified by the CWT (Fig. 4.6g, second row). Second) the EMD identifies the peak frequency of the TEC perturbation detected by the pair G32 - HLNI. Indeed, the FFT in Figure 4.5b reports three peak frequencies for the pair G32 - HLNI. Since the relatively noisy G32-detection, as described in Figure 4.4d, these three peak frequencies include noise also. The EMD splits these frequencies to associate their respective IMF and then it is possible to note in Figure 4.6f that the peak frequency of the TEC signature, detected by the pair G32 - HLNI, is $f_{G32} \approx$ 1.4 mHz. Finally, it is important to note that the index $j = 0$ doesn't refer to the fundamental mode of the TEC disturbance but it simply indicates the highest frequency component extracted by sifting. Once performed the spectral analysis of these co-volcanic ionospheric disturbances, it arises that the satellite G08 detects TEC amplitude peak around 09:15 - 09:20 UTC

with period of 1540 s ($f_{G08} \approx 0.65$ mHz) while the satellite G32 detects the same peak around 09:30 UTC with period of 730 s ($f_{G32} \approx 1.4$ mHz).
To get information about the TEC perturbation onset time in the ionosphere, the EMD is performed on the TEC time series of Figures 4.4c,d. As shown in Figures 4.4e,f, the local TEC anomalies appear to begin around 09:00 UTC but it is not possible to unambiguously identify the specific GNSS station where the ionospheric disturbance first emerges. Figures 4.4c,d reveal that the TEC amplitude observed by satellite G08 begins to rise in the records of MSRU, MPNC and MCSR stations, which are located in the northeastern part of Sicily island (Italy) along a baseline of 40 km (Fig.4.7a).

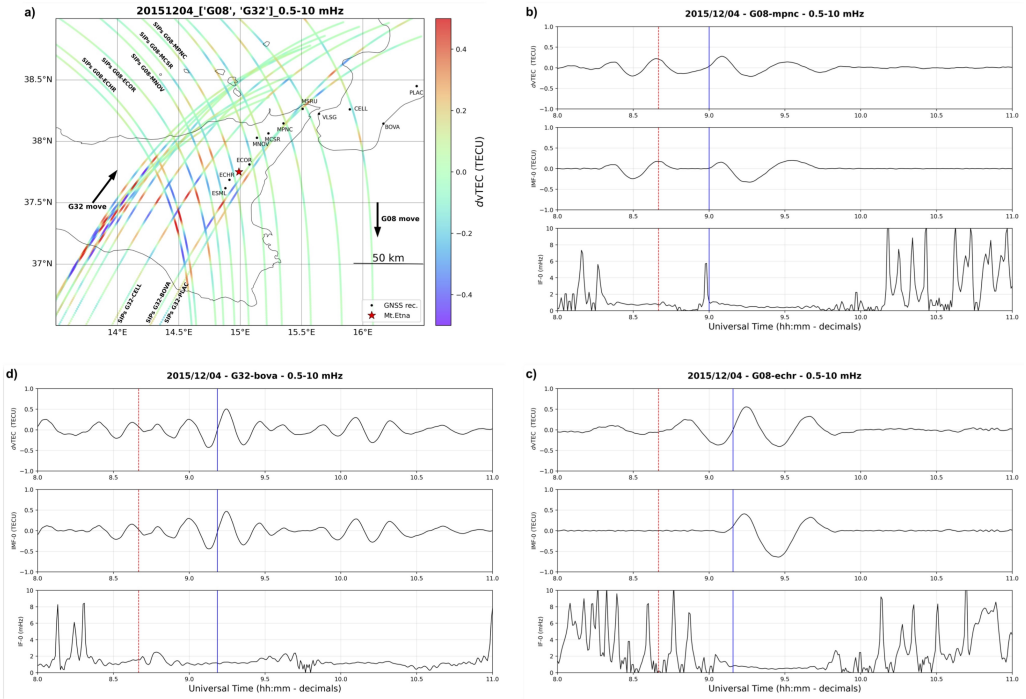

Figure 4.7: a) detailed TEC map showing the GNSS stations involved in the picking of the TEC anomaly onset time t_0 in the ionosphere. It can be noted the south-southwest directivity of the TEC perturbation; b, d) EMD outputs with stable mode-frequency components. The red dashed line indicates the seismo-acoustic onset of the eruption; the blue line in G08 - MPNC pair indicates t_0 while the blue lines in G08 - ECHR and G32 - BOVA time series indicate the picking time of the ongoing TEC positive peak started from t_0.

In contrast to the other stations, the EMD analysis of the pair G08 - MPNC reveals a TEC anomaly characterized by a well-defined intrinsic mode and a nearly constant instantaneous frequency (Fig.4.7b). This mode-frequency combination becomes recognizable from the TEC background at approximately $t_0 =$ 09:00 UTC, which it can be the likely signature of ionospheric forcing from the eruption. Conversely, Figure 4.4d indicates that TEC per-

turbations recorded by satellite G32 start to appear in the records of BOVA and PLAC stations, located in the south of Calabria peninsula (Italy) along a 40 km baseline. These signals are, however, contaminated by persistent noise due to the low elevation angle of G32. Despite this, the EMD output for the pair G32 - BOVA exhibits a quasi-periodic TEC fluctuation, with a coherent intrinsic mode and instantaneous frequency peaking around 09:11 UTC (Fig.4.7d). Figure 4.7a also shows that the IPPs (SIPs in the TEC map) of G08 at t_0 are located within 50 km of Etna volcano. Notably, t_0 aligns with the sustained TEC amplification towards the southwest around 09:09 UTC, as observed in the G08 - ECHR pair (Fig. 4.7c).

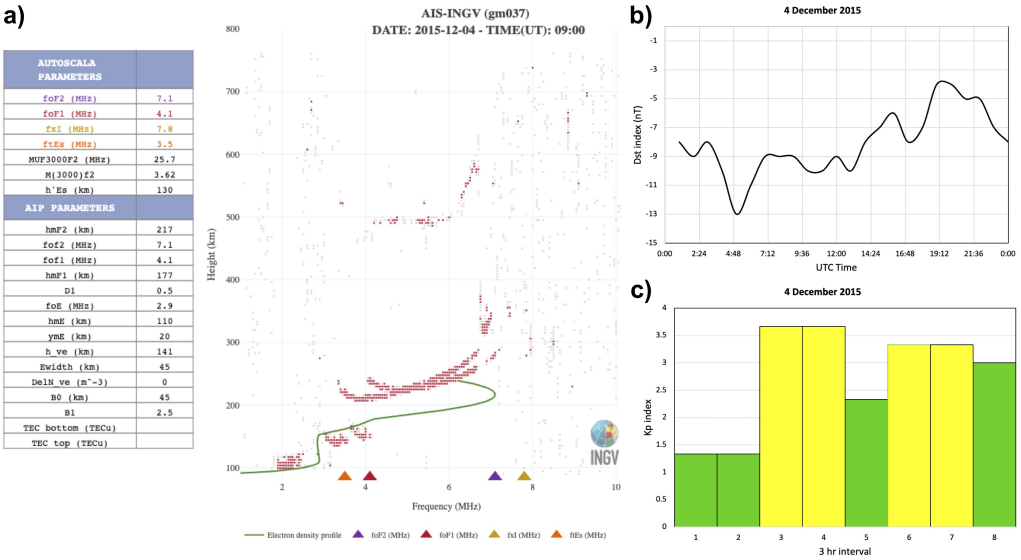

Figure 4.8: a) ionogram from Gibilmanna showing the electron density profile recovered from HF radio frequency reflectors altitudes. The colored triangles indicate the autoscaled peak frequency values used in the inversion model; b) Dst index time series around -10 nT during the December 4^{th} 2015; c) Kp index for the same period showing quiet geomagnetic conditions.

4.2.1 Doppler shift correction and the intrinsic wave characteristics

The local co-volcanic ionospheric disturbances detected by satellites G08 and G32 show a frequency difference $\Delta f = f_{G32} - f_{G08}$ leading to the relation $f_{G32} \approx 2f_{G08}$. This difference is caused by the Doppler shift due to the ionospheric pierce point motion and then the frequency variation must be corrected by the v_{ipp} to know the *intrinsic characteristics* of the TEC perturbation. The GNSS - TEC detection here presented is based on standalone receivers only, then our statement is the IPP as the moving observer

and the Etna volcano as the motionless source. Therefore

$$\omega_{obs} = \omega_0 + |v_{ipp}||k_x| \cos(\theta) \tag{4.2}$$

where $\omega_{obs} = 2\pi f_{obs}$ is the observed angular frequency, $\omega_0 = 2\pi f_0$ is the intrinsic unknown angular frequency, k_x is the horizontal wavenumber of volcano-induced acoustic-gravity waves (AGWs) and θ is the angle between $\vec{v_{ipp}}$ and $\vec{k_x}$ [38].

To find θ it is necessary to know the directions of the AGWs propagation and of v_{ipp}, that is δ_{AGW} and δ_{ipp}, respectively. The direction δ_{AGW} is related to the in-phase points direction δ_Φ of the TEC anomaly at the same time (Fig. 4.4a,b). This means that, for plane-wave assumption, the direction δ_Φ is the front of the AGWs propagation and then

$$\text{(i)} \quad \delta_{AGW} \perp \delta_\Phi$$

By eq.(4.2) and (3.18), the intrinsic characteristics of the local co-volcanic ionospheric disturbances are retrieved as follows. As verified on the TEC map, the front of the TEC perturbation at 09:21:30 UTC (time of peak amplitude in the record of HLNI station) has a direction $\delta_\Phi \sim$ N232°E (Fig. 4.9). Then, since condition (i), the AGWs propagation has an orientation $\delta_{AGW} \sim$ N142°E. The eq.(3.18) is applied for both satellites, G08 and G32, to know the distance d_{ipp} and the direction δ_{ipp} tracked by their IPPs in the time range of the TEC signature detection $\Delta t =$ 09:00 - 10:00 UTC (Fig. 4.4c,d); then $\delta_{ipp}^{G08} \sim$ N172°E and $\delta_{ipp}^{G32} \sim$ N26°E. Once retrieved the IPP directions for both satellites, the corresponding θ to the AGWs direction are $|\theta_{G08}| = |\delta_{AGW} - \delta_{ipp}^{G08}| = 30°$ and $|\theta_{G32}| = |\delta_{AGW} - \delta_{ipp}^{G32}| = 117°$.

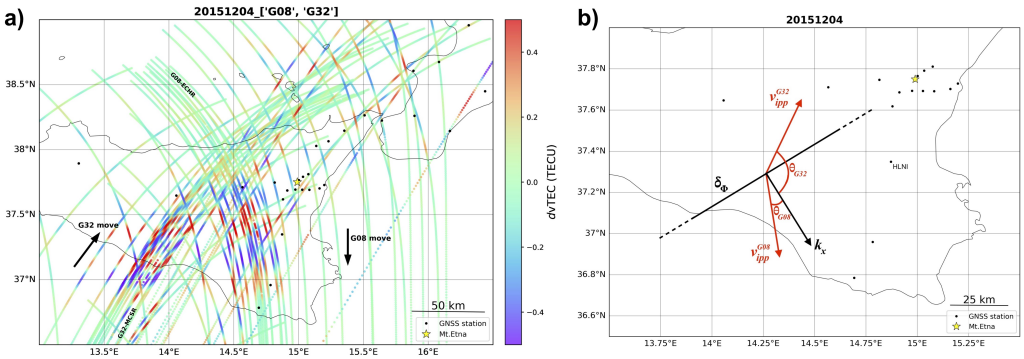

Figure 4.9: a) Near-field magnification of the TEC map showing the CVIDs detected by the two satellites G08 and G32; b) orientation of the IPP velocities and CVID vectors on the map. The black arrows in a) indicate the descending and ascending moving of G08 and G32 respectively.

The distance d_{ipp} between two epochs is related to the IPP velocity (Fig. 4.10). Figure 4.9a shows that the satellite G08 is in descending orbit, from northwest to south, and the satellite G32 is in ascending orbit from southwest to northeast. That is, the two satellites move in opposite directions during the occurrence of the TEC anomaly and then a Doppler shift can explain the difference of peak frequency characterizing their time series (Fig. 4.5 and 4.6). The IPP velocities are computed in the time range Δt as averages $v_{ipp}^{G08} \sim 26$ m·s^{-1} and $v_{ipp}^{G32} \sim 32$ m·s^{-1} (Fig. 4.10). Finally, knowing ω_{obs}, v_{ipp} and θ, the eq.(4.2) is applied for both satellites in a "system of two equations in two unknowns" to recover the intrinsic period $\tau_0 \sim 914$ s and the intrinsic horizontal wavelength $\lambda_x \sim 51$ km of the TEC anomaly, corrected by the Doppler shift. Then we obtain an intrinsic horizontal phase velocity $V_{HA} \sim 55$ m·s^{-1}. Since the electron density fluctuations are dynamically induced by neutral-ion collisions from acoustic-gravity wave propagation, V_{HA} is the horizontal apparent phase velocity. The value of V_{HA} is one order of magnitude less than the horizontal apparent velocity v_{HA} estimated from the hodochrones in Figure 4.4e,f. This discrepancy can be due to the fact that the CVIDs occur in the near-field for which the wave energy undergoes to a fast attenuation and/or dispersion, and then the wave field is really limited for a reliable estimation of v_{HA}. On the other hand, the value of V_{HA} is reliable since it is based on the observed peak frequencies f_{G08} and f_{G32}.

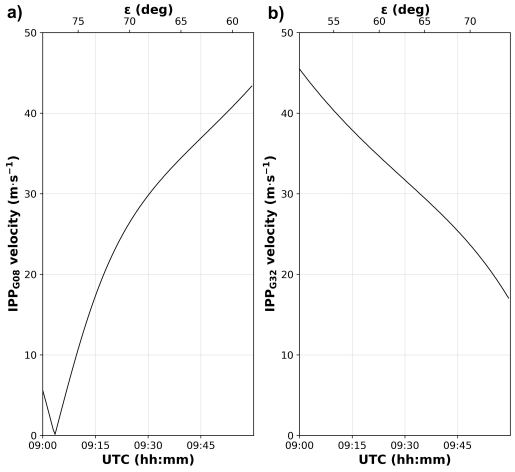

Figure 4.10: IPP velocities for the pairs G08 - HLNI and G32 - HLNI calculated in the time range 09:00 - 10:00 UTC with the elevation angle ε. It can be noted the inverse relation between v_{ipp} and ε.

4.2.2 Source characterization and infrasound ray tracing

To get further information about the time-space relations between the eruption and the TEC anomaly, a first step towards the modeling of the volcano - atmosphere coupling is here proposed as infrasound ray tracing by setting the large-scale lava fountain as the source. Figure 4.1 (panels in the middle) shows that the lava fountain reaches the maximum height $h_f \sim 2000$ m from the vent and then the fountain exit velocity $w_f \sim 200$ m·s^{-1} by eq.(2.2) is retrieved. The motion of the lava fountain and its height h_f are extremely variable during the eruption due to the fast rise of the gaseous slugs and their sudden separation from the liquid phase at the discontinuity faced to air. This means that the estimation of the fountain height depends on the method and 2000 m is a value based on the continuous fountain portion only. However, h_f is similar to the average height reported in literature [14]. Therefore, w_f represents the motion of our lithospheric source. The lava fountain stops at the top height h_f, where $w_f(h_f) = 0$, then the rising time of the lava fountain t_f is approximated as

$$t_f = \frac{w_f}{g} \tag{4.3}$$

where $g = 9.8$ m·s^{-1} is the gravity acceleration. The equation (4.3) represents the linear deceleration motion of the lava fountain against gravity and $t_f \sim 20$ s. However, the ray tracing technique needs a period of complete oscillation. Since t_f represents half the period then it is multiplied by 2 to have the source period $\tau_f \sim 40$ s. In detail, τ_f is consistent with the video analysis in thermal channel of the lava fountain since the visual counting of the slugs leads to estimate a flames frequency of the fountain $f_f \sim \frac{1}{\tau_f}$ during the main energy release time Δt (Fig. 4.2).

The ray tracing technique for infrasound takes into account the source oscillation period τ_f for a single fountain jet to return the characteristics of the infrasound waves as a function of height h and of zenithal angle χ. Figure 4.11 shows the results of ray tracing simulation for infrasound waves with the assumed period τ_f started with χ from 0° to 30° with the step of 1°, including the wave attenuation along the ray trajectories due to the kinetic viscosity and thermal conductivity. The background winds are not considered for simplicity [21]. It is clear that infrasound waves of τ_f are strongly attenuated at the heights around 200 km (Fig. 4.11b-d). The waves which

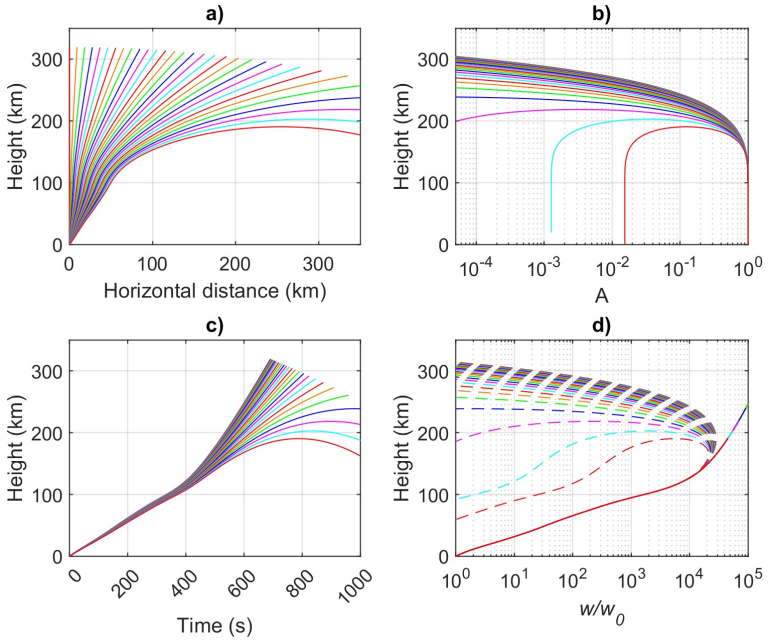

Figure 4.11: Ray tracing outputs as a function of height and for a source period $\tau_f \sim 40$ s. Panel a) shows the propagation distance; b) attenuation; c) travel time; d) amplification. It can be noted that the infrasound reaches the horizontal distances of TEC anomaly detection at about 200 km of altitude around 800 s.

are started with larger χ are attenuated more at the same altitude because they propagated longer time and larger distance at high altitudes. It should be noted that the real attenuation (decrease of energy density) is significantly larger than that displayed in Figure 4.11b due to the divergence of ray trajectories. Therefore, the infrasound ray tracing of the oscillation τ_f indicates that the travel time needed for the waves to reach the ionospheric shell height h_i, at the near-field horizontal distances observed in TEC map, is around 800 s and the same rays are those affected by most attenuation. These outputs provide travel times approaching to the observed onset time t_0 by starting from the formation of the eruption column, and not starting from the seismo-acoustic onset of the eruption. However, our co-volcanic ionospheric disturbances are mostly related to internal gravity oscillation modes (Fig. 4.6). Then, the infrasound ray tracing technique leads to say that further factors must be included in this volcano-ionosphere coupling case study.

4.2.3 Data integration

To rule out any accidental affecting of the volcanic plume to the satellite line-of-sights during the occurrence of the large-scale lava fountain, the ash

dispersion model HYSPLIT, proposed by the National Oceanic and Atmospheric Administration (NOAA), U.S.A., is adopted to track the ash dispersal area during the TEC anomaly detection, that is mostly in the time range 09:00 - 09:30 UTC. The HYSPLIT outputs are compared with the wind profile retrieved from the Climate Data Store of ERA5 reanalysis of European Centre for Medium-Range Weather Forecasts (ECMWF) (Climate Data Store). The wind components are retrieved from 37 standard pressure levels in the range 1000 - 1 hPa. Since the pressure exponentially decreases with altitude, the interdistance between two next pressure levels increases upward by reducing the accuracy of the high altitude values.

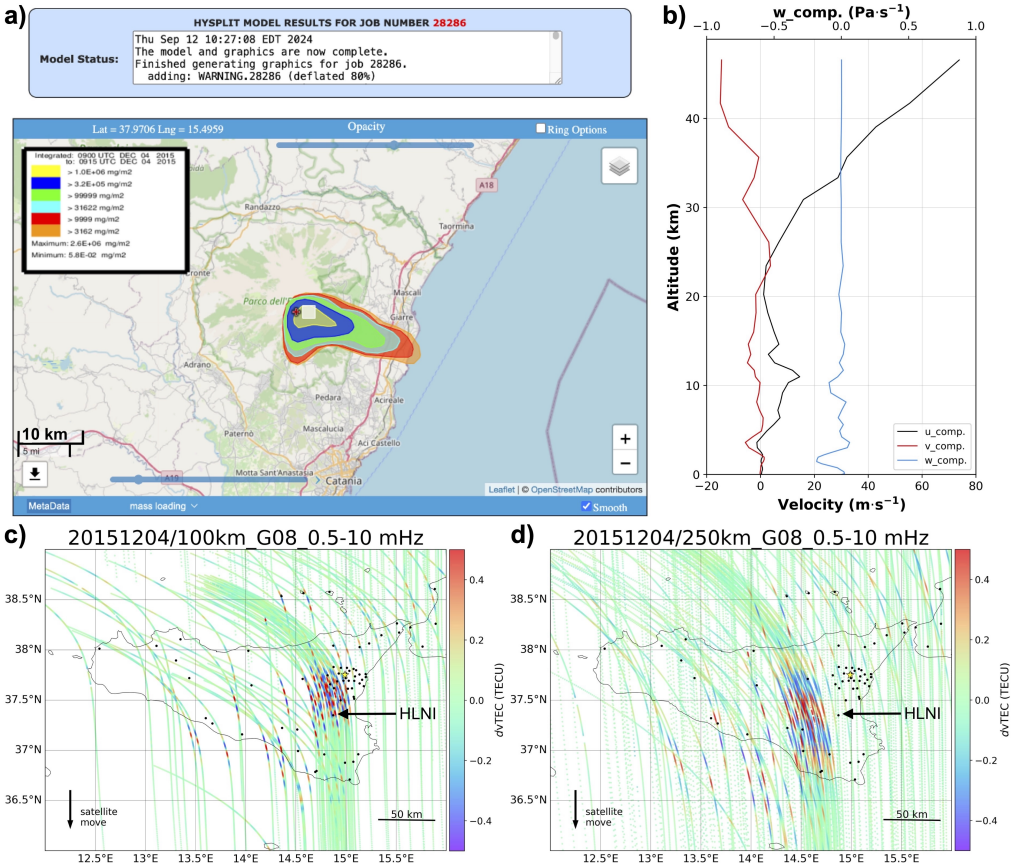

Figure 4.12: Comparison of the plume-wind data to the IPP trajectories: a) wind-oriented volcanic plume during the TEC detection. The colors indicate the ash concentration in mg·m^{-2} reducing from the central yellow area to the outer orange one. It can be noted that the plume develops eastward up to 20 km of the vent; b) profile of the wind components (u = west-east; v = north-south, w = vertical; positive values are for eastward, northward, downward motions respectively). It can be noted the westerly prevalent u-component fitting with the plume dispersion showed in a); c), d) IPP trajectories tracked for ionospheric shells at 100 and 250 km, respectively. It can be noted that the IPP trajectories shift south-westward with the altitude since the relative position of the satellite to the GNSS network.

Figure 4.12a shows the dispersion area of the volcanic plume during the

TEC anomaly detection. The orientation of the plume is mainly towards the east, fitting well with the prevalent westerly wind u-component at that time (Fig. 4.12b). The comparison between the plume-wind data and the IPP trajectories retrieved for different altitudes reveals that the satellites are linking with the GNSS network from the south-west, and then most of the line-of-sights related to the TEC signatures cross the free air.
Finally, the historic of the TEC time series, for the same time range 08:00 - 11:00 UTC, is reported in Figure 4.13 by the plot of dozens of time series related to the past or next days from the eruption. The days are plotted as Days Of Year (DOY) and the eruption day is the DOY 338. Despite the other days, when TEC oscillations are more incoherent, it can be noted on DOY 338 the distinct quasi-periodic TEC signatures. The comparison with the TEC time series recorded in other days indicates that TEC gravity oscillation modes can occur around the Etna volcano. Nevertheless, the TEC time series that are recorded during the December 4th 2015 morning eruption are those showing oscillations with the highest amplitude and with the most coherent structure.

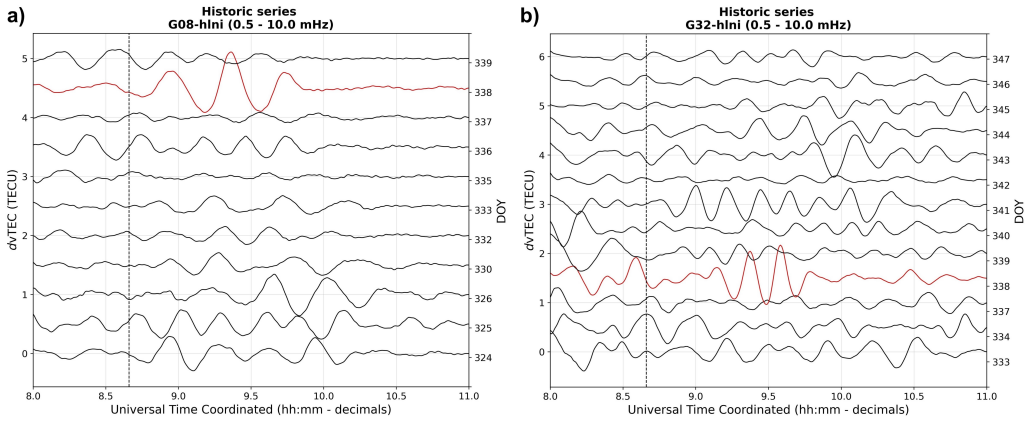

Figure 4.13: Historical TEC time series for the pairs G08 - HLNI and G32 - HLNI during the same time range of the December 4th 2015 morning eruption. a) historical TEC time series for the pair G08 - HLNI; b) historical TEC time series for the pair G32 - HLNI. The red TEC time series are those of the eruption day. The black vertical dashed lines indicate the seismo-acoustic onset of the eruption.

Although the onset time t_0 and the infrasound ray tracing lead to investigate further factors involved in the Etna-ionosphere coupling process, the historical time series outputs of Figure 4.13 show that the thermodynamic forcing of the atmosphere, induced by Etna volcano with prevalent internal gravity modes, can occur in such a way to perturb the local electron density distribution.

Chapter 5

The April 12th 2012 eruption

The April large-scale lava fountain occurred at the Nuovo Cratere di Sud-Est (NSEC) that was characterized by frequent explosive activity (section 2.1.2). The video records of April eruption show a well time definite lava fountaining activity lasting about 1 hr with an oblique eruption column due to the strong westerly wind. Despite the wind, the fire fountain reaches heights more than 1000 m above the vent and the volcanic plume reaches around 10 km of altitude. The eruption occurs in the time range 14:30 - 15:30 UTC and no clouds appear in the meanwhile. Figure 5.1 reports three screenshots of the April eruption in thermal and visible channels.

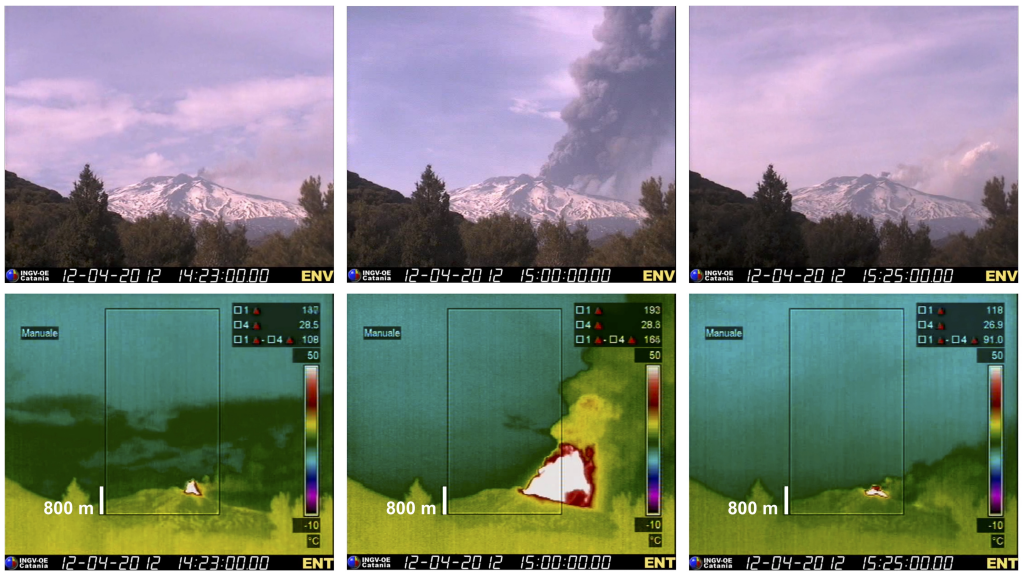

Figure 5.1: Screenshots of the April 12th 2012 eruption. The panels on the left show the lava fountaining activity onset, the panels in the middle show the paroxysmal timing related to the fountain at the maximum height and the panels on the right show the end of the eruption. The images are from the same videocamera reported in Figure (4.1). The white line indicates the height unit for the field of view.

The panels on the left show the eruption onset that is characterized by the incipient ash emission severely disturbed by the wind advection. Indeed, the ash dispersion is quite horizontal and directed on the east. A low fire fountain defines the thermal anomaly at the top. The panels in the middle show the oblique eruption column that is sustained by the lava fountain at its maximum height. A broad area of thermal anomaly around NSEC is recognizable. The panels on the right show the end of the eruption that is characterized by the remains at the ground of incandescent ejecta without any explosive activity. This eruption is among the more energetic lava fountains that occurred in the 2011 - 2012 paroxysmal sequence of Etna volcano [7].

5.1 The seismo-acoustic activity

The time range of seismo-acoustic activity fits well with the timing that can be estimated from video images. The seismo-acoustic time series shows a gradual intensification, since 13:00 UTC, until a steep increase of both vertical seismic velocity and infrasonic pressure amplitudes occurring as the eruption onset at 14:23 UTC (Fig. 5.2a).

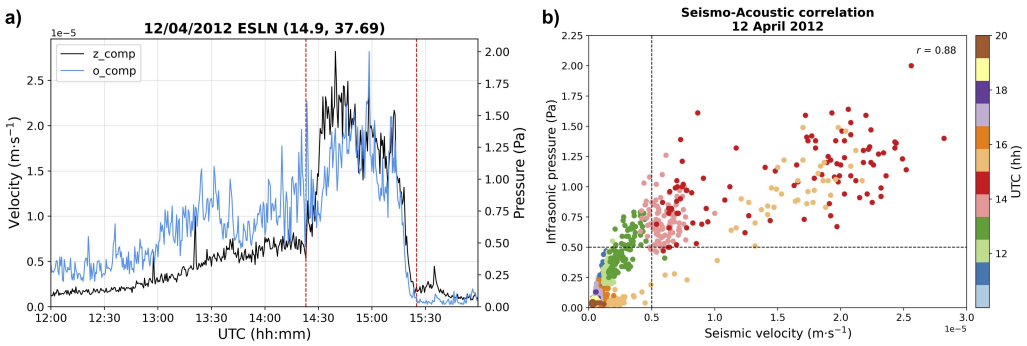

Figure 5.2: Seismo-acoustic data for the April 12th 2012 eruption; a) seismo-acoustic amplitudes time series where the abrupt change represents the onset of the lava fountaining activity; b) seismo-acoustic correlation with the field of the eruption and the Pearson coefficient r. The red dashed lines in a) indicate the seismo-acoustic onset and end of the eruption, respectively; the black dashed lines in b) define the seismo-acoustic field of the eruption as pink - red - sand colored dots.

Once the eruption started, the time series of seismic and infrasonic signals are characterized by the typical waxing-waning trend describing a quiet regular lava fountaining activity. The seismic amplitude reaches the peak around 14:35 UTC to gradually decrease until 15:15 UTC and finish with an abrupt fall at the pre-eruption values at 15:30 UTC; similar trend can be

appreciated from the infrasonic signal. As observed by video, the seismo-acoustic flat step between 14:30 - 15:15 UTC is the time range of high energy release in atmosphere, that is when the fire fountain is fully developed to sustain an highly convective eruption column. The seismo-acoustic field of the eruption is limited by infrasonic pressure threshold value of 0.5 Pa and vertical seismic velocity value of $0.5 \cdot 10^{-5}$ m·s^{-1}, that are related to peaks around 2 Pa and $3 \cdot 10^{-5}$ m·s^{-1}, respectively. The seismo-acoustic correlation reports a Pearson coefficient of 0.88 indicating the seismo-acoustic coupling between the volcanic conduit and the surrounding air above the vent (5.2b).

5.2 The ionospheric TEC analysis

The geomagnetic activity by Dst and Kp indices is quiet during the seismo-acoustic activity of the eruption (Fig. 5.2a,b,c). The Dst index varying around -10 nT and the Kp index variations are around 2 - 3. However, a geomagnetic depression begins at the Dst index around 17:00 UTC, to reach weak geomagnetic activity values of -40 nT in the evening that are accompanied by an increase of the Kp index to 4.5 after 18:00 UTC. This limited geomagnetic hustle is likely related to regional-global scale ionospheric forcing from above, induced by magnetosphere and/or space weather dynamics.

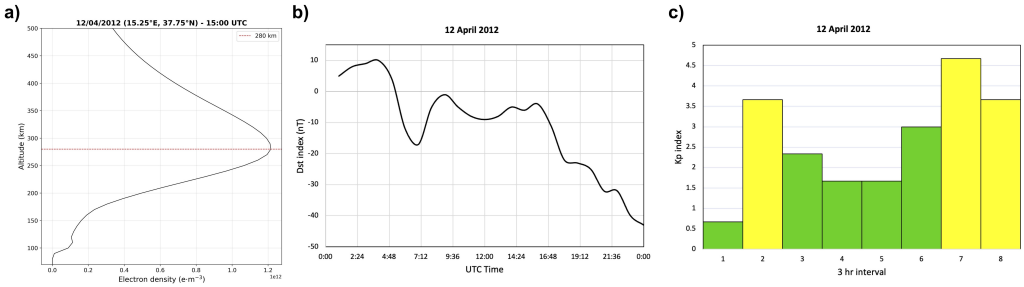

Figure 5.3: a) electron density profile of April 12th 2012 above the Etna at 15:00 UTC; b) Dst index characterized by the evening geomagnetic depression; c) Kp index with the green and yellow warning colors for quiet and moderate geomagnetic activity, respectively. It can be noted a quiet geomagnetic activity during the eruption.

Since the seismo-acoustic activity of the lava fountain ends at 15:25 UTC, the geomagnetic perturbation occurs more than two hour after the ideal entire duration of the ionospheric forcing from below and then, also in this case, co-volcanic ionospheric TEC perturbations may be expected. Regarding the vertical distribution of the electron density above the Etna volcano, no clear data come from the ionosonde in Gibilmanna Observatory and then the electron density profile is recovered from IRI model, version 2020. Since

the daytime occurrence of the eruption, the IRI model reports the electron density profile at 15:00 UTC, with an electron density peak altitude h_mF2 = 280 km.

During the April 12th 2012 eruption, near-field TEC perturbations are observed. The satellite skyplot, in the time range 12:00 - 20:00 UTC show four satellites transiting around the Etna volcano during the paroxysmal activity. The satellites are G09, G26, G27, G28 and the Butterworth 4th order band-pass filter is applied to their time series in the acoustic-gravity frequency range 0.4 - 10 mHz. Not all the satellites detect the TEC perturbations since the satellites G26 and G28 transit near Etna during the eruption but no clear TEC signatures are observed from their GNSS records (Fig. 5.4a).

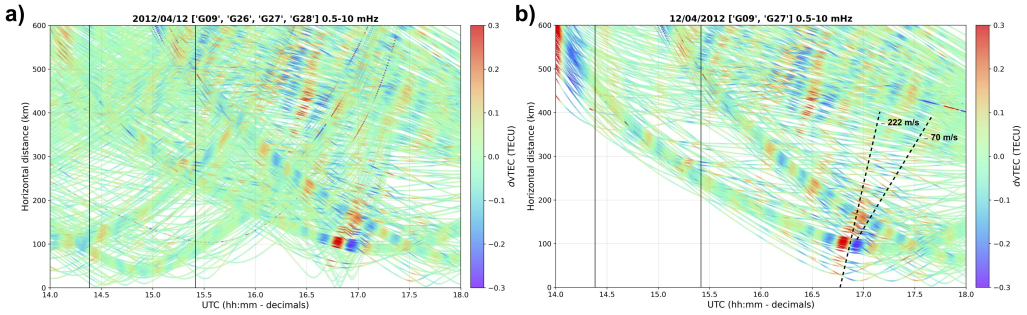

Figure 5.4: a) travel time diagram (hodochrones) of the four satellites transiting above Etna during and after the eruption; b) near-field TEC anomaly detected by the satellites G09 and G27 with the estimation of the horizontal apparent velocity v_{HA} and its dispersion to lower values. It can be noted that the two satellites near the source don't detect any TEC oscillations while the other two delayed satellites detect TEC perturbations. The black solid lines indicate the seismo-acoustic onset and end of the eruption, respectively.

On the other hand, the satellites G09 and G27 detect near-field TEC anomalies starting from 16:30 UTC, that is one hour after the seismo-acoustic end of the lava fountaining activity. The hodochrones of these two satellites are merged in Figure 5.4b showing defined local TEC anomalies up to 200 km of Etna and with an estimated horizontal apparent velocity $v_{HA} \sim 222$ m·s^{-1}. A dispersion of disappearing waves is recognizable from satellite G09 hodochrones, where low velocities $v_{HA} \sim 70$ m·s^{-1} are estimated from subtle TEC anomalies. Once identified the satellites of interest, a baseline of around 20 GNSS stations, from the southwest to the northeast, is defined to focus the TEC analysis on the time-spatial distribution of these local co-volcanic ionospheric disturbances.

Figures 5.5a,b show the TEC time series for both satellites G09 and G27 that are related to the GNSS ground baseline. The satellite G27 detects

high TEC positive peaks around 16:45 UTC with a northward propagation.

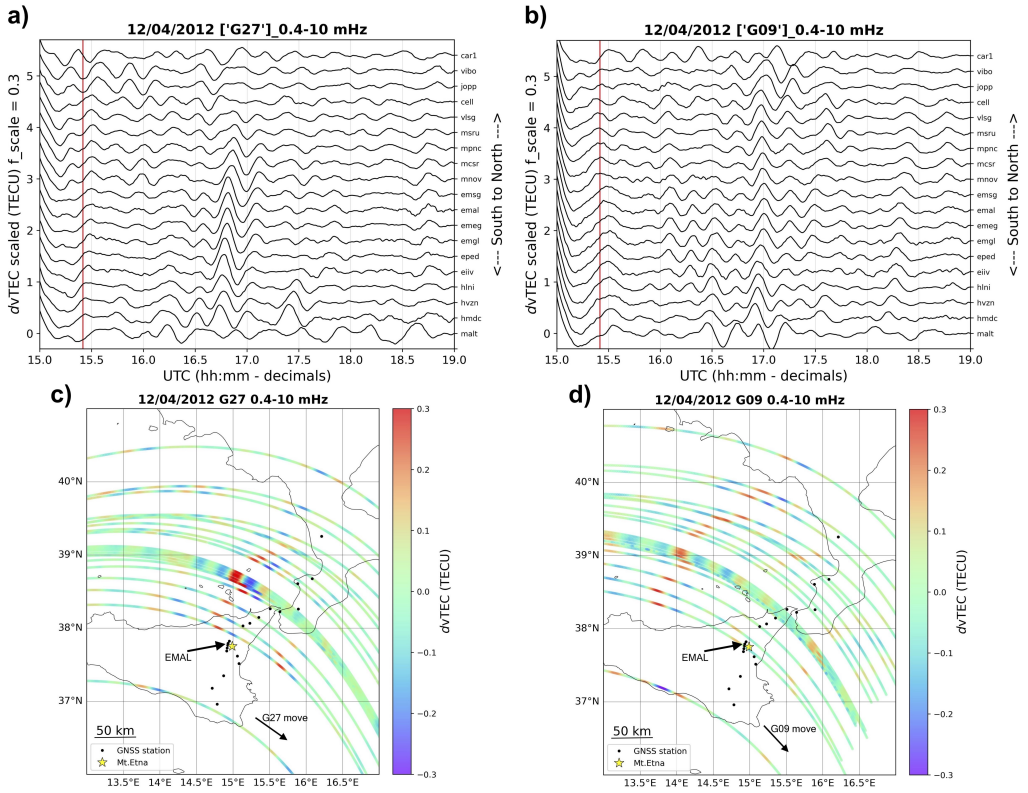

Figure 5.5: a - b) TEC time series of the satellite G09 and G27, respectively, in which the perturbation waveform and its propagation are recognizable; c - d) TEC maps of the previous time series along the southwest - northeast GNSS ground stations baseline. It can be noted the central core of the TEC perturbation expanding along the baseline. It can be noted also, observing from G27 to G09 TEC maps, the westward propagation of the TEC anomaly. The red solid line in a) and b) indicates the seismo-acoustic end of the eruption. The EMAL station site is indicated.

On the other hand, the satellite G09 detects subtle TEC oscillations around 17:00 UTC. Although the TEC amplitudes are lower than the G27 record, a focus on the G09 time series indicates a more deep northward propagation of the wave front around 17:00 UTC, that is anticipated by quasi-periodic oscillations at the southern records. However, we stay on the positive peaks of both satellites time series as the representative co-volcanic TEC perturbations for this case study. Figures 5.5c,d show the TEC maps of the previous time series for both satellites showing the geographical area of the TEC anomaly. Both satellites G09 and G27 are in descending orbits, from the west to the southeast, and then their ionospheric pierce points velocities v_{ipp} approach Etna volcano in similar directions. The TEC map of satellite G27 shows clearly the local co-volcanic ionospheric disturbances at the north of Etna volcano. These TEC perturbations are detected up to GNSS stations at 70 - 80 km of Etna, both at the south side and north side. On the other

hand, the TEC map of satellite G09 shows attenuated TEC amplitudes that are probably related to the last branches of the wave dispersion disappearing beyond 200 km (Fig. 5.4b). Satellite G27 detects the major TEC amplitudes around 0.3 TECU, according to the fact that its sub-ionospheric pierce points (SIPs) are closer to Etna than those of satellite G09 at the time of detection. The comparison of time series with TEC maps highlights that the satellite G09 detects the local TEC anomalies after the satellite G27 at about 60 - 70 km westward. This means that the delay of the G09 detection is reasonably around 17:00 UTC due to the westward propagation of this co-volcanic ionospheric disturbance (Fig. 5.5c,d). This means that both satellites G09 and G27 move in opposite directions to the TEC perturbation. The EMAL station of the local GNSS network is selected to analyze the spectral characteristics of these local co-volcanic ionospheric disturbances. The EMAL station is installed in the area of Maletto town, at 7 km westward to the lava fountain. The pairs G09 - EMAL and G27 - EMAL show the fully appearance of the TEC signature and their SIPs are at the center of the TEC perturbation (Fig. 5.5c-d). Also in this case, the signal degradation due to the hypothetical plume crossing by the line-of-sights must be ruled out since the following two reasons: i) the strong westerly wind directs the plume eastward by leaving free-air at the west; ii) the TEC anomaly detection from the most distant GNSS stations proves that the TEC anomaly cannot be related to a volcanic plume crossing of the satellite line-of-sights. The integration of Fast Fourier Transform (FFT), Empirical Mode Decomposition (EMD) and Continuous Wavelet Transform (CWT) spectral analysis techniques is applied to these two pairs and the results are showed in Figure 5.6.

Figures 5.6a,b show the unfiltered differential TEC signature of the April 12^{th} 2012 eruption. The signature from the pair G27 - EMAL occurs with a well defined impulsive onset and one complete oscillation cycle. On the other hand, the G09 - EMAL time series is affected by quasi-periodic oscillations before the positive peak observed along the GNSS baseline around 17:00 UTC (Fig. 5.5b). Figures 5.6c,d show the first three intrinsic modes of the TEC signatures in which unambiguous results come from the pair G27 - EMAL. Indeed, the EMD identifies the TEC signature as one intrinsic mode IMF_2, with amplitudes that are comparable to those of the filtered waveforms (Fig. 5.5a). Then the TEC signature has a physical nature maintaining the intrinsic characteristics after the decomposition, by describing a coherent structure.

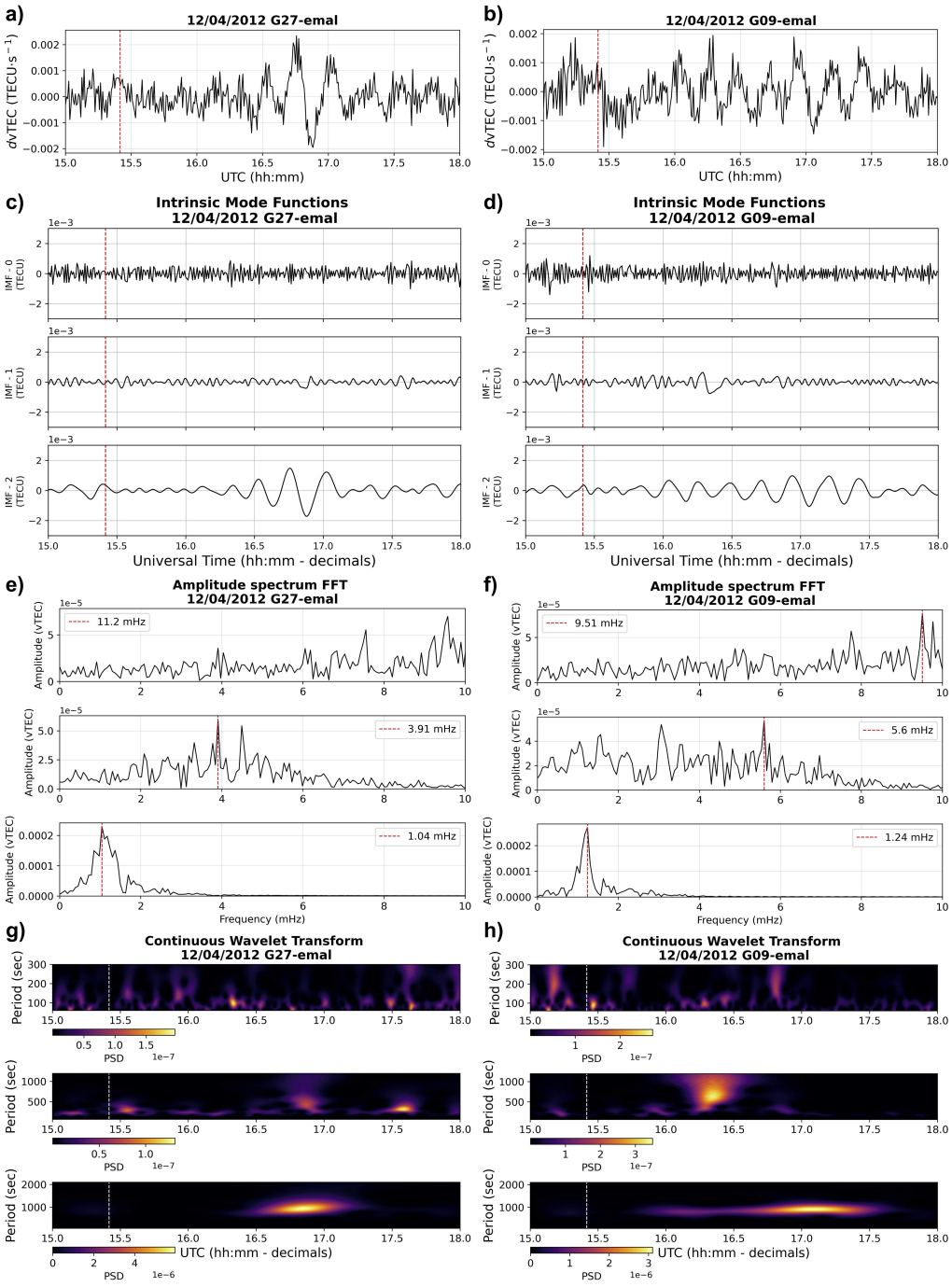

Figure 5.6: a, b) unfiltered differential TEC time series of the pair G27 - EMAL and G9 - EMAL, respectively; c, d) first three intrinsic mode functions of the previous signals; e, f) amplitude FFT spectra of the previous modes; g, h) power spectral densities of the continuous wavelet transform of the previous modes. The red dashed lines in a, b, c, d) and the white dashed lines in g, h) indicate the seismo-acoustic end of the eruption. The red dashed lines in e, f) indicate the peak frequency.

Less clear are the intrinsic modes from the pair G09 - EMAL. Ruled out the first two modes, where distinct oscillations from the noise are episodic, the third mode IMF_2 is affected by the same frequency components of the group observed in the time domain (Fig. 5.6b). However, the instantaneous frequency of this periodic IMF_2 must be very similar to the frequency of the filtered TEC perturbation showed in Figure 5.5b, because oscillations of IMF_2 occur also around 17:00 UTC. Figures 5.6e,f show the FFT of the previous intrinsic mode functions in which the peak frequency $f_{G27} \sim 1.04$ mHz ($\sim$ 960 s) is detected for the pair G27 - EMAL. Regarding the FFT of the pair G09 - EMAL, based on the previous considerations on its intrinsic modes, the peak frequency $f_{G09} \sim 1.24$ mHz ($\sim$ 806 s) may be considered realistic. Finally, Figures 5.6g,h show the power spectral densities of these local co-volcanic TEC perturbations that are recovered by the continuous wavelet transform of the intrinsic modes. It can be noted that the pair G27 - EMAL detects first a power distribution at periods around 1000 s between 16:45 - 17:00 UTC. From the pair G09 - EMAL it is evident the elongation of the power spectral density distribution due to the presence of the same frequency components. Getting a focus on this spectrum, it can be noted higher density values around 17:00 UTC, that is the time of detection for the attenuating wave front (Fig. 5.5b).

Due to the high positive peak of the TEC perturbation, it is easier for this eruption, than the December case study, to recognize the GNSS station recording the onset of the co-volcanic electron density fluctuations. Indeed, it can be observed (Fig. 5.5a) that the TEC perturbation peak begins to rise in the record of the pair G27 - HMDC. To have the picking time of the perturbation onset, the EMD is applied to the time series related to HMDC, HLNI and EIIV stations. The analysis of the intrinsic modes reveals that the peak begins to be stable starting from the line-of-sight of the pair G27 - EIIV. Indeed, the high frequency mode IMF_1, that can be observed in HMDC and HLNI records around 16:30 UTC, should be interpreted as episodic incoherent components since they are lost into the last decomposition of the EIIV record. At the same time, the IMF_2 maintains itself between 16:30 - 17:00 UTC, from HMDC to EIIV records, and then this mode must be a coherent structure.

Based on the EMD analysis, the TEC signature onset for the April 12^{th} 2012 is detected by the pair G27 - EIIV at 16:39:18 UTC, surprisingly more than two hours (2h 14 min) after the seismo-acoustic onset of the eruption (Fig. 5.2).

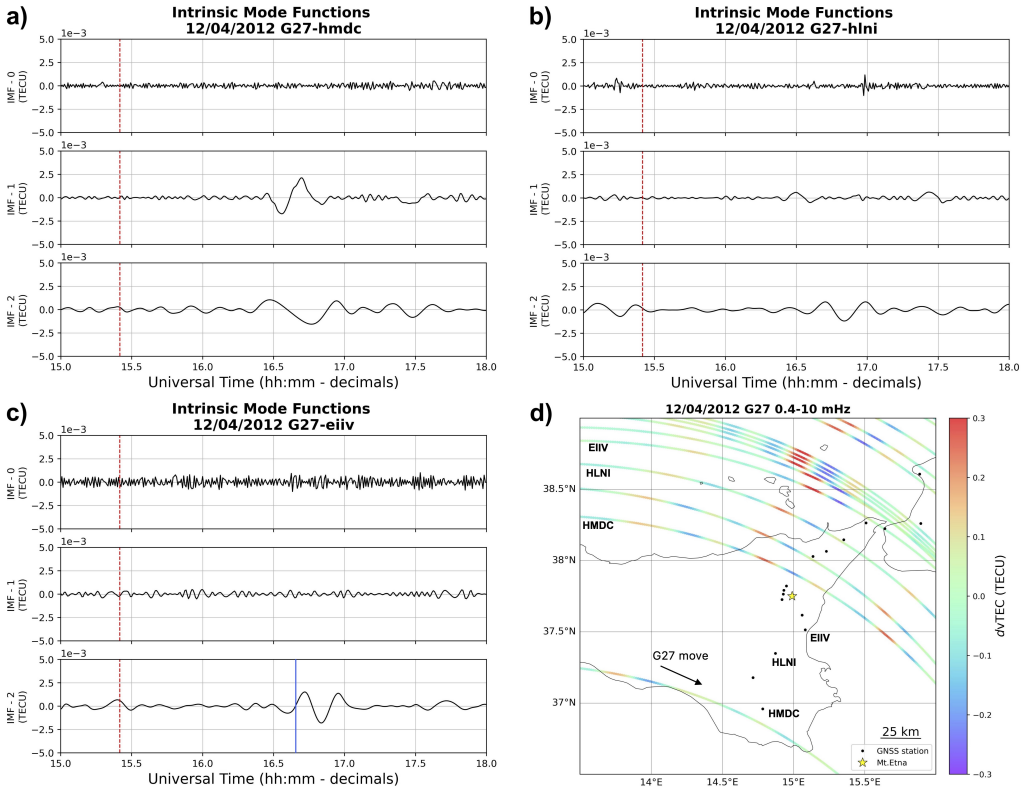

Figure 5.7: a) first three IMFs for the southern pair G27 - HMDC showing an episodic IMF_1 and the forming IMF_2; b) first three IMFs for the pair G27 - HLNI showing the IMF_1 disappearing and a more defined IMF_2 with low amplitude; c) first three IMFs for the pair G277 - HMDC showing a well defined IMF_2 that is related to the typical TEC signature; d) zoom-in of the TEC map around Etna volcano showing the geographical location of the IPP trajectory related to the previous satellite - station pairs. It can be noted the northward TEC amplification fitting with the previous IMFs time develop.

Once defined the periods $\tau_{G27} \sim 960$ s and $\tau_{G09} \sim 806$ s, the intrinsic wave parameters are recovered by inserting the VARION tabular outputs into the procedure from eq.(4.2) to eq.(3.18), as the same for the December case study. The direction of the acoustic-gravity wave $\delta_{AGW} \sim$ N92.5°E is similar to that of the IPP velocities $\delta_{ipp} \sim$ N110°E, which have values $v_{ipp}^{G09} \sim 44$ m·s^{-1} and $v_{ipp}^{G27} \sim 17$ m·s^{-1}. Both satellites G09 and G27 approach Etna and move in opposite direction to the TEC perturbation during its detection. Then eq.(4.2) returns an intrinsic period $\tau_0 \sim 1088$ s and an intrinsic horizontal wavelength $\lambda_x \sim 131$ km that are related to a horizontal apparent phase velocity $V_{HA} \sim 121$ m·s^{-1} at the electron density peak altitude $h_mF2 \sim 280$ km.

Chapter 6

The July 4^{th} 2024 eruption

This large-scale lava fountain belongs to the sequence of six paroxysmal episodes that occurred at the Etna in 2024, from July 4^{th} to August 15^{th}. It is the first of the six eruptions that, as the December case study, developed through the Voragine crater (VOR) [15]. No images for the July eruption are here reported since the cloud coverage seriously affects the usage of video images to estimate the time markers of the lava fountaining activity. However, the seismo-acoustic amplitudes time series are well related to the eruptive activity and then the estimation of the eruption timing, from only this ground-based dual-parameter record, may be considered quite reliable.

6.1 The seismo-acoustic activity

The seismo-acoustic activity of July 4^{th} 2024 eruption is characterized by a well defined steady-state and the longest lasting than the other two eruptions. Figure 6.1a shows the seismo-acoustic record of ESLN station reporting the entire duration of the paroxysmal activity lasting for about 9 hours. The seismo-acoustic onset of the July eruption is then estimated at 15:30 UTC and its end at 01:00 UTC of the day after. Due to the long lasting, the seismo-acoustic activity is characterized by a quite flattened waxing-waning trend indicating the long lasting steady-state of the lava fountaining activity, that is the fountain is sustained by a constant magmatic feeding from the depths of the volcano. The seismo-acoustic field of the eruption is defined by threshold values of 0.75 Pa and $1.75 \cdot 10^{-5}$ $m \cdot s^{-1}$, that are related to an infrasonic peak value around 3.5 Pa and to a vertical seismic velocity value around $6 \cdot 10^{-5}$ $m \cdot s^{-1}$. The seismo-acoustic amplitudes are similar to that of April and then, also for the July eruption, the infrasonic pressure

peak is less than one order of magnitude than the December case study. The Pearson coefficient of the seismo-acoustic correlation is calculated in the 20 hr time interval 10:00 - 06:00 UTC and it is equal to 0.85, indicating for this case study a slightly lower seismo-acoustic coupling than the previous two eruptions. This means that the simultaneous occurrence of seismic and infrasonic amplitudes signals is due to the same source, and then our estimations on the eruption timing may be reliably only based on the seismo-acoustic amplitude time series for this case study.

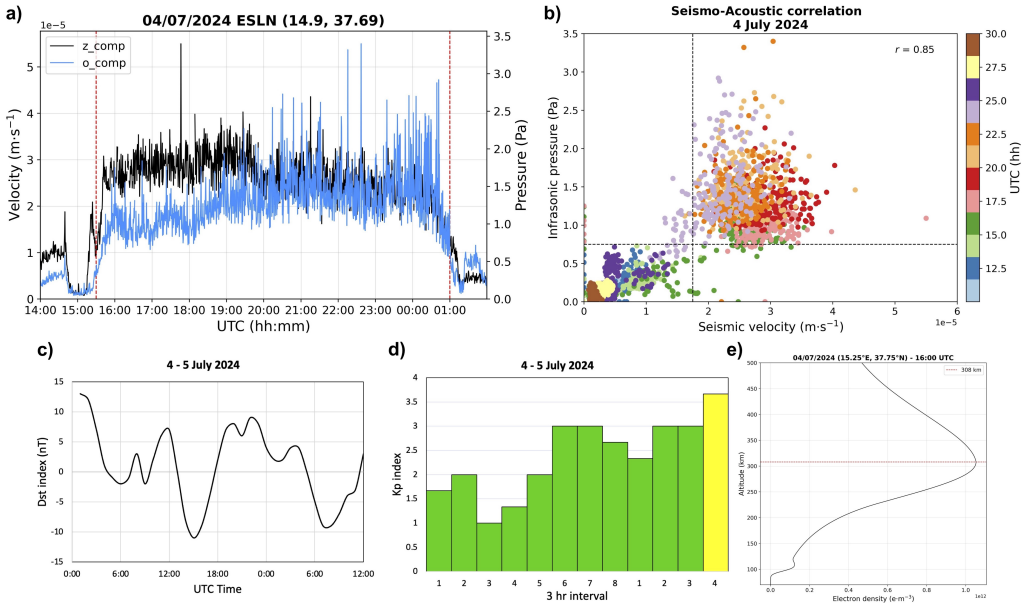

Figure 6.1: a) the long lasting seismo-acoustic activity of July 4th 2024 eruption. The o-comp is the infrasonic component whereas the z-comp is the vertical seismic velocity component. It can be noted the semi-parallel trend of the seismic and infrasonic amplitudes indicating the steady-state of the paroxysmal activity; b) seismo-acoustic correlation of the previous time series in which the Pearson coefficient $r = 0.85$ is related to the green-to-light purple dots cluster at the time of the seismo-acoustic peak amplitudes; c) 36 hr time series of the Dst index, from 00:00 UTC of July 4th to 12:00 UTC of July 5th, indicating quiet geomagnetic activity; d) 36 hr time series of the Kp index indicating high latitudes geomagnetic quiet activity; e) electron density profile with the typical Chapman layering related to the electron density peak. The red dashed lines in a) indicate the seismo-acoustic onset and end of the eruption. The black dashed lines in b) indicate the threshold values of the seismo-acoustic field of the eruption. The red dashed line in e) indicates the electron density peak altitude.

Regarding the geomagnetic activity, the July 4th 2024 is a quiet day from low to high latitudes. The Dst index varies between 15 and -15 nT in a 36 hr time range and it is around 5 nT during the most of the eruption. In the same 36 hr time range, the Kp index maintains low values under 3 during the eruption. The geomagnetic activity of July case study is the lowest among the three case studies here reported. Also for this eruption, the ionogram from the near Gibilmanna Observatory is not available and

then the electron density profile is recovered above the Etna volcano from IRI model at 16:00 UTC, that is characterized by an electron density peak at the altitude $h_mF2 = 308$ km.

6.2 The ionospheric TEC analysis

Five GPS satellites transit near the Etna volcano during the eruptive activity and their TEC time series are filtered in the acoustic-gravity frequency range 0.4 - 10 mHz by a 4^{th} order Butterworth band-pass filter. Once obtained the filtered time series related to all the GNSS stations of the network, it can be observed in Figure 6.2a,b that only the satellites G04 and G09 detect near-field TEC anomalies within 300 km of Etna. These local co-volcanic ionospheric disturbances are characterized by peak amplitudes around 0.4 TECU and estimated apparent velocity $v_{HA} \sim 185$ m·s^{-1}, that is a value similar to the previous December and April case study.

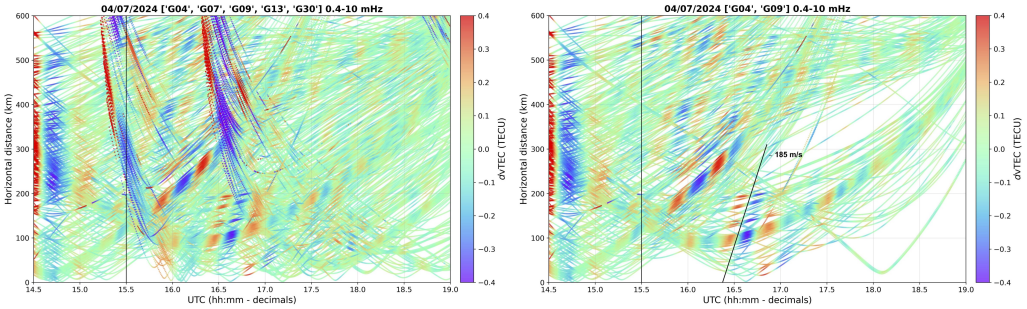

Figure 6.2: a) hodochrones of the satellites transiting around Etna before and after the seismo-acoustic onset of the eruption; b) hodochrones of the satellites G04 and G09 detecting the local TEC anomalies. The vertical black solid line in a), b) indicate the seismo-acoustic onset of the eruption. The slant black line in b) indicates the estimated horizontal apparent velocity v_{HA}.

Also in this case a GNSS stations ground-baseline, composed of 17 receivers, from southwest to northeast is defined to track the local TEC perturbation in the time domain. Figures 6.3a,b show the amplitude-scaled TEC time series along the baseline for both satellites G04 and G09. Despite to the previous April case study, the main amplitude TEC variation is characterized by a negative sign and then the timing estimation from the eruption is based on the negative TEC peak. The satellite G04 detects the TEC anomaly first, starting from 16:00 UTC, with a one complete cycle detected northward progressively. The local TEC amplitude begins to rise at the southern records, peaks at the middle ones and disappears at the northern records. The period of the TEC oscillation is around 25 min falling in the

internal gravity frequency range. Very similar is the TEC perturbation observed in the time series of satellite G09, starting from around 16:30 UTC, northward of Etna. In this case, the wave front is observed almost simultaneously along the GNSS baseline, showing again the fluctuation of the negative amplitude TEC peak from the south to the north.

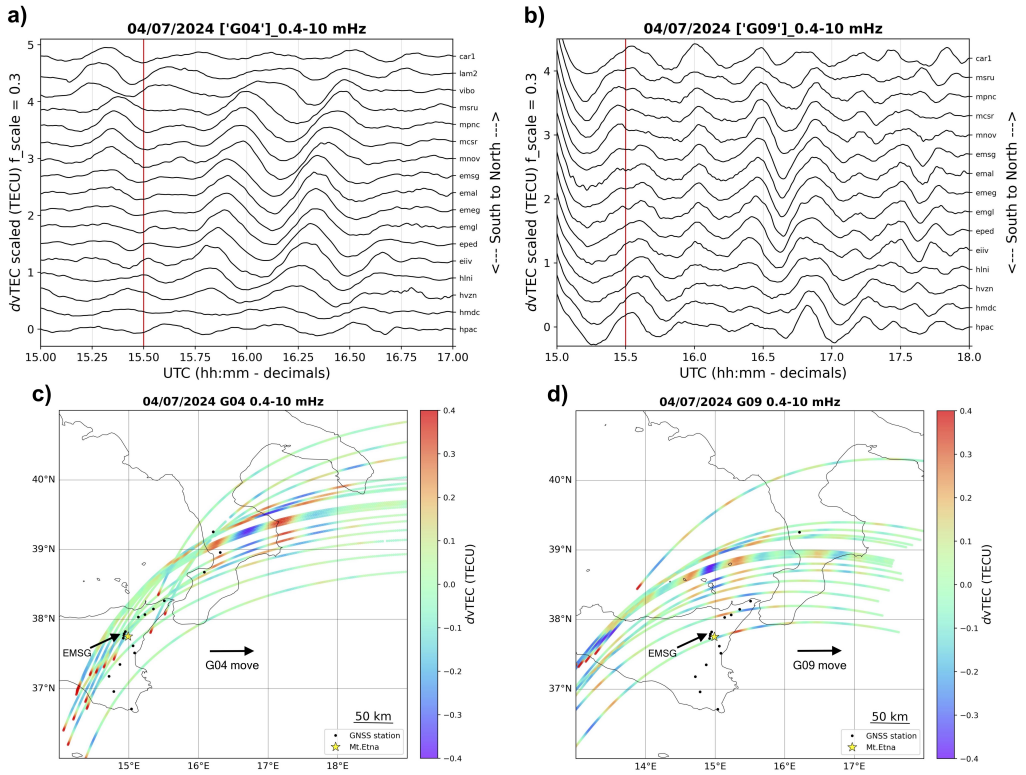

Figure 6.3: a, b) TEC time series from the satellites G04 and G09, respectively, in line-of-sight with the GNSS ground-baseline. The G04 time series stops one hour before the G09 ones because the interruption of the detection; c, d) TEC maps of the satellites G04 and G09 showing the previous time series as a function of latitude, longitude and amplitude. The westward propagation of the local TEC anomaly is recognizable. The site of the reference station EMSG is indicated.

Figures 6.3c,d show the TEC maps for both satellites. Since the satellite G04 detects the TEC anomaly first, then these local co-volcanic disturbances propagate westward. Both satellites G04 and G09 are in ascending orbits from the south to the northeast and then their IPP velocity vectors $\vec{v_{ipp}}$ are opposite to the TEC signature movement. An evident detail can be noted on the TEC maps: the long distance between the G04 detection and the zenith of Etna. This means that, based on the previous time series, the satellite G04 detects the TEC anomaly first but at longer distances than the satellite G09, and this is contradictory. Specifically, the local features of the TEC anomaly, as usual for the previous case studies observed at the Etna volcano, leads to consider the volcanic origin but, on the other hand,

the longer distance of the first detection may be related to other factors like winds or ionospheric currents already ongoing. Figure 6.4 shows outputs of the integrated spectral analysis by Fast Fourier Transform (FFT), Empirical Mode Decomposition (EMD) and Continuous Wavelet Transform (CWT). The differential TEC data is recovered by the records of EMSG station for both satellites G04 and G09. The EMSG station is selected since it is among the receivers recording higher TEC amplitudes and since its line-of-sight travels in free air. Figures 6.4c,d show the first three intrinsic mode functions (IMFs) of the differential TEC records for both satellites G04 and G09. The IMF_2 from the pair G04 - EMSG is characterized by a significant one big cycle of TEC fluctuation lasting around 30 min and with an amplitude comparable to that of the input signal (Fig. 6.4a). This mode represents most of the TEC anomaly observed. On the other hand, also the time series of the pair G09 - EMSG is characterized by an IMF_2 lasting around 30 min as the main mode of oscillation, but the amplitude is around half than the input signal. This less amplitude of IMF_2 is probably due to the dispersion. Indeed, the satellite G09 detects the TEC anomaly after the G04 one, that is during the propagation and when the higher frequency components can be already attenuated. However, both intrinsic modes IMF_2 for the two pairs oscillate during the eruption with the main period of about 30 min, and then these IMF_2 are representative of the local TEC anomalies. Figures 6.4e,f show the amplitude spectra, obtained by FFT, for the previous intrinsic mode functions. The amplitude spectrum of the IMF_2, related to the pair G04 - EMSG, is characterized by a peak frequency $f_{G04} \sim 0.52$ mHz ($\tau_{G04} \sim 1900$ s). On the other hand, the amplitude spectrum of the IMF_2 related to the pair G09 - EMSG has a peak frequency $f_{G09} \sim 0.65$ mHz ($\tau_{G09} \sim 1540$ s). Then the satellites G04 and G09 detect similar components of the local co-volcanic ionospheric perturbation during its westward propagation. Finally, Figures 6.4g,h show the power spectral densities (PSD) of the previous intrinsic modes for both satellites obtained by continuous wavelet transform. Regarding the pair G04 - EMSG, it can be noted that high values of PSD dominate the time-periods domain during the occurrence of IMF_2. It is a broad region of PSD that is characterized by one peak around 16:00 UTC. Similar power distribution is that related to the IMF_2 of the pair G09 - EMSG. Indeed, also for this second detection it can be noted a broad PSD distribution with one peak around 16:30 UTC. Both periods recovered by CWT fit with those of the input signals.

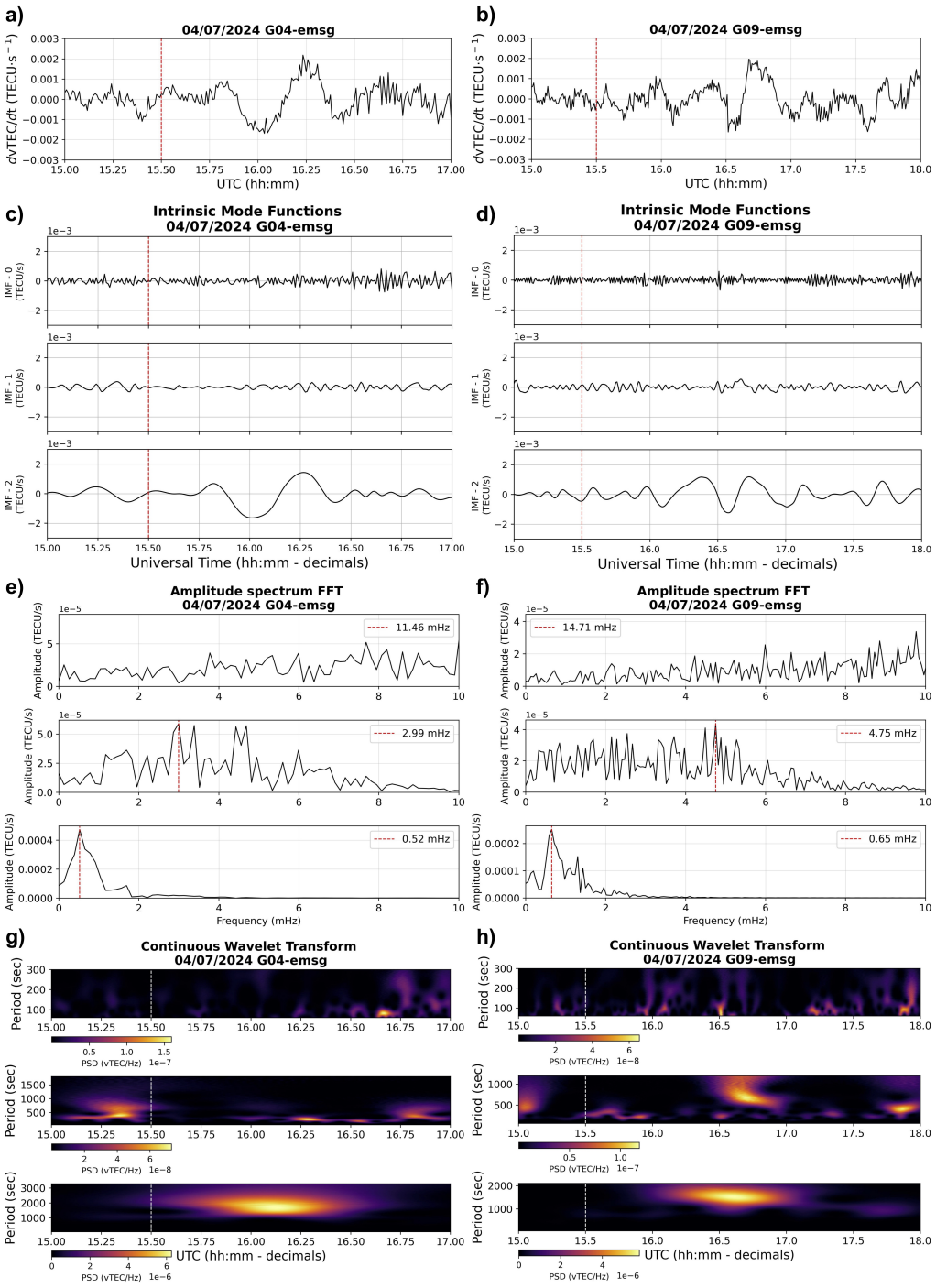

Figure 6.4: a, b) raw differential TEC time series for the pairs G04 - EMSG and G09 - EMSG, respectively; c, d) first three intrinsic modes for the pairs G04 - EMSG and G09 - EMSG, respectively, with the main mode IMF_2 decomposed for both satellites; e, f) FFT amplitude spectra for the pairs G04 - EMSG and G09 - EMSG with peak frequencies of the IMFs; g, h) power spectral densities of the previous IMFs as a function of time and frequency by CWT. The red and white dashed lines in a), b), c), d), g), h) indicate the seismo-acoustic onset of the eruption; the red dashed lines in e), f) indicate the peak frequencies.

Once defined the spectral characteristics of these local co-volcanic ionospheric disturbances, the TEC time series are analyzed to estimate the picking time of the TEC perturbation onset into the ionosphere. The time series of Figure 6.3 show that the TEC amplitude starts to rise with an emergent, reversed, onset around 16:00 UTC in the line-of-sights of satellite G04. The application of EMD on the TEC time series, related to the satellite G04, reveals that the low internal gravity frequencies of this TEC anomaly can make it difficult a time picking of the onset.

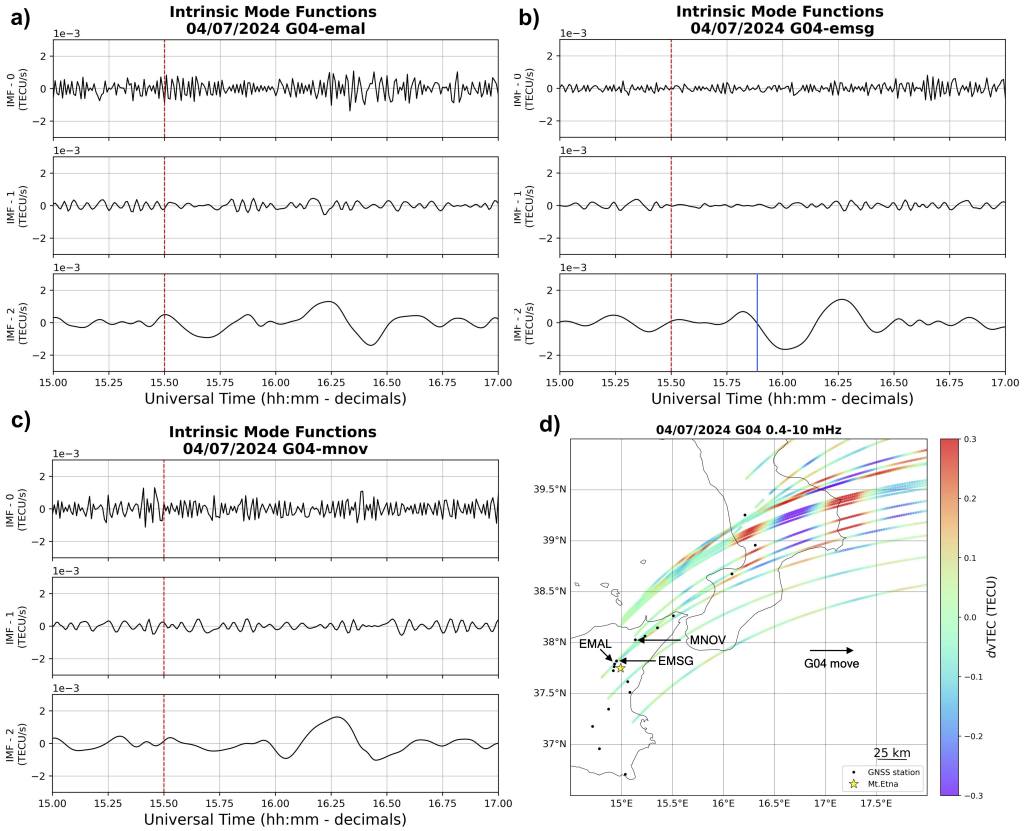

Figure 6.5: Time picking estimation from the intrinsic mode functions; a) first three intrinsic modes of the pair G04 - EMAL in which the IMF_2 is not stable; b) first three intrinsic modes of the pair G04 - EMSG in which the IMF_2 is stable; c) first three intrinsic modes of the pair G04 - MNOV in which the IMF_2 is again stable and then it represents a coherent structure; d) TEC map showing the GNSS station locations used for the TEC anomaly picking time. The red dashed lines in a), b), c) indicate the seismo-acoustic onset of the eruption. The blue solid line in b) indicates the picking time of the co-volcanic TEC signature.

Figure 6.5 shows the empirical mode decomposition of the records from EMAL, EMSG and MNOV stations in line-of-sight with the satellite G04. All the three records show the TEC amplitude anomaly in the time domain (Fig. 6.3a) but the main intrinsic mode IMF_2 becomes stable only starting from the EMSG record. Specifically, despite the TEC amplitudes are

similar to the previous case studies, the low gravity frequencies of this local TEC signature can make it difficult the mode-based time picking of the perturbation onset. This because the empirical mode decomposition identifies the main intrinsic mode from a GNSS station (EMSG) that records the TEC anomaly after other stations. This means that, in the time domain, the picking time of TEC anomaly can be recognized at the HVZN or HLNI stations records, instead by the EMD the intrinsic mode-based picking time is at the EMSG station at t_0 = 15:53:23 UTC. Based on the picking time t_0, local electron density fluctuations above the Etna volcano starts around 25 min after the seismo-acoustic onset of the eruption. This onset time t_0 is similar to that of the December case study and also the frequencies are very similar if we consider the satellites going away from the source. From the tabular outputs of VARION it is recovered that the TEC perturbation has a direction $\delta_{AGW} \sim$ N118°E, while the IPP velocity vectors of the satellites G04 and G09 are both opposite to the wave, along the same direction δ_{ipp}^{G04} = $\delta_{ipp}^{G09} \sim$ N70°E (Fig. 6.3c,d). Then, the IPPs of both satellites G04 and G09 move away from Etna with different velocities $v_{ipp}^{G04} \sim 60$ m·s^{-1} and $v_{ipp}^{G09} \sim 19$ m·s^{-1}. Knowing the peak frequencies from both satellites G04 and G09, the wave equation eq.(4.2) returns an apparent horizontal phase velocity $V_{HA} \sim 146$ m·s^{-1}, intrinsic period $\tau_0 \sim 1400$ s and intrinsic horizontal wavelength $\lambda_x \sim 205$ km. The horizontal apparent phase velocity V_{HA} is different but of the same order of magnitude than the apparent one v_{HA} estimated from the hodochrones (Fig. 6.2).

Chapter 7

Discussion

The Total Electron Content (TEC) is among the most important parameters to analyze the effects of volcanic eruptions in ionosphere. The global scale coverage provided by Global Navigation Satellite Systems (GNSS) is an important condition to obtain reliable estimations of co-volcanic TEC fluctuations. The Co-Volcanic Ionospheric Disturbances (CVIDs), presented in this dissertation, show the typical ionospheric response that can occur above the Etna volcano during explosive eruptions, noted as large-scale lava fountains. Starting from 2000, the eruption column H and the mass eruption rate Q are used as discriminating parameters to focus on the most energetic Etna's eruptions until 2021. Although H and Q are not the highest, co-volcanic TEC signatures are observed during the morning paroxysm of December 4^{th} 2015. This eruption is the main case study around which this research was developed. Specifically, these TEC signatures are analyzed into a multidisciplinary framework integrated by seismic, infrasonic, video, plume and ray-tracing modeling data, in such a way to recognize space-time relations between the volcanological data and the TEC ones. Once verified the volcanic source of the December TEC fluctuations, the study extends to new CVIDs that are observed during the large-scale lava fountains that occurred on April 12^{th} 2012 and July 4^{th} 2024.

Focusing on the observations, the CVIDs appear as spot-like TEC anomaly showing 1 - 2 cycles of complete peak oscillations reaching values around 0.3 - 0.6 TECU. The peak frequency f_0 varies around 1 mHz and the electron density fluctuation lasts around 30 - 45 minutes to disappear beyond 200 - 300 km of Mt. Etna. Two types of velocity are analyzed: the horizontal apparent velocity v_{HA}, estimated from the travel time diagrams of the multiple satellite-station pairs of GNSS network, varying around 135 - 300 $m \cdot s^{-1}$

with average value around 200 m·s^{-1}; the horizontal apparent phase velocity V_{HA}, calculated by eq.(4.2), varying around 50 - 150 m·s^{-1}. Finally, by V_{HA}, horizontal wavelengths λ_x varying around 50 - 200 km are obtained. Tables 7.1 and 7.2 show the features of the eruptions and of the observed CVIDs at Mt. Etna, respectively.

Table 7.1: Volcanological and seismo-acoustic data of the three Etna's eruptions. Fountain heights are reported as average values while plume, seismic velocity and infrasonic pressure values are reported as maximum values.

Date	Seismo-acoustic activity (UTC)	Fountain height (m)	Plume altitude (km)	Seismic velocity (10^{-5} m·s^{-1})	Infrasonic pressure (Pa)
12/04/2012	14:23 - 15:25	1000	10.2	2.8	2
04/12/2015	08:40 - 11:00	2000	13.1	3.5	15
04/07/2024	15:30 - 01:00	2500	4.5	5.6	3.4

Table 7.2: Characteristics of the co-volcanic ionospheric disturbances observed at the Mt. Etna. TEC amplitudes are reported as peak values.

Date	Onset time t_0 (UTC)	TEC amplitude (TECU)	Peak frequency f_0 (mHz)	Calculated app. phase velocity V_{HA} (m·s^{-1})	Horizontal wavelength λ_x (km)
12/04/2012	16:39	0.3	0.92	121	131
04/12/2015	09:00	0.6	1.1	55	51
04/07/2024	15:53	0.4	0.72	146	205

The co-volcanic TEC signatures observed at Mt. Etna show peak frequencies f_0 falling into gravity frequency range. However, even if f_0 varies into a short interval among the three case studies, the co-volcanic TEC signatures show important variations of apparent phase velocity and different travel times to reach the ionospheric shell. Regarding the velocity, the higher V_{HA} the higher λ_x and the period τ_0 (i.e. the inverse of f_0), and this may indicates normal dispersion being consistent with near-field propagation and ionospheric refraction of radio waves; however the more energetic eruption (i.e. December's one) is related to the lowest V_{HA}. Regarding the travel time, the onset time t_0 of TEC signatures observed in December and July are around 20 minutes after the seismo-acoustic onset of the eruption, whereas t_0 for April eruption is more than 2 hours after the seismo-acoustic onset. These observations highlight that V_{HA} seems to doesn't fit with the eruptive power and that the ionospheric response can occur with different delays.
A partial explanation for these results may be related to the atmospheric

conditions of the GNSS data acquisition and to the type of eruption. The geographic localizations of these local CVIDs seem to fit with the prevalent wind components. Indeed, since the upwind facilitates the upward atmospheric waves propagation, the appearance of the TEC signatures in December and July are consistent with the direction of the prevalent wind component [30]. Less clear is the relation between the TEC anomaly localization and the wind in April, when a notable vertical motion of air is the prevalent component (Fig. 7.1).

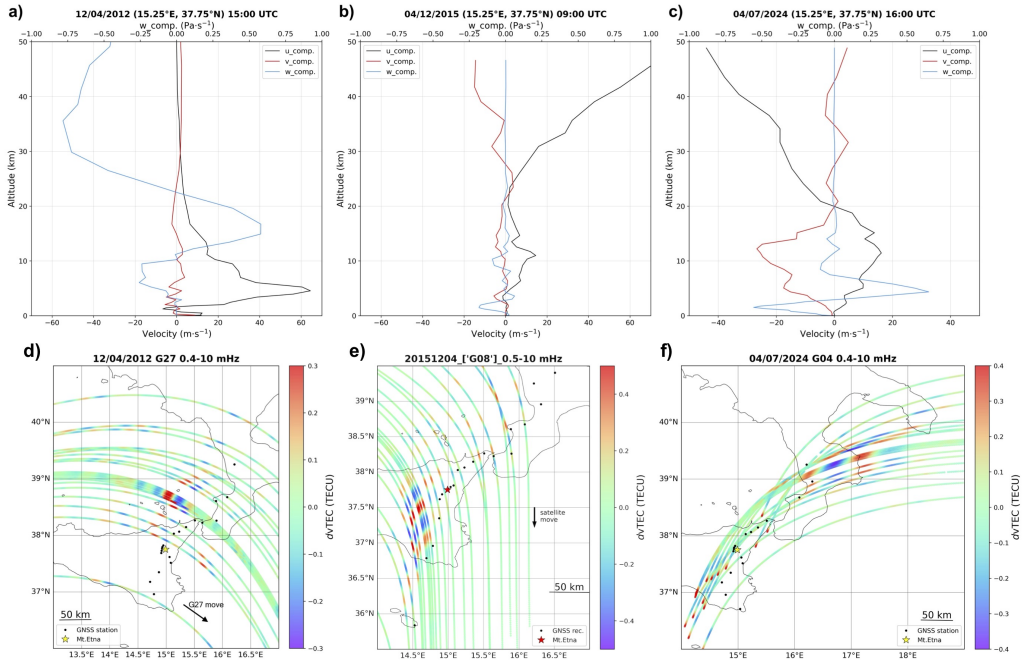

Figure 7.1: a), b), c) wind three-components profiles during the April, December and July eruptions, respectively; the v-comp and u-comp are the meridional and zonal components with positive values northward and eastward, respectively; the w-comp is the wind vertical component with negative values indicating upward motion. Panels d), e), f) show the TEC maps of the CVIDs on the same days of a), b), c) respectively.

Regarding the type of eruption, the large-scale lava fountains occurring at Mt. Etna are paroxysmal activities developing gradually in time, in such a way that this type of source may not be considered properly impulsive. Indeed, higher lava fountains are sustained by sequences of discontinuous gas slugs coming from the deep. This means that the gradual seismo-acoustic intensification of the lava fountaining activity at Mt. Etna can induce a gradual thermodynamic forcing of the lower atmosphere, as the effect of a superimposition of warm air pulses. The result is the generation of co-volcanic acoustic-gravity waves (AGWs) amplifying upward by the double effect due, on one side, to the thermo-seismo-acoustic intensification of the eruption and, from the other side, to the atmospheric amplification.

The discrepancies in t_0, among the three case studies, lead to assume that the CVIDs on April eruption are related to different factors than the December and July eruptions. However, these factors should be related to atmospheric forcing processes from below. Indeed, although the TEC signatures in April occur when the ionosphere undergoes to a weak increase of geomagnetic activity at the global scale, the spot-like appearance of CVIDs leads to consider primarily the volcanic origin. This means that, starting from the thermodynamic forcing of the lower atmosphere, the local coupling processes between the geospheres, at Mt. Etna, could be severely affected by volcanic and/or atmospheric "small-scale" features that could be influent for VEI ≤ 3 eruptions. Figure 7.2 shows a scheme of the hypothetical local processes that occurred at the Mt. Etna during the eruptions here analyzed.

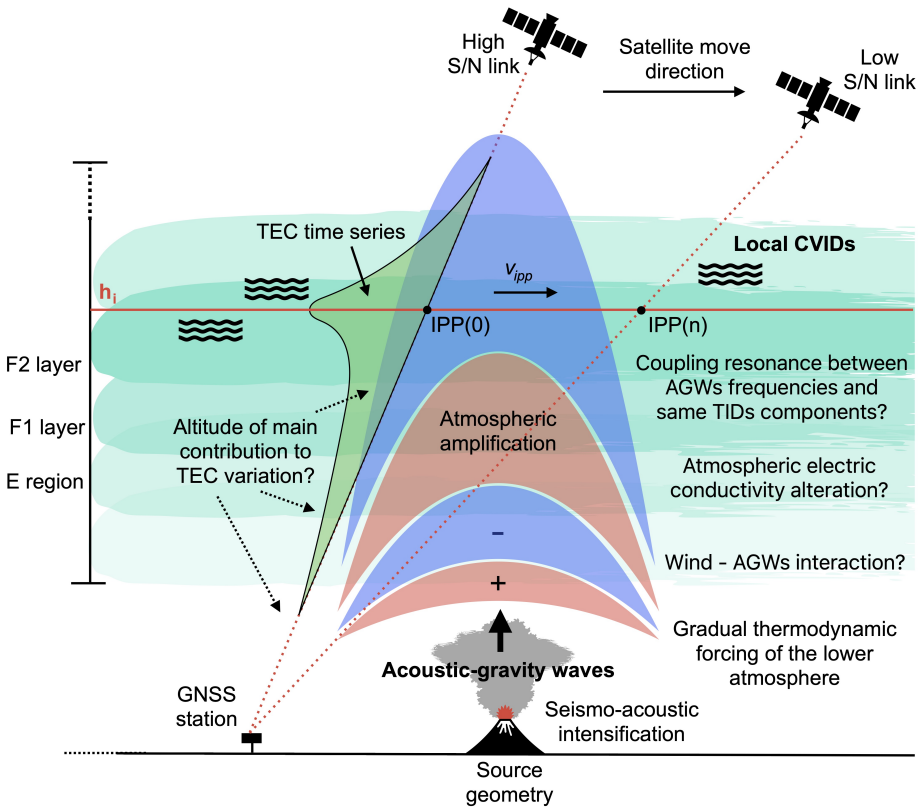

Figure 7.2: Conceptual scheme of the local coupling processes induced by paroxysmal activity of Mt. Etna. The gradual seismo-acoustic intensification, due to the developing of gas-slugged fire fountain, transfers a superimposition of warm air pulses into the atmosphere. The result is a gradual thermodynamic forcing of the lower atmosphere generating upward acoustic-gravity waves amplifying by the double effect of the eruptive dynamics and the atmospheric amplification. Finally, the thermodynamic perturbation of air affects the local electron density distribution, by inducing near field TEC fluctuations detectable from GNSS.

Getting a focus on the techniques, the GNSS-based method for TEC estimations has own limitation that, as explained in paragraph 3.1.2, can affect the evaluation of spatial-time relations from the eruption onset. The integration of ionospheric measurements, like Doppler sounder, may provide a better precision to pick the right altitude of co-volcanic TEC variations. On the other hand, the dense and proximal GNSS network around the Etna volcano enables the detection of CVIDs with unprecedented spatial and temporal resolution. Nevertheless, these local CVIDs are subtle and non-impulsive making their detection challenging, especially under conditions of natural ionospheric variability.

It is not clear if the dynamic coupling process only may explain the observation of local CVIDs at Mt. Etna. The spot-like appearance of these electron density fluctuations and their waveforms, during lava fountaining activity, lead us to maintain the focus on the thermodynamic coupling as the first local coupling process between the Etna's area and the surrounding atmosphere. Specifically, due to its continuous state of activity, Mt. Etna is a so-called "open-conduit volcano" implying a quite direct linkage between the deep lithospheric (magmatic) source and the atmosphere [36]. Therefore, open-conduit eruptive dynamics, like the Etna lava fountaining, likely facilitates direct energy transfer as a vertical long-size source of internal gravity waves [37]. Although ionospheric plasma perturbations induced by Etna's eruptive activity have been observed by a few authors, these findings report unprecedented space-time characteristics of the electron density oscillations as TEC signatures. For this reasons, future works need to evaluate: 1) local electromagnetic coupling processes (i.e. magnetic data); 2) integration of ionospheric measurements (i.e. Doppler sounder); 3) ray-tracing modeling with the wind; 4) application of automated TEC analysis on multiple explosive Etna's eruptions.

Chapter 8

Conclusion

The coupling processes of geospheres, from the lithosphere to the upper atmosphere, induced by volcanic activity, have been studied into regional scale at the Etna Observatory of the Istituto Nazionale di Geofisica e Vulcanologia (INGV-OE), Italy. The ionospheric forcing from three large-scale lava fountains, that occurred at Mt. Etna (Italy) on April 12$^{\text{th}}$ 2012, December 4$^{\text{th}}$ 2015 and July 4$^{\text{th}}$ 2024, is studied as ionospheric Total Electron Content (TEC) variations recovered from Global Navigation Satellite Systems (GNSS) data. The analysis of TEC time series, integrated by a multidisciplinary framework of seismo-acoustic and video data, reveal fluctuations occurring in the near field, up to 200 - 300 km of the volcano, amplitudes A $\sim$ 0.3 - 0.6 TECU, estimated horizontal apparent velocity $v_{HA} \sim 200$ m·s^{-1}, intrinsic peak frequency $f_0 \sim 1$ mHz. The intrinsic peak frequency is typical of internal gravity waves by suggesting that the Etna paroxysmal activity is coupled with the ionospheric electron density layers through the lower atmosphere. Specifically, the near field occurrence of these co-volcanic ionospheric disturbances leads to say that the open-conduit eruptive dynamics, as those of Etna volcano, likely facilitate direct energy transfer, from the deep to the ionosphere, as a vertical long-size source of internal gravity waves. These findings provide potential guidelines for the ionospheric detection and characterization of Etna paroxysmal activity, as well as the implementation of the current volcano monitoring framework. Mt. Etna is among the best monitored volcanoes in the world with different sensors and the multi-data analysis of its activity can provide new information to understand the rest - unrest transition states.

Acknowledgements

I thank the University of Trento, in particular the Ph.D. coordinator Prof. Roberto Battiston for the excellent formative experience. I thank all the professors and researchers of the Ph.D. Consortium that have been available to make possible this national doctoral program. I thank the Secretariat, in particular Dr. Gaia Fanelli, for the inexhaustible support and the Ufficio Missioni - Polo Collina for the immaculate service about my missions.
I thank the Istituto Nazionale di Geofisica e Vulcanologia (INGV), in particular the Etna Observatory in Catania (Italy), for the professional and human experience as my operative site.
I thank my supervisors Dr. Alessandro Bonforte, Dr. Michela Ravanelli and Dr. Jaroslav Chum for being available for my needs and for their precious suggestions.
I thank also the Institute of Atmospheric Physics of Prague (Czechia) for my abroad period.
I thank Dr. Simona Scollo, Dr. Mariangela Sciotto and Dr. Luigi Mereu for the volcanological data.
I am glad to met Prof. Vincenzo Carbone and Dr. Vincenzo Capparelli, from University of Calabria (Italy), for the scientific collaboration.
I thank Prof. Andrea Cannata, from University of Catania, for the scientific collaboration.
I thank Prof. Mirko Piersanti and Dr. Giulia D'Angelo for the proficue days spent at the University of L'Aquila (Italy).
I thank Dr. Giuseppe Puglisi for the considerations about my work.
I thank the revisors for the suggestions about the final version of this thesis.
I thank my family to give me further reasons to believe in my scientific knowledge and in my progress.

Bibliography

1. Andrews, D. *An Introduction to Atmospheric Physics* ISBN: 9780511800788. doi:https://doi.org/10.1017/CBO9780511800788 (Cambrige University Press, 2010).

2. Andronico, D., Cannata, A., Di Grazia, G. & Ferrari, F. The 1986–2021 paroxysmal episodes at the summit craters of Mt. Etna: Insights into volcano dynamics and hazard. *Earth-Science Reviews* **220.** doi:https://doi.org/10.1016/j.earscirev.2021.103686 (2021).

3. Astafyeva, E. *et al.* The 15 January 2022 Hunga Tonga Eruption History as Inferred From Ionospheric Observations. *Geophysical Research Letters* **49.** doi:https://doi.org/10.1029/2022GL098827 (2022).

4. Astafyeva, E. Ionospheric Detection of Natural Hazards. *Reviews of Geophysics* **57.** doi:https://doi.org/10.1029/2019RG000668 (2019).

5. Balthazor, R. & Moffett, R. A study of atmospheric gravity waves and traveling ionospheric disturbances at equatorial latitudes. *Annales Geophysicae* **15.** doi:https://doi.org/10.1007/s00585-997-1048-4 (1997).

6. Bartels, J. in *Geomagnetism* (Pergamon, 2013). doi:https://doi.org/10.1016/B978-1-4832-1304-0.50006-3.

7. Behncke, B. *et al.* The 2011-2012 summit activity of Mount Etna: Birth, growth and products of the new SE crater. *Journal of Volcanology and Geothermal Research* **270.** ISSN: 0377-0273. doi:https://doi.org/10.1016/j.jvolgeores.2013.11.012 (2014).

8. Belehaki, A. *et al.* An overview of methodologies for real-time detection, characterisation and tracking of Traveling Ionospheric Disturbances developed in the TechTIDE project. *Journal of Space Weather and Space Climate* **10.** doi:https://doi.org/10.1051/swsc/2020043 (2020).

9. Bilitza, D. *et al.* The International Reference Ionosphere Model: A Review and Description of an Ionospheric Benchmark. *Reviews of Geophysics* **60.** doi:https://doi.org/10.1029/2022RG000792 (2022).

10. Bonadonna, C. & Costa, A. Plume height, volume, and classification of explosive volcanic eruptions based on the Weibull function. *Bulletin of Volcanology* **75.** doi:10.1007/s00445-013-0742-1 (2013).

11. Bonadonna, C. & Phillips, J. C. Sedimentation from strong volcanic plumes. *Journal of Geophysical Research: Solid Earth* **108.** doi:https://doi.org/10.1029/2002JB002034 (2003).

12. Bonforte, A., Cannavò, F., Gambino, S. & Guglielmino, F. Combining High- and Low-Rate Geodetic Data Analysis for Unveiling Rapid Magma Transfer Feeding a Sequence of Violent Summit Paroxysms at Etna in Late 2015. *Applied Sciences.* doi:https://doi.org/10.3390/app11104630 (2021).

13. Cahyadi, M. N., Handoko, E. Y., Rahayu, R. W. & Heki, K. Comparison of volcanic explosions in Japan using impulsive ionospheric disturbances. *Earth, Planets and Space* **73.** doi:https://doi.org/10.1186/s40623-021-01539-5 (2021).

14. Calvari, S., Cannavò, F., Bonaccorso, A., Spampinato, L. & Pellegrino, A. G. Paroxysmal Explosions, Lava Fountains and Ash Plumes at Etna Volcano: Eruptive Processes and Hazard Implications. *Frontiers in Earth Science* **6.** doi:https://doi.org/10.3389/feart.2018.00107 (2018).

15. Calvari, S. & Nunnari, G. Reawakening of Voragine, the Oldest of Etnas Summit Craters: Insights from a Recurrent Episodic Eruptive Behavior. *Remote Sensing* **16.** doi:10.3390/rs16224278 (2024).

16. Cannata, A. *et al.* Monitoring Seismo-volcanic and Infrasonic Signals at Volcanoes: Mt. Etna Case Study. *Pure and Applied Geophysics.* doi:https://doi.org/10.1007/s00024-012-0634-x (2013).

17. Capparelli, V. *et al.* A spatiotemporal analysis of U.S. station temperature trends over the last century. *Journal of Geophysical Research: Atmospheres* **118.** doi:https://doi.org/10.1002/jgrd.50551 (2013).

18. Carbone, V. *et al.* A mathematical model of lithosphereatmosphere coupling for seismic events. *Scientific Reports* **11.** doi:https://doi.org/10.1038/s41598-021-88125-7 (2021).

19. Carey, S. & Bursik, M. in *Encyclopedia of Volcanoes* (eds Sigurdsson, H., Houghton, B., Rymer, H., Stix, J. & McNutt, S.) Part IV (Academic Press, 1999). ISBN: 9780080547985.

20. Carey, S. & Sparks, R. S. J. Quantitative models of the fallout and dispersal of tephra from volcanic eruption columns. *Bulletin of Volcanology* **48.** doi:10.1007/BF01046546 (1986).

21. Chum, J. *et al.* Atmospheric and ionospheric waves induced by the Hunga eruption on 15 January 2022; Doppler sounding and infrasound. *Geophysical Journal International* **233.** doi:https://doi.org/10.1093/gji/ggac517 (2022).

22. Ciraolo, L., Azpilicueta, F., Brunini, C., Meza, A. & Radicella, S. Calibration errors on experimental slant total electron content (TEC) determined with GPS. *Journal of Geodesy* **81.** doi:10.1007/s00190-006-0093-1 (2007).

23. Coco, I. & Tozzi, R. *10 maggio 2024: la più forte tempesta magnetica degli ultimi vent'anni* (Istituto Nazionale di Geofisica e Vulcanologia, Italy, 2024). https://ingvambiente.com/2024/06/17/10-maggio-2024-la-piu-forte-tempesta-magnetica-degli-ultimi-ventanni/.

24. Contadakis, M. E., Arabelos, D. & Scordilis, E. Lower Ionospheric Turbulence Variations During the Recent Activity of Etnas Volcano, Sicily, in December 2018. *Bulletin of the Geological Society of Greece* **55.** doi:https://doi.org/10.12681/bgsg.20517 (2019).

25. Cooley, J. W. & Tukey, J. W. An Algorithm for the Machine Calculation of Complex Fourier Series. *Mathematics of Computation* **19.** doi:https://doi.org/10.2307/2003354 (1965).

26. Corsaro, R. *et al.* Monitoring the December 2015 summit eruptions of Mt. Etna (Italy): Implications on eruptive dynamics. *Journal of Volcanology and Geothermal Research* **341.** doi:https://doi.org/10.1016/j.jvolgeores.2017.04.018 (2017).

27. Dautermann, T. & Calais, E. *TEC Data Processing Software* (Purdue University, 2008).

28. Dautermann, T., Calais, E. & Mattioli, G. S. Global Positioning System detection and energy estimation of the ionospheric wave caused by the 13 July 2003 explosion of the Soufrière Hills Volcano, Montserrat. *Journal of Geophysical Research: Solid Earth* **114.** doi:https://doi.org/10.1029/2008JB005722 (2009).

29. Davies, K. *Ionospheric radio propagation* **NBS MONO 80.** doi:https://doi.org/10.6028/NBS.MONO.80 (National Institute of Standards and Technology, Gaithersburg, MD, 1965).

30. Ding, F., Wan, W. & Yuan, H. The influence of background winds and attenuation on the propagation of atmospheric gravity waves. *Journal of Atmospheric and Solar-Terrestrial Physics* **65.** doi:https://doi.org/10.1016/S1364-6826(03)00090-7 (2003).

31. Donn, W. L. & Shaw, D. M. Exploring the atmosphere with nuclear explosions. *Reviews of Geophysics* **5.** doi:https://doi.org/10.1029/RG005i001p00053 (1967).

32. Estey, L. H. & Meertens, C. M. TEQC: The Multi-Purpose Toolkit for GPS/GLONASS Data. *GPS Solutions* **3.** doi:https://doi.org/10.1007/PL00012778 (1999).

33. Evers, L. G. & Haak, W. in *Infrasound Monitoring for Atmospheric Studies* (eds Le Pichon, A., Blanc, E. & Hauchecorne, A.) chap. 1 (Springer, 2010). ISBN: 978-1-4020-9507-8. doi:10.1007/978-1-4020-9508-5.

34. Farge, M. WAVELET TRANSFORMS AND THEIR APPLICATIONS TO TURBULENCE. *Annual Review of Fluid Mechanics* **24.** doi:https://doi.org/10.1146/annurev.fl.24.010192.002143 (1992).

35. Fee, D. *et al.* Volcanic tremor and plume height hysteresis from Pavlof Volcano, Alaska. *Science* **355.** doi:https://doi.org/10.1126/science.aah6108 (2017).

36. Ferlito, C., Coltorti, M., Lanzafame, G. & Giacomoni, P. P. The volatile flushing triggers eruptions at open conduit volcanoes: Evidence from Mount Etna volcano (Italy). *Lithos* **184-187.** doi:https://doi.org/10.1016/j.lithos.2013.10.030 (2014).

37. Ferrara, F. *et al.* Ionospheric Disturbances During the 4 December 2015, Mt. Etna Eruption. *Earth and Space Science* **12.** doi:https://doi.org/10.1029/2025EA004214 (2025).

38. Fritts, D. C. & Alexander, M. J. Gravity wave dynamics and effects in the middle atmosphere. *Reviews of Geophysics* **41.** doi:https://doi.org/10.1029/2001RG000106 (2003).

39. GeoDAF. *Geodetic Data Archive Facility* Agenzia Spaziale Italiana, Roma, Italy. http://geodaf.mt.asi.it.

40. GFZ Data Services. *German Research Centre for Geosciences* 2024. https://www.gfz-potsdam.de/en.

41. Hargreaves, J. K. *The Solar-Terrestrial Environment* doi:https://doi.org/10.1017/CBO9780511628924 (Cambridge University Press, 1992).

42. Harkrider, D. G. Theoretical and observed acoustic-gravity waves from explosive sources in the atmosphere. *Journal of Geophysical Research (1896-1977)* **69.** doi:https://doi.org/10.1029/JZ069i024p05295 (1964).

43. Heki, K. Explosion energy of the 2004 eruption of the Asama Volcano, central Japan, inferred from ionospheric disturbances. *Geophysical Research Letters* **33.** doi:https://doi.org/10.1029/2006GL026249 (2006).

44. Heki, K. Atmospheric resonant oscillations by the 2022 January 15 eruption of the Hunga TongaHunga Ha'apai volcano from GNSS-TEC observations. *Geophysical Journal International* **236.** doi:https://doi.org/10.1093/gji/ggae023 (2024).

45. Hidayati, S., Ishihara, K. & Iguchi, M. Volcano-tectonic Earthquakes during the Stage of Magma Accumulation at the Aira Caldera, Southern Kyushu, Japan. *Bull. Volcanol. Soc. Japan* **52.** doi:10.18940/kazan.52.6_289 (2007).

46. Hines, C. O. Internal atmospheric gravity waves at ionospheric heights. *Canadian Journal of Physics* **38.** doi:https://doi.org/10.1139/p60-150 (1960).

47. Hocke, K. & Schlegel, K. A review of atmospheric gravity waves and travelling ionospheric disturbances: 1982-1995. *Ann. Geophysicae* **14.** doi:https://doi.org/10.1007/s00585-996-0917-6 (1996).

48. Hofmann-Wellenhof, B., Lichtenegger, H. & Wasle, E. *GNSS - Global Navigation Satellite Systems* ISBN: 9783211730126 (SpringeWienNewYork, 2008).

49. Huang, N. E. *et al.* The empirical mode decomposition and the Hilbert spectrum for nonlinear and non-stationary time series analysis. *Proceedings of the Royal Society of London. Series A: Mathematical, Physical and Engineering Sciences* **454.** doi:https://doi.org/10.1098/rspa.1998.0193 (1998).

50. Ichihara, M. Seismic and infrasonic eruption tremors and their relation to magma discharge rate: A case study for sub-Plinian events in the 2011 eruption of Shinmoedake, Japan. *Journal of Geophysical Research: Solid Earth* **121.** doi:https://doi.org/10.1002/2016JB013246 (2016).

51. Kanamori, H., Mori, J. & Harkrider, D. G. Excitation of atmospheric oscillations by volcanic eruptions. *Journal of Geophysical Research: Solid Earth* **99.** doi:https://doi.org/10.1029/94JB01475 (1994).

52. Klobuchar, J. *et al.* in *Handbook of geophysics and the space environment* (ed Jursa, A.) chap. 10 (1985). https://www.cnofs.org/Handbook_of_Geophysics_1985/Handbook.pdf.

53. Lamb, H. On atmospheric oscillations. *Proceedings of the Royal Society of London. Series A, Containing Papers of a Mathematical and Physical Character* **84.** doi:10.1098/rspa.1911.0008 (1911).

54. Lizunov, G. & Hayakawa, M. Atmospheric Gravity Waves and their Role in the Lithosphere-troposphere-ionosphere Interaction. *Institute of Electrical Engineers of Japan Journal A* **124.** doi:https://doi.org/10.1541/ieejfms.124.1109 (2004).

55. Longpré, M. A. Reactivation of Cumbre Vieja volcano. *Science* **374.** doi:10.1126/science.abm9423 (2021).

56. Luhmann, J. in *Introduction to Space Physics* (eds Kivelson, M. G. & Russel, C. T.) chap. 7 (Cambridge University Press, 1995). ISBN: 9781139878296. doi:https://doi.org/10.1017/9781139878296.

57. Macleod, M. A. Sporadic E Theory. I. Collision-Geomagnetic Equilibrium. *Journal of Atmospheric Sciences* **23.** doi:https://doi.org/10.1175/1520-0469(1966)023<0096:SETICG>2.0.CO;2 (1966).

58. Madonia, P. *et al.* Propagation of Perturbations in the Lower and Upper Atmosphere over the Central Mediterranean, Driven by the 15 January 2022 Hunga Tonga-Hunga Haapai Volcano Explosion. *Atmosphere* **14.** doi:https://doi.org/10.3390/atmos14010065 (2023).

59. Maletckii, B. & Astafyeva, E. Near-Real-Time Identification of the Source of Ionospheric Disturbances. *Journal of Geophysical Research: Space Physics* **129.** doi:https://doi.org/10.1029/2024JA032664 (2024).

60. Mannucci, A. J. *et al.* A global mapping technique for GPS-derived ionospheric total electron content measurements. *Radio Science* **33.** doi:https://doi.org/10.1029/97RS02707 (1998).

61. Manta, F., Occhipinti, G., Feng, L. & Hill, E. Rapid identification of tsunamigenic earthquakes using GNSS ionospheric sounding. *Scientific Reports* **10.** doi:10.1038/s41598-020-68097-w (2020).

62. Manta, F. *et al.* Correlation Between GNSS-TEC and Eruption Magnitude Supports the Use of Ionospheric Sensing to Complement Volcanic Hazard Assessment. *Journal of Geophysical Research: Solid Earth* **126.** doi:https://doi.org/10.1029/2020JB020726 (2021).

63. Mastin, L. *et al.* A multidisciplinary effort to assign realistic source parameters to models of volcanic ash-cloud transport and dispersion during eruptions. *Journal of Volcanology and Geothermal Research* **186.** doi:https://doi.org/10.1016/j.jvolgeores.2009.01.008 (2009).

64. Matoza, R. S., Fee, D., Neilsen, T. B., Gee, K. L. & Ogden, D. E. Aeroacoustics of volcanic jets: Acoustic power estimation and jet velocity dependence. *Journal of Geophysical Research: Solid Earth* **118.** doi:https://doi.org/10.1002/2013JB010303 (2013).

65. Matoza, R. S. *et al.* Atmospheric waves and global seismoacoustic observations of the January 2022 Hunga eruption, Tonga. *Science* **377.** doi:https://doi.org/10.1126/science.abo7063 (2022).

66. Matzka, J., Stolle, C., Yamazaki, Y., Bronkalla, O. & Morschhauser, A. The Geomagnetic Kp Index and Derived Indices of Geomagnetic Activity. *Space Weather* **19.** doi:https://doi.org/10.1029/2020SW002641 (2021).

67. Mereu, L. *et al.* Ground-Based Remote Sensing and Uncertainty Analysis of the Mass Eruption Rate Associated With the 35 December 2015 Paroxysms of Mt. Etna. *IEEE Journal of Selected Topics in Applied Earth Observations and Remote Sensing* **15.** doi:https://doi.org/10.1109/JSTARS.2021.3133946 (2022).

68. Nakashima, Y. *Multi-sensor study of dynamics of atmospheric waves induced by volcanic eruptions* Doctoral dissertation (Hokkaido University, 2018). http://hdl.handle.net/2115/69524.

69. Nakashima, Y. *et al.* Atmospheric resonant oscillations by the 2014 eruption of the Kelud volcano, Indonesia, observed with the ionospheric total electron contents and seismic signals. *Earth and Planetary Science Letters* **434.** doi:https://doi.org/10.1016/j.epsl.2015.11.029 (2016).

70. Newhall, C. G. & Self, S. The volcanic explosivity index (VEI) an estimate of explosive magnitude for historical volcanism. *Journal of Geophysical Research: Oceans* **87.** doi:https://doi.org/10.1029/JC087iC02p01231 (1982).

71. Nischan, T. *GFZRNX - RINEX GNSS Data Conversion and Manipulation Toolbox. GFZ Data Services* GFZ German Research Centre for Geosciences (2016). doi:https://doi.org/10.5880/GFZ.1.1.2016.002.

72. Nishida, K., Kobayashi, N. & Fukao, Y. Background Lamb waves in the Earth's atmosphere. *Geophysical Journal International* **196.** doi:10.1093/gji/ggt413 (2013).

73. Occhipinti, G. in *Subduction Dynamics* chap. 9 (American Geophysical Union, 2015). doi:https://doi.org/10.1002/9781118888865.ch9.

74. Occhipinti, G., Rolland, L., Lognonné, P. & Watada, S. From Sumatra 2004 to Tohoku-Oki 2011: The systematic GPS detection of the ionospheric signature induced by tsunamigenic earthquakes. *Journal of Geophysical Research: Space Physics* **118.** doi:https://doi.org/10.1002/jgra.50322 (2013).

75. Pfeffer, R. & Zarichny, J. Acoustic-gravity wave propagation in an atmosphere with two sound channels. *Pure and Applied Geophysics* **55.** doi:https://doi.org/10.1007/BF02011231 (1963).

76. Proakis, J. G. & Manolakis, D. G. *Digital signal processing (3rd ed.): principles, algorithms and applications* in (Prentice-Hall, 1996). https://api.semanticscholar.org/CorpusID:67051967.

77. Prölss, G. W. *Physics of the Earth's Space Environment. An Introduction* **2.** ISBN: 978-3-642-05979-7. doi:https://doi.org/10.1007/978-3-642-18807-7 (Springer Berlin, Heidelberg, 2004).

78. Pulinets, S. & Davidenko, D. Ionospheric precursors of earthquakes and Global Electric Circuit. *Advances in Space Research* **53.** doi:https://doi.org/10.1016/j.asr.2013.12.035 (2014).

79. Ravanelli, M., Astafyeva, E., Munaibari, E., Rolland, L. & Mikesell, T. D. Ocean-Ionosphere Disturbances Due To the 15 January 2022 Hunga-Tonga Hunga-Ha'apai Eruption. *Geophysical Research Letters* **50.** doi:https://doi.org/10.1029/2022GL101465 (2023).

80. Ravanelli, M. *et al.* GNSS total variometric approach: first demonstration of a tool for real-time tsunami genesis estimation. *Scientific Reports* **11.** doi:https://doi.org/10.1038/s41598-021-82532-6 (2021).

81. ReVelle, D. O. in *Infrasound Monitoring for Atmospheric Studies* (eds Le Pichon, A., Blanc, E. & Hauchecorne, A.) chap. 11 (Springer, 2010). ISBN: 978-1-4020-9507-8. doi:10.1007/978-1-4020-9508-5.

82. RING. *Rete Integrata Nazionale GNSS* INGV - RING Working Group, Roma, Italy. http://ring.gm.ingv.it.

83. Savastano, G. *New applications and challenges of GNSS variometric approach* Doctoral dissertation (Sapienza Università di Roma, 2018). https://hdl.handle.net/11573/1077041.

84. Savastano, G. *et al.* Real-Time Detection of Tsunami Ionospheric Disturbances with a Stand-Alone GNSS Receiver: A Preliminary Feasibility Demonstration. *Scientific Reports* **7.** doi:10.1038/srep46607 (2017).

85. Scandone, R. & Giacomelli, L. in *Vulcanologia - Principi fisici e metodi d'indagine* chap. 6 (Liguori, 2004). ISBN: 9788820726874.

86. Scase, M. M., Caulfield, C. P. & Dalziel, S. B. Temporal variation of non-ideal plumes with sudden reductions in buoyancy flux. *Journal of Fluid Mechanics* **600,** 181–199. doi:10.1017/S0022112008000487 (2008).

87. Schiavello, M. & Palmisano, L. *Fondamenti di Chimica* ISBN: 9788879595544 (EdiSES, 2010).

88. Sciotto, M. *et al.* Unravelling the links between seismo-acoustic signals and eruptive parameters: Etna lava fountain case study. *Scientific Reports* **9.** doi:https://doi.org/10.1038/s41598-019-52576-w (2019).

89. Shestakov, N. *et al.* Investigation of Ionospheric Response to June 2009 Sarychev Peak Volcano Eruption. *Remote Sensing* **13.** doi:https://doi.org/10.3390/rs13040638 (2021).

90. Shults, K., Astafyeva, E. & Adourian, S. Ionospheric detection and localization of volcano eruptions on the example of the April 2015 Calbuco events. *Journal of Geophysical Research: Space Physics* **121.** doi:https://doi.org/10.1002/2016JA023382 (2016).

91. Tiwari, S. H., Bagiya, M. S., Maurya, S., Heki, K. & Dimri, A. On the role of volcanic plume heights in excitation of free oscillations of the solid Earth and atmosphere: Case study. *Advances in Space Research* **73.** doi:https://doi.org/10.1016/j.asr.2024.01.001 (2024).

92. Tolstoy, I. The Theory of Waves in Stratified Fluids Including the Effects of Gravity and Rotation. *Rev. Mod. Phys.* **35.** doi:10.1103/RevModPhys.35.207 (1963).

93. Toman, I., Bri, D. & Kos, S. Contribution to the Research of the Effects of Etna Volcano Activity on the Features of the Ionospheric Total Electron Content Behaviour. *Remote Sensing* **13.** doi:https://doi.org/10.3390/rs13051006 (2021).

94. Troll, V. R. *et al.* The Fagradalsfjall and Sundhnúkur Fires of 20212024: A single magma reservoir under the Reykjanes Peninsula, Iceland? *Terra Nova* **36.** doi:https://doi.org/10.1111/ter.12733 (2024).

95. Upper Atmosphere Physics and Radiopropagation Working Group *et al. Electronic Space Weather Upper Atmosphere Database (eSWua)HF Validated Data (1.0)* 2020. doi:https://doi.org/10.13127/ESWUA/HFVALIDATED.

96. Vergados, P., Komjathy, A. & Meng, X. in *Position, Navigation, and Timing Technologies in the 21st Century* 939–969 (John Wiley & Sons, Ltd, 2020). doi:https://doi.org/10.1002/9781119458449.ch32.

97. Vergniolle, S. & Ripepe, M. in *Fluid Motions in Volcanic Conduits: A Source of Seismic and Acoustic Signals* (The Geological Society of London, 2008). ISBN: 9781862392625. doi:https://doi.org/10.1144/SP307.7.

98. Vulpiani, G., Ripepe, M. & Valade, S. Mass discharge rate retrieval combining weather radar and thermal camera observations. *Journal of Geophysical Research: Solid Earth* **121.** doi:https://doi.org/10.1002/2016JB013191 (2016).

99. Walker, G. P. L. Explosive volcanic eruptions - a new classification scheme. *Geologische Rundschau* **62.** doi:https://doi.org/10.1007/BF01840108 (1973).

100. Walker, J., Halliday, D. & Resnick, R. *Fondamenti di Fisica* ISBN: 9788808182982 (Casa Editrice Ambrosiana, 2015).

101. Wallace, J. M. & Hobbs, V. *Atmospheric Science: an Introductory Survey* ISBN: 978-0-12-732951-2. doi:https://doi.org/10.1016/C2009-0-00034-8 (Academic Press, 2006).

102. Wassermann, J. in *New Manual of Seismological Observatory Practice (NMSOP)* (ed Bormann, P.) chap. 13 (Deutsches GeoForschungsZentrum, 2009). doi:10.2312/GFZ.NMSOP_r1_ch13.

103. Watada, S. & Kanamori, H. Acoustic resonant oscillations between the atmosphere and the solid earth during the 1991 Mt. Pinatubo eruption. *Journal of Geophysical Research: Solid Earth* **115.** doi:https://doi.org/10.1029/2010JB007747 (2010).

104. WDCG. *Geomagnetic Data Service* 2024. https://wdc.kugi.kyoto-u.ac.jp.

105. Widmer, R. & Zürn, W. Bichromatic excitation of long-period Rayleigh and air waves by the Mount Pinatubo and El Chichon volcanic eruptions. *Geophysical Research Letters* **19.** doi:https://doi.org/10.1029/92GL00685 (1992).

106. Woodhouse, M. J., Hogg, A. J., Phillips, J. C. & Sparks, R. S. J. Interaction between volcanic plumes and wind during the 2010 Eyjafjallajökull eruption, Iceland. *Journal of Geophysical Research: Solid Earth* **118.** doi:https://doi.org/10.1029/2012JB009592 (2013).

107. Yamamoto, R. A theoretical consideration of the atmospheric internal gravity waves. *Journ. Met. Soc. Japan* **41.** doi:10.2151/jmsj1923.41.1_5 (1963).

108. Zawdie, K. *et al.* Impacts of acoustic and gravity waves on the ionosphere. *Frontiers in Astronomy and Space Sciences* **22.** doi:https://doi.org/10.3389/fspas.2022.1064152 (2022).

109. Zuccarello, L. *et al. Testing infrasound array technology for monitoring eruptive activity at Mt. Etna, Italy* Rapp. Tec. (Istituto Nazionale di Geofisica e Vulcanologia, 2025). doi:https://doi.org/10.13127/rpt/490.